SEMMELWEIS EGYETEM

DOKTORI ISKOLA

Ph.D. értekezések

3372.

BERKI PÉTER

Funkcionális Idegtudományok

című program

Programvezető: Dr. Sperlágh Beáta, egyetemi tanár

Témavezetők: Dr. Dénes Ádám, tudományos főmunkatárs

Dr. Gulyás Attila, tudományos tanácsadó

MICROGLIA IN ACUTE BRAIN SLICES AND THEIR INFLUENCE ON NEURONAL NETWORKS

PhD thesis

Péter Berki

Semmelweis University

János Szentágothai Doctoral School of Neurosciences

Supervisors: Ádám Dénes, D.Sc
Attila Gulyás, D.Sc

Official reviewers: Katalin Schlett, Ph.D
Tamás Németh, Ph.D

Head of the Complex Examination Committee: Alán Alpár, MD, D.Sc

Members of the Complex Examination Committee: Tibor Zelles, MD, Ph.D
Lucia Wittner, Ph.D

Budapest
2025

Table of Contents

List of abbreviations

A1R	Adenosine A1 receptor
Aβ	Amyloid-β
ACh	Acetylcholine
ACSF	Artificial Cerebrospinal Fluid
AD	Alzheimer's disease
ADP	Adenosine Diphosphate
AIS	Axon initial segment
AMP	Adenosine Monophosphate
ATP	Adenosine Triphosphate
ARs	α and β adrenergic receptors
BBB	Blood-brain barrier
BDNF	Brain-derived neurotrophic factor
CA#	Cornu Ammonis Area # (1, 2, 3) in the Hippocampus
CD#	Cluster of differentiation molecule #
CD200	OX-2 membrane glycoprotein
CD200R	OX-2 membrane glycoprotein receptor
CLSM	Confocal Laser Scanning Microscopy
CNS	Central Nervous System
CSF1	Colony stimulating factor 1
CSF1R	Colony stimulating factor 1 receptor
CVOs	Circumventricular organs
Cst3	Cystatin C
Ctss – CatS	Cathepsin S
CX3CL1	Chemokine receptor 1 ligand
CX3CR1	Chemokine receptor 1 / fractalkine receptor / GPR13
DAPI	4'6-Diamidino-2-Phenylindole (double stranded DNA staining)
DAP12	DNAX-activation protein 12
DCs	Dendritic cells
DEPL	Depleted
DG	Dentate Gyrus

EMPs	Erythromyeloid progenitor cells
EMR1 – F4/80	EGF-like module-containing mucin-like hormone receptor-like 1
Ent	Entorhinal Cortex
fEPSPs	Field Excitatory Postsynaptic Potentials
GABA	Gamma-Aminobutyric Acid
GFP	Green Fluorescent Protein
GLUT	Glutamate
Gpr34	G-protein-coupled receptor 34
Hexb	Hexosaminidase subunit B
HMGB1	High mobility group box 1
IBA1	Ionized calcium binding adaptor molecule 1
IGF1	Insulin-like growth factor
IL – #	Interleukin – #
IRF8	Interferon regulatory factor 8
LFP	Local Field Potential
LysoPS	Lysophosphatidylserine
MerTK	MER Proto-Oncogene, Tyrosine Kinase
MFI	Mean fluorescent signal
MIP	Maximum intensity projection
mRNA	Messenger Ribonucleic Acid
MS	Multiple Sclerosis
NE	Norepinephrine
NF-H	Neurofilament H
NTPDase	Ecto-nucleoside triphosphate diphosphohydrolase enzyme
NVU	Neurovascular unit
P#	Postnatal day #
PAMPs	Pathogen-associated molecular patterns
P2X4R	P2X purinoceptor 4
P2Y12R	P2Y12 G-protein coupled purinoreceptor
P2Y13R	P2Y13 G-protein coupled purinoreceptor
PD	Parkinson’s disease
PRh	Perirhinal Cortex

PU.1	Transcription factor PU.1
Py	Hippocampal pyramidal layer
ROI	Region of interest
RUNX1	Runt-related transcription factor 1
SIRP	Signal regulatory protein
SWR	Sharp Wave-Ripple
TeA	Temporal Association Cortex
TGF-β	Transforming growth factor beta
THIK-1	Tandem pore domain Halothane Inhibited K+ channel 1
TLRs	Toll-like receptors
Tmem199	Transmembrane protein 199
TNF-α	Tumor necrosis factor alpha
TREM2	Triggering receptor expressed on myeloid cells 2
VGLUT1	Vesicular glutamate transporter 1
VGAT	Vesicular GABA transporter
VEGF	Vascular endothelial growth factor

1. Introduction

1.1. Neuroglial diversity in the nervous system

The brain is an extraordinarily complex organ, characterized by an intricate network of highly specialized cells. Together, these cells mediate a wide range of processes, collectively supporting the brain's integrated activity and enabling its diverse functions. Despite the extensive knowledge scientists have gathered about the central nervous system (CNS), precise mechanisms by which these cellular networks coordinate and regulate overall brain function remain incompletely understood. Nonetheless, it is evident that complex interactions among different cell types are fundamental to these processes. As a starting point, the neural tissue is often divided into two main types of cellular components: neuronal and glial cells that show a 1:1 ratio when considering the whole brain[1,2], however this can vary significantly across brain structures. Generally, neurons are thought of as the basic information processing units of the system, highly specialized in transmitting electrical impulses and are organized into complex network architectures via synaptic connections[3,4]. The composition of the neuronal population is extremely heterogeneous and can be further divided into various subtypes based on morphology, transmitter use, genetic expression profile and connectivity patterns[5–8]. This diversity is considered to be fundamental for allowing the intricate information processing mechanisms to manifest within the neural circuitry, ultimately allowing the nervous system to perform the multitude of tasks essential for survival and adaptation[9–11].

Beyond the intricate network of neurons lies an equally sophisticated ecosystem of non-neuronal cells, generally referred to as glia. Importantly, these glial cells also contribute to information processing with distinct spatial and temporal characteristics, while they work in close cooperation with the brain's vascular network to perform essential metabolic and homeostatic functions[12–14]. The three primary types of glial cells consist of astrocytes, oligodendrocytes and microglia, which collectively contribute to the diverse processes that keeps the CNS functional[15–18]. Importantly, these cellular partners bare distinct, yet highly interdependent roles communicating through a wide variety of intercellular interactions, just as interesting and nuanced as ones observed between neurons[17,19–21]. Briefly, astrocytes are involved in metabolic support by influencing extracellular ionic composition and neurotransmitter regulation[22–24], while they are also

known to release neurotrophic factors promoting the genesis and maturation of other cellular components[25–27]. Oligodendrocytes are primarily recognized for their role in myelination, the process of forming a protective myelin sheath around axons, facilitating the rapid conduction of nerve impulses[28–30]. Beyond myelination, oligodendrocytes also play crucial roles in maintaining neuronal health by providing metabolic and trophic support essential for energy production in axons[31,32]. Microglia mainly serve as the brain's resident immune sentinels working in close co-operation with other CNS-associated macrophages located at the borders of the parenchyma, generating dynamic responses to environmental cues or tissue disturbances[33–37]. While being pivotal in orchestrating neuroprotective and inflammatory processes, they modulate cerebral blood flow and possess important roles during development and homeostasis by regulating synaptic connections and neuronal activity[13,14,19,38].

Collectively, the glial population of the CNS is being more and more recognized for playing crucial roles in the emergence and propagation of neurological disorders, with a spotlight directed specifically on their importance in regulating central immune responses[34,39,40]. Despite the increasing attention focused on glial dysfunction, underlying mechanisms and effective targets for therapeutic interventions are still lacking, concerning many of the most detrimental neurological disorders such as Alzheimer's disease (AD), Parkinson's disease (PD) and multiple sclerosis (MS), among others[27,41–44]. Evidently, the challenge of understanding diseases with such complexity lies not only in deciphering the contributions of numerous individual components but also in thoroughly mapping interactions at the systemic level in both health and disease.

1.2. Neuroimmune crosstalk and CNS-associated macrophages

Neuroimmunology is a rapidly evolving interdisciplinary field investigating interactions between the nervous and the immune system with a special focus on its contributions to physiological and pathological states[39]. While the CNS is segregated by diverse border structures built up by specialized epithelial and endothelial cells which limit the access of peripheral immune cells and blood-derived substances to the CNS parenchyma, it is far from being an immune-privileged site. Interestingly, advances in the field revealed the existence of unique bidirectional pathways between the CNS and the immune system. For instance, the autonomic nervous system (ANS) innervates all primary and secondary lymphoid organs such as the thymus, bone marrow, lymph nodes, spleen, tonsils, gut,

lungs, peritoneum and the mucosal tissue of the skin[44,45]. Within these organs, efferent parasympathetic fibers of the ANS were shown to release acetylcholine (ACh), which binds to muscarinic and nicotinic receptors abundantly expressed on macrophages, dendritic cells, T cells, and B cells. This activation in turn can inhibit cytokine production and promote anti-inflammatory processes[44,46]. Apart from cholinergic immune modulation, sympathetic post-ganglionic fibers can also release norepinephrine (NE), which acts on α and β adrenergic receptors (ARs) and can bidirectionally modulate immune cell responses[46]. Furthermore, NE is also released into the blood stream from sympathetic nerve terminals and the adrenal medulla during stress and other conditions, from where it indirectly modulates blood and lymph flow, inflammatory cell recruitment, and leukocyte production in the bone marrow[47,48]. Additionally, afferent parasympathetic fibers, primarily those of the vagus nerve can detect pro-inflammatory cytokines like IL-1β and relay this information to the brain in order to coordinate systemic immune responses[46]. Notably, neuroimmune signaling also involves the circumventricular organs (CVOs), which are characterized by fenestrated capillaries that allow cytokines and pathogen-associated molecular patterns (PAMPs) to access the CVO parenchyma[49–51]. Specialized glial cells within CVOs highly express receptors for these molecules, and their activation triggers neuroinflammatory responses while also modulating brain circuits mediating sickness behavior, fever, and neuroendocrine regulation[49,50]. Upon activation, these cells also produce and release cytokines into the blood stream which can influence peripheral immune response through humoral routes[49]. Apart from CVOs, immune regulation is also present at the borders of the CNS, where it is mediated through various myeloid cells including specialized macrophages, mast cells and dendritic cells (DCs)[32,52]. Importantly, all of these cells express characteristic, myeloid-specific markers (IBA1, F4/80 or EMR1, CX3CR1, MerTK, CD11b/c) and are the primary immune-sentinels of these regions performing surveillance, remove cellular debris and maintain local cellular integrity[36]. They reside in areas within the choroid plexus, meninges and the subarachnoid space, and are instrumental in regulating the transduction of immune signals between the periphery and the CNS[36,53,54]. Fate-mapping studies revealed that both meningeal and perivascular macrophages form a long-lived, self-renewing population, which originate from yolk sac progenitors early during development[55]. In contrast, choroid plexus cells - known as epiplexus cells – were shown to have a dual origin: while

its primary population originates from the yolk sac, a substantial portion is continuously replenished by bone marrow-derived monocytes[55,56]. Collectively, these cells are heavily involved in guarding the health of the CNS at its borders and respond to any tissue disturbance or pathogens with protective and restorative functions[35,36,56,57]. For instance, perivascular macrophages participate in the removal of amyloid-β (Aβ) from the CNS and maintain BBB-integrity through preserving the health of endothelial cells, while also regulating capillary stability and vascular constriction[36]. Choroid plexus-resident macrophages among monocytes, mast cells and DCs were suggested to promote anti-inflammatory states for leukocytes during immune cell trafficking towards the CNS and promote recovery after injury[36]. Meningeal macrophages were shown to mainly perform as sentinels for infection or tissue disturbance by surveying the cerebrospinal fluid (CSF) and meningeal blood vessels, while they can either acquire anti- or pro-inflammatory phenotypes to regulate immune responses[36]. In line with this, genetic alterations of key myeloid genes or disruption of myeloid-neuron interactions results in the severe impairment of memory-related functions and social behavior, highlighting their importance in CNS homeostasis[36,57]. Importantly, these CNS-associated macrophages function in close cooperation with probably the most investigated, sole myeloid population situated within the brain parenchyma, called microglia[57].

1.3. Microglia, the resident immune sentinel of the CNS parenchyma

Microglia are tissue-resident macrophages colonizing the brain during early embryonic development[58–60] and are fundamental in orchestrating central immune responses, among several other important roles. Microglia represent ~5-15% of CNS-resident cells, and their myeloid identity was already suspected by Pio del Rio Hortega who first described this cell type in 1918. Studies since then revealed that microglia are derived from erythromyeloid progenitors (EMPs) originating from the yolk-sac at embryonic day 7.5-8 (E7.5-8) in mice[59,60]. Several key molecules have been implicated during the development of microglia, such as DNAX-activation protein 12 (DAP12), interferon regulatory factor 8 (IRF8), transcription factor PU.1 and runt-related transcription factor 1 (RUNX1), colony-stimulating factor 1 (CSF1) and transforming growth factor beta (TGF-β)[59,60]. Within the developing human brain, microglia progenitors can be detected as early as 3 weeks during gestation, colonization of the spinal cord begins after 9 weeks

and after 22 weeks microglia are widely distributed within the intermediate zone[61]. After differentiation and rapid proliferation, microglia populate the entire CNS forming a self-renewing, long-lived cellular population. In particular, neocortical microglia in mice showed a turnover rate of 26% per year with a median lifetime well over 15 months, meaning that approximately half of the microglia population persists through lifetime[62,63]. Similarly, the turnover in humans showed a median rate of 28% a year with an average lifetime of 4.2 years, while individual microglia can last potentially for decades[62]. Importantly, other monocytes can be recruited to invade the brain parenchyma in special conditions such as during CNS inflammation or when the microglial niche is compromised. In line with this, studies emphasize the remarkable self-renewing capabilities of microglia after genetic ablation, as they can rapidly proliferate and repopulate the whole brain (within ~5 days) from clusters of highly proliferative cells, independently from peripheral bone-marrow-derived myeloid cells[64]. While the number of microglia remains remarkably steady throughout life, they represent an extremely heterogenous and dynamic population with diverse functional adaptations across different contexts such as development, aging, health and disease[65–68].

1.4. The microglial sensome

In order to fulfill their role as immune sentinels and homeostatic regulators, physiological microglia display a unique transcriptomic profile often referred to as microglia 'signature genes' or the microglial 'sensome'. This includes a multitude of surface receptors which control the phenotypic identity of microglia, mediate interactions with other CNS constituents and enable the detection of tissue disturbances like the presence of pathogens, toxins, injured cells and cellular debris[69–71]. The main signaling mechanism suggested to maintain a mature microglia population involves CSF1R and its ligands CSF1 and interleukin-34 (IL-34) as knockouts of this pathway lead to the dramatic reduction of microglia among other tissue macrophages[72,73]. Of note, CSF-1 is mainly produced by oligodendrocytes and astrocytes, while IL-34 is produced by neurons, highlighting the importance of other CNS constituents shaping microglia identity[74]. Transforming growth factor β (TGF-β) and its microglial receptor TGF-βR2 is another key signaling pathway which promotes homeostatic microglial states and prevents excessive activation and inflammatory responses[76]. In addition, several other core microglial pathways exist that have marked impact on microglial states. For example, fractalkine signaling through

CX3CR1 plays a key role in shaping microglia phenotype, involved in microglia-neuron interactions promoting neuroprotection and survival, while also mediating cell migration, cytokine secretion, adhesion, apoptosis and phagocytosis both during development, homeostasis, and upon injury[75–78]. The lysosomal cysteine protease Cathepsin S (Ctss or CatS) is also widely expressed and released by microglia upon injury or by elevated extracellular ATP levels and liberates soluble fractalkine from neurons, creating a feedback loop for CX3CR1 promoting the release of inflammatory mediators[79,80]. Importantly, CX3CR1 is abundantly and selectively expressed in microglia, which enables the wide use of this receptor as a promoter to investigate or manipulate microglia functions[78]. Triggering receptor expressed on myeloid cells 2 (TREM2) is predominantly expressed in microglia and its role is widely investigated, particularly due to its involvement in AD. TREM2's primary function in microglia is mediating phagocytosis, particularly regarding the clearance of Aβ and apoptotic neuronal debris by enhancing microglial uptake capabilities[81–84]. TREM2 also plays a vital role in promoting microglial survival and metabolic adaptation, particularly under the stress of neurodegenerative processes, as it has been shown to maintaining metabolic fitness in microglia, enabling them to respond effectively to pathological cues[81]. G-protein-coupled receptor 34 (Gpr34) through its ligand lysophosphatidylserine (LysoPS) is involved in mediating immune responses and phagocytic behavior, sensing and responding to myelin debris by promoting the expression of proinflammatory cytokines[85,86]. Purinergic P2Y12 receptors are G_i-coupled receptors activated by nucleotides like ATP/ADP and are also predominantly expressed in microglia[70]. These receptors play a central role in shaping microglia phenotype and function, as they are involved in a multitude of microglial interactions with other CNS constituents including neurovascular coupling, monitoring neuronal states through somatic junctions and detection of injured or infected cells[13,18,19,87–89]. Furthermore, P2Y12 receptors are widely investigated for regulating chemotactic responses, which involves the directed movement of microglia processes towards injured sites or elevated extracellular ATP levels[90,91]. Similarly to P2Y12R, Transmembrane protein 199 (Tmem199) is an evolutionarily conserved microglia-specific marker also found in humans, while in contrast to P2Y12 it does not downregulate in pathological states, such as in AD[92]. Cystatin C (Cst3) and hexosaminidase subunit B (Hexb) are also recognized as stable microglial markers across

diverse physiological and pathological states implicated in protease inhibition and lysosomal function. Importantly, Cst3 is upregulated in patients with MS, while heritable Hexb deficiency results in Sandhoff disease[93–96]. Collectively, this complex 'sensome' enables microglial states to be spatially and temporally dynamic while performing a wide range of adaptive responses to environmental cues, ultimately resulting in a diverse phenotypic landscape[68,70,71]. Importantly, microglial heterogeneity is commonly observed across different brain regions, age and sex groups, while also being influenced by circadian rhythm, peripheral cues such as microbiota[97,98] or by a wide array of systemic diseases and pathological states[99].

1.5. Functional diversity of microglia

Within physiological conditions, fully matured microglia show a ramified morphology and perform micro-movements with their highly motile processes (1-2 μm/min), constantly surveying their micro-environment[91]. Importantly, a minor subset (~5%) of microglial cell bodies can also dislocate and migrate through the brain parenchyma, however this process – depending on brain region – typically occurs at a much slower rate (1–2 μm/h) relative to process motility[93,102]. Since microglia in undisturbed conditions are evenly distributed within the tissue forming an almost crystal-like topology, this form of scanning behavior is estimated to enable the microglia population to scan the entire brain parenchyma within hours[100]. These sophisticated process movements require cytoskeleton remodeling through bundling and membrane ruffling, including the functional cooperation of surface receptors and ion channels such as P2Y12R, P2X4R, P2Y13R, CX3CR1, adenosine receptor and the tandem pore-domain halothane inhibited K+ channel (THIK-1)[101,102]. Importantly, THIK-1 is posited to be tonically active, setting microglia membrane potential and maintaining ramified morphology during surveillance, while purine and fractalkine receptors are possibly involved in guiding directed movements upon activation by local cues[102]. During these seemingly randomized process movements, microglia have been shown to contact, monitor and influence almost all CNS constituents including cells within the cerebral vasculature, astrocytes, oligodendrocytes, synaptic junctions and neuronal soma at specialized contact sites. In particular, microglia form cell-cell contacts with all the cellular components of the neurovascular unit (NVU), such as perivascular macrophages, pericytes, endothelial cells, astrocytes and neurons[13,89,103–105]. Importantly, these

microglia-NVU contacts have been shown to influence cerebral blood flow, hypercapnia-induced vasodilation and neurovascular coupling in a P2Y12R mediated manner, while the CX3CL1-CX3CR1 pathway is involved in modulating capillary constriction. These microglia-mediated mechanisms are vital for maintaining the metabolic needs - including glucose and oxygen - of CNS constituents.

Interestingly, direct contacts with neurons are posited to form dynamically in a compartment-dependent manner[19]. This is supported by the fact that neurons have an extremely elaborate three-dimensional morphology with functionally segregated compartments such as the somatic region, the axonal region and the axon initial segment (AIS), dendritic regions and synaptic elements. Since these compartments have distinct roles in neuronal signaling which involve different metabolic and regulatory needs, it is likely that microglial contacts at these sites are also compartment-specific. For instance, microglial contacts formed at neuronal somatic regions are called 'somatic junctions', which represent an interface for microglia to monitor neuronal states through mitochondria-related messenger molecules[89]. Microglia can detect and respond to changes in mitochondrial function like metabolic imbalance, oxidative stress, inflammation, cellular injury or cell death[106,107]. Importantly, these microglia-neuron contacts also rely on P2Y12R signaling, as disruption of this purinergic pathway results in the reduction of somatic junction prevalence, which was correlated to increased infarct volumes after acute brain injury induced by experimental stroke[89]. Contacts formed at synaptic elements are possibly the most heavily investigated, with direct membrane-membrane interactions between microglial processes, synaptic boutons and spines[108,109]. Microglia form contacts both with glutamatergic and GABAergic synapses and were shown to be involved in the elimination of silent synapses and in activity-dependent synaptogenesis during development and in adulthood[110,111]. In addition, direct microglia-dendrite interactions were shown to induce filopodia formation[112]. The AIS together with more distal axonal regions including the nodes of Ranvier also receive microglial contacts that were shown to influence output signals and promote myelination[113–115]. Importantly, microglia through these diverse connections are not only monitoring, but also influencing neuronal activity, as it has been demonstrated that microglia can control mitochondrial function, synaptic activity, depolarization and neuronal synchrony[89,115,116]. Apart from direct interactions, microglia and neurons also communicate through a wide range of

soluble substances such as neurotransmitters (GABA, glutamate), interleukins (IL-1β, IL-10), fractalkine, purine nucleotides (ATP, ADP, adenosine), brain-derived neurotrophic factor (BDNF) and tumor necrosis factor alpha (TNF-α)[19,25,117–119]. Microglia are also posited to communicate with neurons through intermediate cells including astrocytes and cells within the NVU, or even through the interaction of different organ systems including peripheral nerves via neuronal and humoral routes or by interactions through the gut-brain axis[18,97,105,120,121]. Collectively, these microglia-neuron interactions were shown to be pivotal during development in regulating neurogenesis, cell differentiation and migration, synaptogenesis, synaptic remodeling, and removal of apoptotic or excess neurons and synapses[122–126].

1.6. Context-dependent changes in microglial phenotypes

Since homeostatic microglia are constantly surveying the brain parenchyma, changes in environmental cues due to trauma, injury, infection or disease are quickly integrated through the microglial sensome resulting in functional and phenotypic microglial transformation[44,99,127,128]. Historically, microglial phenotypic states were categorized rigidly by imposing a dichotomic view, which only distinguished 'pro-inflammatory' or 'anti-inflammatory', 'activated' versus 'resting', 'ameboid' or 'ramified', and M1 versus M2 phenotypes. Importantly, recent high-throughput transcriptomic and single-cell studies have revealed that microglial phenotypes form a multidimensional and context-dependent spectrum, rather than conforming to simple binary or static states[132,133]. To this end, traditional dualistic views are now considered to be outdated, as they do not reflect properly the diversity of microglial phenotypes. Instead, microglia display a diverse array of activation states, with overlapping gene expression profiles that reflect the complexity of their responses to the CNS microenvironment[132–134]. For example, the Human Microglia Atlas (HuMicA) has identified that multiple homeostatic and reactive microglial subpopulations coexist in the human brain, each characterized by distinct gene signatures and functional properties[135]. Importantly, this microglial heterogeneity is influenced by region-specific cues, developmental stage and disease context, resulting in unique transcriptomic and functional profiles across different CNS compartments and states[132,133]. Additionally, microglia also undergo distinct transcriptional changes during development, aging, and in response to pathological insults, with gene clusters associated with proliferation, synaptic pruning, immune surveillance, and inflammation being

differentially regulated at each stage[134]. While morphological changes - from highly ramified to amoeboid forms - often accompany these functional transitions, these features are also considered to be part of a broad morpho-functional continuum, rather than discrete activation categories[133,134]. Importantly, microglial phenotypes are not terminally locked into these states, as they can reversibly shift in response to evolving environmental signals, which is ultimately governed by intricate epigenetic and transcriptomic regulation. Consequently, microglial phenotypes in response to trauma, injury, infection or disease are extremely heterogeneous and strongly depend on the pathological context with a wide array of transcriptomic, proteomic and morpho-functional characteristics[133]. Furthermore, it is increasingly evident that phenotypic states are not fixed or clearly defined categories, as microglial phenotypes can change more freely and fluidly within a multi-parameter space of states.

1.7. Injury-induced central neuroimmune responses

Acute injury can induce radical changes in environmental cues within the brain parenchyma, which is usually divided into primary/acute and secondary/delayed phases[136,137]. The primary phase of injury involves the immediate mechanical damage to the brain, leading to a localized necrotic area of neuronal and glial cells paired with the rapid accumulation of cellular debris within minutes at the lesion site[137]. In addition, CNS injury is often paired with BBB disruption, allowing the leakage of circulating molecules into the brain parenchyma followed by vascular activation and the infiltration of peripheral immune cells[138,139]. Consequently, the secondary phase of injury constitutes biochemical, cellular and physiological events that are initiated during the primary phase of the injury. Depending on the severity of the insult, these processes can last potentially from hours to years and may result in gliosis, scar formation and a prolonged immune response[137]. Within this phase, a series of biological processes are triggered which ultimately result in necrosis, ischemia, excitotoxicity, apoptosis, edema, and inflammation[140–142]. Necrosis is considered to be an uncontrolled form of cell death which typically occurs at the core of injured sites due to severe tissue damage and energy failure, resulting in cell swelling, plasma membrane rupture, and the release of damage-associated molecular patterns (DAMPs)[145]. Additionally, necrotic processes also affect peri-lesioned sites by the rapid diffusion of these injury-related soluble factors[136,144,145]. Ischemic events typically result from insufficient oxygen and glucose supply which

disrupts the energy metabolism of cells, eventually causing ATP depletion and mitochondrial failure, ionic imbalance, depolarization, and an excessive release of glutamate into the extracellular space[143]. Consequently, elevated glutamate concentrations overstimulate extrasynaptic NMDA receptors on neurons leading to massive Ca^{2+} influx (excitotoxicity), triggering signaling pathways that activate pro-apoptotic proteins and the programmed death of neurons[144]. Importantly, necrotic cells release a broad mixture of DAMPs rapidly and passively due to membrane rupture, which include ATP, histones, heat shock proteins, extracellular RNAs (exRNAs) and high mobility group box 1 (HMGB1). In contrast, apoptotic cells release DAMPs in a regulated, stage-dependent manner which also includes ATP, HMGB1, histones and exRNAs, which can modulate immune responses differently[148,149]. Microglia can rapidly sense DAMPs through purinergic receptors and TLRs, which signaling pathways are vital in orchestrating the inflammatory response[150].

Within these conditions, the homeostatic state of microglia characterized by ramified morphology and surveillant behavior can quickly transform near the affected tissue and acquire reactive phenotypes[151]. This activated state is often characterized by transitioning into an amoeboid morphology paired with process polarization and cell body migration towards injured sites[90]. The injury-induced, directed process motility have been shown to be guided by purinergic signaling (specifically P2Y12R) and involve the co-operation of astrocytes[101,143]. In particular, it has been demonstrated that P2Y12R is widely expressed in homeostatic microglia, while gradual loss of P2Y12R correlates with transformation from ramified to an ameboid morphology. Along these lines, P2Y12R knockouts do not respond with process extraction to the presence of exogenous nucleotides (ATP) either via directly applied or released after focal laser ablations[92,93,153]. Subsequently, activation of P2Y12 receptors have been shown to potentiate THIK-1 activity resulting in reduced branching, activation of the inflammasome and the release of pro-inflammatory cytokine IL-1β[102]. In addition, the presence of other DAMPs including cellular debris, and reactive oxygen species (ROS) are integrated trough the microglial sensome and can trigger the release of other mediators promoting inflammation such as TNF-α, IL-6, IL-12, interferon-γ (IFN-γ), inducible nitric oxide synthase (iNOS) and proteolytic enzymes (MMP9, MMP3)[144]. These factors are posited to ultimately promote neurotoxic processes and exacerbate the damage after injury[145].

Along these lines, several studies demonstrated that TNF-α, IL-6 and IL-1β expression increases during aging, which correlates well with the commonly observed increased vulnerability to CNS injury in adult individuals[146–148]. Conversely, microglia within the same injured environment can also acquire reactive phenotypes releasing anti-inflammatory substances like IL-10, the IL-1 agonist IL-1ra, BDNF, TGF-β, insulin-like growth factor (IGF1) and vascular endothelial growth factor (VEGF) which are posited to promote tissue repair and facilitate the resolution of inflammation[149,150]. Based on these results, reactive microglial phenotypes were historically considered to be dualistic in their nature, as they seem to both promote and decelerate the resolution of inflammation after tissue disturbance[144,145,150]. As stated above, such dichotomic views of 'detrimental' or 'beneficial' microglial states are becoming outdated, as recent studies emphasize that different microglial phenotypes coexist as dynamic and plastic responders to environmental cues[136]. Of note, the release of pro-inflammatory agents after the acute phase of the injury is necessary for the recruitment of immune cells to protect against invading pathogens and for the elimination of tissue debris, while anti-inflammatory factors can ultimately downregulate the immune response upon the hiatus of such cues, promoting regeneration and preventing excess inflammation[150]. Importantly, it is still not well understood how exactly these microglial states are coordinated by intrinsic transcriptomic processes and injury-related external signals, and in turn, how they influence the activity of other CNS constituents.

1.8. Invention and evolution of acute brain slices

In the 1950s and 1960s McIlwain and colleagues demonstrated through a series of seminal experiments that viability and electrophysiological properties of neurons can be maintained within isolated brain slices[151,152]. Their legacy later on became one of the cornerstones of neuroscientific research by contributing significantly to our current understanding of processes ranging from nanoscale events to complex neuronal circuits[8,156–158]. Initially, McIlwain and his collaborators pioneered both manual and mechanical methods for preparing viable brain slices, including the invention of the McIlwain tissue chopper. In addition, they developed an integrated apparatus comprising a slice chamber, perfusion system and thermostat, which allowed for the maintenance of tissue viability during measurements[161,162,166]. These advancements have laid down the foundation of acute slice experimentation and facilitated the combination of different

techniques for investigating cellular processes within isolated tissues[162,163]. Later on, numerous iterations in slice preparation methods were introduced, which further enhanced the viability of cells by mitigating injury-related alterations during tissue isolation. One of these novel methods involved ice-cold (~0–4°C) transcardial perfusion prior to brain extraction and slicing[159], which reduces the metabolic demand of cells and slows down enzymatic processes. Consequently, ice-cold artificial solutions were also utilized during tissue sectioning to minimize the extent of ischemic injury and preserve cellular energy stores. After the slicing procedure, tissue sections are transferred into an incubation chamber containing physiological temperature solutions (~34–37°C) to support recovery and function[165,169]. Importantly, while ice-cold solutions have been shown to be beneficial for cellular viability, subsequent studies indicated that they alter the ultrastructure, molecular composition and density of synaptic elements, often leading to synaptic sprouting[181–183]. To this end, cutting solutions heated to physiological temperatures have been utilized specifically to study synaptic mechanisms and demonstrated several advantages over ice-cold solutions, including higher release probability and better preservation of synaptic processes[163,164]. Another critical advancement was the introduction of protective cutting and recovery solutions in which sodium ions (Na^+) are partially or fully substituted with alternative ions such as sucrose or N-methyl-D-glucamine (NMDG)[165,169,172]. The aim of this technique is to reduce excitotoxicity by limiting sodium-dependent depolarization and glutamate release during slicing, while also preserving osmotic balance and preventing edema[169]. Adjusting the concentrations of divalent cations, specifically by shifting magnesium (Mg^{2+}) and calcium (Ca^{2+}) levels is another strategy which was developed to protect neurons during slicing. Within this medium, elevated Mg^{2+} concentrations can block NMDA receptor-mediated excitotoxicity, while carefully balanced Ca^{2+} levels are essential for maintaining synaptic transmission without exacerbating calcium overload[171]. In addition to ionic modifications, the incorporation of antioxidant and volume-regulating compounds into cutting and recovery solutions has further enhanced slice quality. Antioxidants were shown to mitigate oxidative stress generated by ROS during tissue trauma, while volume-regulating agents help to maintain cellular osmolarity and prevent swelling[165,174].

In addition to improvements in slice quality, the popularity of acute slice experimentation was further facilitated by its ease of integration with other advanced

experimental techniques. For example, high-density multielectrode arrays (HD-MEAs) enabled simultaneous recording from hundreds to thousands of neurons with high spatial resolution, allowing detailed analysis of synaptic activity and network dynamics within specific brain regions[165]. These arrays capture complex spatiotemporal patterns of neuronal signaling that were previously inaccessible using traditional single-electrode methods. Multi-slice recording systems increased experimental throughput by permitting parallel electrophysiological recordings from multiple slices, thereby facilitating comparative studies across different brain areas or experimental conditions[166,167]. Alongside these developments, optogenetic tools also revolutionized *ex vivo* experimentation by allowing precise, cell-type-specific control of neuronal activity through genetically encoded light-sensitive proteins[168,169]. When combined with advanced optical imaging and stimulation techniques like structured illumination microscopy using multi-mirror devices (MMD), optogenetics enabled high-throughput, all-optical interrogation of cellular and circuit mechanisms, alongside other physiological processes[180]. Moreover, acute brain slices provided an ideal platform for pharmacological investigations due to their accessibility and controlled environment. The ability to apply pharmacological agents directly to the perfusion medium allowed precise temporal and concentration control over drug exposure, facilitating detailed studies of receptor function, synaptic modulation, and network pharmacodynamics[176]. The ease of pharmacological manipulation combined with advanced recording and stimulation techniques have greatly enhanced the utility of slice preparations for dissecting the molecular and cellular mechanisms underlying neuronal function.

1.9. Slice preparations as models for studying microglia

Initially developed to investigate neuronal circuits, acute brain slices have become increasingly valuable for microglia research over the past decades. A key advantage of slice preparations is that they preserve much of the native tissue architecture and local cellular microenvironment, which allows detailed investigation using advanced techniques such as optogenetics, high-resolution imaging, electrophysiology, and direct pharmacological manipulation[175–177]. As mentioned above, microglial behavior and identity are strongly influenced by the environment and interactions with other CNS constituents[75,178]. While in vivo models provide the most intact environmental context – including systemic influences like blood flow and immune signaling – acute slice

preparations offer a balance between preserving these features and enabling increased experimental control and reproducibility[178,179]. In particular, acute slices allow precise regulation of the extracellular environment, direct drug application, and simultaneous multimodal measurements. These advantages facilitate detailed, time-resolved studies of microglial morphology, electrophysiology, gene expression, and interactions with neurons and other glial cells[131,181–183]. Other ex vivo methods, including primary and co-cultures, organoids, and microglia-like cell lines also provide advanced experimental control, however, microglial phenotypes in these models tend to diverge further from homeostatic signatures compared to those in slice preparations[173,175,176]. Recent transcriptomic-level comparisons between organotypic slice-resident, glial culture-resident, and acutely isolated microglia demonstrate that homeostatic signature genes correlate more closely with the in vivo state in slice preparations[173,174]. This is likely due to the preservation – at least partially – of the original CNS architecture and critical cell-cell interactions, such as CSF-1, IL-34, cholesterol, TGF-β2, CX3CL1, and CD22 that are necessary for maintaining microglial homeostasis[74]. To this end, studies using slices to investigate microglia in pathological contexts often emphasize that baseline behavior and disease-related functions correlate well with in vivo observations[177–182]. However, significant differences between ex vivo and in vivo microglial states are also recognized[131,187–189].

Despite the well-known sensitivity of microglia to environmental changes, only a limited number of studies have systematically examined how slice preparation itself affects baseline microglial behavior. Acute slices inherently contain numerous injury-related cues, including dead or dying cells, cellular debris, elevated extracellular purinergic nucleotides, blood-brain barrier disruption, and increased pathogen presence[177,190]. Transcriptomic analyses show that organotypic slices immediately after preparation exhibit rapid increases in pro-inflammatory markers such as neurofilament H (NF-H), IL-6, and TNF-α, alongside upregulation of microglial inflammatory signatures including CD45, CD44, and CD68, as well as increased autofluorescence[173,174]. These findings indicate a robust inflammatory state, where microglial phagocytic activity is elevated due to apoptotic cells and debris. The duration and extent of these injury-induced alterations remain unclear. While the inflammatory state subsides only after weeks in culture, neurodegenerative markers and structural degradation begin to appear after

approximately three weeks[177]. Microglial function is heavily regulated by purinergic signaling via extracellular ATP, which is anticipated to increase significantly following tissue injury due to the passive release of nucleotides from damaged neurons[90,91,101]. Additionally, acute slices show downregulation of microglial P2Y12 receptors, astrogliosis, mitochondrial dysfunction, morphological changes, and microglial migration within 1–2 hours post-preparation[128,183–186]. Microglia are highly motile cells that respond rapidly to tissue disturbances by extending processes and migrating toward injury sites[90,91]. To this end, acute slice preparations are widely used to study these mechanisms since they allow real-time imaging of microglial responses to various stimuli. Many studies induce localized injury via focal laser ablation or pharmacological agents such as ATP or LPS[101]. While these methods provide a well controlled induction of injury signals, they are only additional to the baseline injury signal initially introduced by the slice preparation itself. Changes may also impact network organization and neuronal synchrony, since microglia are well known to regulate network architecture and neuronal activity with diverse roles at synapses and neuronal somata[19]. Based on this, it is plausible that microglia can dynamically influence synaptic remodeling under these conditions. Of note, synaptic sprouting is commonly observed in acute slices[190–192].

Taken together, environmental factors inherent to acute slice preparations are likely to profoundly influence microglial phenotypes and in turn, impact network organization and functioning, which processes remain insufficiently characterized. Moreover, acute slice experiments employ a wide variety of methodologies, with each laboratory using distinct tools, solutions and protocols, whose effects on microglial states are largely unknown. Therefore, a systematic, time-resolved characterization of microglia residing in acute slices, including the mechanisms underlying injury-induced activation and the resulting alterations in network function, is essential to accurately interpret and contextualize findings derived from these preparations.

2. Objectives

2.1. Establishing a standardized acute slice time-series paradigm

The first objective was to develop a rigorously controlled protocol for slice preparation and incubation, with tissue fixation at well-defined time points. This standardization aimed to minimize artefacts from methodological variability and ensure consistency across experiments. To test the generalizability of certain methodological impacts, we also included modified protocols and invited independent laboratories to contribute tissue samples prepared with their native methods. All samples underwent identical post-fixation processing and blinded analysis to assess how different methodologies influence microglial responses.

2.2. Time-dependent characterization of microglial phenotypes

Using this framework, we aimed to perform detailed, time-resolved profiling of injury-induced microglial changes. Time lapse or z-stack confocal imaging of fluorescent microglia ($CX3CR1^{+/GFP}$) was planned to capture spatiotemporal dynamics, cell body and process distribution, migration to injury sites, and purinergic (P2Y12R) receptor expression via quantitative immunofluorescent labeling. We monitored multiple brain regions and developmental stages to account for region- and age-dependent variability. Additionally, time-dependent single-cell electrophysiology was employed to correlate morphological changes with possible alterations in ion regulation and membrane properties.

2.3. Investigating mechanisms underlying phenotypic changes

Our third goal was to explore signaling pathways regulating injury-induced microglial transitions. We utilized genetic knockout models of mice lacking microglia-specific receptors (P2Y12R, CX3CR1) or applied their selective pharmacological antagonists (PSB 0739, AZD 1283). To study extracellular purinergic signaling, we developed a novel transgenic mouse expressing the sensitive $GRAB_{ATP}$ fluorescent sensor ($ATP1.0^{\Delta Vglut1}$) or delivered the sensor via viral vectors (AAV9-hsyn-cATP1.0) into microglia-labeled mice strains (CX3CR1-cre/tdTomato). These approaches allowed

simultaneous monitoring of microglial behavior and purinergic dynamics, including the effects of receptor antagonism.

2.4. Assessing microglial impact on network architecture and synchrony

Finally, we investigated whether microglial activity in acute slices influences synaptic connectivity and neuronal synchrony. Given that microglia are well known regulators of synaptic elements, we investigated via quantitative immunofluorescent labelling whether microglia could also influence synaptic sprouting, a phenomenon which regularly occurs in acute slice preparations. Using P2Y12R and CX3CR1 genetic knockout mice and microglia-depleted wild-type mice (via PLX3373 or PLX5622), we also aimed to elucidate whether microglia might contribute to the spontaneous emergence of neuronal synchrony by performing simultaneous electrophysiological recordings in hippocampal slice preparations.

3. Methods

3.1. Experimental animals

In the studies used for this thesis the following mice strains were used: CX3CR1$^{+/GFP}$, CX3CR1$^{-/-}$ (knockout), P2Y12$^{-/-}$, NKCC1$^{-/-}$, CX3CR1-cre/tdTomato, ATP1.0$^{\Delta Vglut1}$ or C57Bl/6J as control groups. In all experiments male mice were used, except for data presented in Figure 12, Figure 13 and Figure 14b, where both genders were used in order to obtain sufficient animal numbers from littermates. Mice were kept in the vivarium on a 12-hour light/dark cycle and provided with food and water ad libitum. Temperature was 22 ± 2 °C paired with 50 ± 10% humidity. Animals were housed 2-3/cage.

3.2. Standardized protocol for slice preparation, incubation and fixation

To prevent bacterial contamination, all instruments and containers used for slice preparation and incubation were thoroughly cleaned with 70% ethanol and rinsed with distilled water before and after each experiment. For acute brain slice preparation, mice were deeply anesthetized with isoflurane and decapitated. The brains were quickly removed and placed in an ice-cold, carbogenated (95% O_2/5% CO_2) cutting solution for at least 30 minutes prior to use, containing (in mM): 205 sucrose, 2.5 KCl, 26 $NaHCO_3$, 0.5 $CaCl_2$, 5 $MgCl_2$, 1.25 NaH_2PO_4, and 10 glucose. Horizontal hippocampal slices (300 µm or 450 µm for LFP recordings) were cut using a Leica VT1000S vibratome, with the interval from decapitation to fixation / placement in the incubation chamber kept within 5–10 minutes. After slicing, tissues were transferred to an interface-type chamber with standard ACSF (in mM: 126 NaCl, 2.5 KCl, 26 $NaHCO_3$, 2 $CaCl_2$, 2 $MgCl_2$, 1.25 NaH_2PO_4, 10 glucose; saturated with 95% O_2/5% CO_2) at 35 °C, which then cooled to room temperature. Slices were supported by rectangles of sterile lens cleansing tissue (Whatman) placed on a nylon mesh, allowing oxygenation of the tissue from the humidified and saturated air above. At designated time points, slices were immersion-fixed in 4% PFA for 1 hour. For experiments involving PSB-0739, both cutting and ACSF solutions contained 10 µM PSB-0739. For perfusion fixation, mice were anesthetized and perfused transcardially with 0.9% NaCl for 1 minute, then 4% PFA in 0.1 M phosphate buffer for 40 minutes, followed by a 10-minute wash with 0.1 M PB. Brain regions including the somatosensory cortex and ventral hippocampus were dissected and

sectioned horizontally using a Leica VT1200S vibratome at 50 µm for immunofluorescence and 100 µm for automated morphological analysis. Invited laboratories who donated slice preparations used the following slice preparation protocols:

Lab #2: deep isoflurane anesthesia; ice-cold, NMDG-based, HEPES-buffered cutting solution (135 NMDG, 10 d-glucose, 4 $MgCl_2$, 0.5 $CaCl_2$, 1 KCl, 1.2 KH_2PO_4, 20 HEPES, 27 sucrose saturated with 100% O_2); incubation: interface-type chamber filled with reduced sodium and sucrose ACSF solution (in mM: NaCl 85, d-glucose 25, sucrose 55, KCl 2.5, NaH2PO4 1.25, CaCl2 0.5, MgCl2 4, NaHCO3 26, pH 7.3-7.4 saturated with 95% O_2–5% CO_2).

Lab #3: deep isoflurane anesthesia; ice-cold, sucrose-based cutting solution (in mM: NaCl 60, sucrose 100, KCl 2.5, NaH2PO4 1.25, NaHCO3 26, CaCl2 1, MgCl2 5, d-glucose 20 saturated with 95% O_2–5% CO_2); incubation: submerge-type chamber filled standard ACSF solution (in mM: NaCl 125, KCl 3.5, NaH2PO4 120, NaHCO3 26, CaCl2 2, MgCl2 5, d-glucose 15, pH 7.3-7.4 saturated with 95% O_2–5% CO_2).

3.3. Cross-sectioning and quantification of cell body/process distribution

Acute brain slices (thickness: 300 µm) were immersion-fixed with 4% PFA in 0.1 M phosphate buffer solution at various time points: immediately after slicing (0 min), or following 20 minutes, 1, 2, or 5 hours of incubation in an interface-type chamber. After a fixation period of 1 hour, slices were washed in 0.1 M phosphate buffer, embedded flat in 2% agarose, rotated by 90°, and then re-sectioned at 50 µm using a Leica VT1200S vibratome. The resulting sections were mounted on glass slides and coverslipped with Aqua-Poly/Mount. Microglia expressing CX3CR1-GFP were visualized using a Nikon Eclipse Ti-E inverted microscope equipped with a CFI Plan Apochromat VC ×20 DIC N2 objective (NA 0.75) and an A1R confocal system. Fluorescence was excited with a 488 nm laser, and image stacks at a resolution of 0.62 µm per pixel were acquired using NIS-Elements software. Maximum intensity projections spanning the full thickness of each section were saved as TIFF files. Cell bodies were identified and masked in Fiji using the “Analyze Particles” plugin, and these masks were subtracted from the original images to isolate microglial processes. To validate volumetric measurements, the average thickness of slices throughout the incubation period was assessed (mean ± SD:

262 ± 7 µm), with no significant differences observed between groups (Kruskal–Wallis test, $p > 0.05$). For quantification, a grid dividing the section thickness into seven equal zones was applied, allowing for the counting of cell bodies and measurement of microglial process volume by integrated fluorescence density within each zone using Fiji. Cell-body translocation was analyzed by recording the positions of cell bodies in Fiji and measuring their distances from the bottom surface or the central Z-depth at both 0 min and 5 h. The sorted distance values from 0 min were subtracted from those at 5 h to determine the minimum distance each cell had to move to reach its final position. For assessing process area coverage, images with masked cell bodies from slices fixed at 0 min and 5 h were binarized in Fiji, and the percentage of the area covered by processes was calculated.

3.4. Z-stack acquisition and time-lapse imaging of microglia

Acute brain slices (300 µm thick) were obtained from 80-day-old CX3CR1$^{+/GFP}$ mice as previously described. Approximately one hour after slicing, z-stack images (1 µm intervals) were captured using a Nikon C2 laser scanning confocal microscope with a ×20 CFI Plan Apo VC objective (NA 0.75, WD 1.00 mm, FOV 1290.4 mm) at 488 nm, while slices were continuously perfused with ACSF at 3 ml/min. Image stacks were acquired every 20 minutes over a 6-hour period. Videos were processed using NIS Elements 5.00 and ImageJ 1.53f51. The same confocal system, paired with a ×40 CFI Apochromat Lambda S objective (NA 1.25, WD 0.18 mm, FOV 840 µm), was used to monitor ATP dynamics following ecto-ATPase inhibition with ARL 67156 (10 µM, Tocris) at a rate of 0.5 frames per second. To track ATP responses before and after secondary mechanical injury, imaging was performed at ×4 magnification (Plan Fluor objective, NA 0.13, WD 17.2 mm, FOV 3215.36 µm) using a CoolLed pE-4000 light source and Hamamatsu ORCA-Flash 4.0 camera. Secondary injuries were introduced manually with a sterile blade, and imaging commenced within 1–2 minutes. For ATP visualization, the sensor was either delivered via AAV injection into CX3CR1-cre/tdTomato mice, or slices were prepared from ATP1.0ΔVglut1 mice. The ages of animals used in these experiments ranged from P19–20 to P69–99, as detailed in the figure legends.

3.5. Automated morphological analysis

Acute slices harvested as described above underwent 1-hour immersion fixation after designated intervals (0 min, 20 min, 1, 2, or 5 hours) spent in the incubation chamber. Following fixation, slices were washed in 0.1 M phosphate buffer (PB), embedded flat in 2% agarose blocks, and re-sectioned at 100 µm thickness using a Leica VT1200S vibratome (Fig. 1b). Sections from the middle region of incubated slices were immuno-stained. To prevent tissue deformation, preparations remained free-floating during imaging. Imaging occurred in 0.1 M PB using a Nikon Eclipse Ti-E inverted microscope with a ×60 water immersion objective (NA 1.2) and A1R confocal system, capturing volumes at 0.2 µm/pixel resolution and 0.4 µm Z-steps. For 3D microglial morphology analysis, we utilized the MATLAB-based Microglia Morphology Quantification Tool (accessible at https://github.com/isdneuroimaging/mmqt), which automatically derives 59 morphological parameters through 4 distinct analysis steps: 1: nuclei identification, 2: 3D skeletonization, 3: watershed segmentation, and 4: cell segregation.

3.6. Pre-embedding immunofluorescent labelling

Prior to immunofluorescent labeling, 50 µm-thick sections underwent sequential washes in phosphate buffer (PB) and Tris-buffered saline (TBS). Sections were then blocked for 1 hour at room temperature in TBS containing 1% human serum albumin (HSA; Sigma-Aldrich) and 0.03–0.1% Triton X-100. Primary antibody mixtures diluted in TBS were applied overnight at room temperature, followed by TBS washes and subsequent overnight incubation at 4°C with secondary antibody mixtures in TBS. After final TBS and PB washes, sections were mounted on glass slides using Aqua-Poly/Mount. Imaging was conducted on a Nikon Eclipse Ti-E inverted microscope equipped with a ×60 oil immersion objective (NA 1.4) and A1R confocal system. Imaging utilized 405, 488, 561, and 647 nm lasers with line-serial scanning at 50 × 50 nm pixel resolution. Z-stacks were acquired via NIS-Elements AR. Quantitative analysis involved at least two observers who have been blinded to the origin of the data. For somatic contact assessment, cortical regions were imaged using dual labeling of cell-type marker and a microglia marker (for details see: Table 1). Cells were counted when fully contained within z-stacks, with contacts defined by microglial processes touching ≥0.5 µm of somatic surface without gaps. Microglial process coverage was measured on 300 nm-step z-stacks: Kv2.1-positive

cells were randomly selected, and contact area was calculated as (soma circumference × section thickness) across slices. Synaptic contact analysis employed triple labeling (pre-/post-synaptic markers + microglia). Pre- and postsynaptic channel thresholds were adjusted in FIJI, with "fill holes" and "erode" applied. Automated particle tracking identified synapses where pre- and postsynaptic puncta touched. A systematically random subset was validated in original z-stacks, with microglial contact defined as processes within 200 nm (4 pixels) of synapses.

3.7. Post-embedding immunofluorescent labelling

We adapted the method by Holderith et al.[196] with minor modifications. Acute 300 µm-thick slices from CX3CR1$^{+/GFP}$ mice were immersion-fixed at the given intervals. Fixed slices were washed in 0.1 M phosphate buffer (PB) and 0.1 M maleate buffer (pH 6.0), then treated with 1% uranyl-acetate in maleate buffer for 40 min (dark conditions). After PB washes, slices underwent dehydration through an alcohol series and acetonitrile, followed by embedding in Durcupan. Each block contained a full time-series from one animal. Ultrathin sections (200 nm) cut with a Leica UC7 ultramicrotome spanned the entire slice width and were mounted on Superfrost Ultra plus slides. Slides were heated at 80 °C for 30 min, then oven-baked overnight. Sections were outlined with silicon polymer, resin-etched with Na-ethanolate (5 min, RT), and rinsed through ethanol gradients to distilled water. Antigen retrieval used 0.02 M Tris Base (pH 9) with 0.5% SDS at 80 °C for 80 min. After TBST washes, blocking occurred in TBST with 6% BlottoA, 10% NGS, and 1% BSA (1 h), then primary antibodies in blocking solution (overnight, RT, agitation). Secondary antibodies in TBST/25% blocking solution (3 h) preceded final TBST/DW rinses and mounting in Slowfade Diamond. Immunofluorescence analysis used a Nikon Eclipse Ti-E microscope with ×60 oil objective (NA 1.4) and A1R confocal, employing 488/647 nm lasers at 50 × 50 nm resolution (line-serial mode). Z-stacks were acquired via NIS-Elements AR. Quantitative analysis involved at least 2 blinded observers. For P2Y12R expression, single CLSM planes (avoiding top/bottom 40 µm) captured full slice cross-sections. Microglial profiles (somata, thick/thin processes) identified by TMEM119/CX3CR1-GFP were outlined, expanded 250 nm inward/outward to create 500 nm-wide ROIs. P2Y12R intensity per membrane unit was calculated as (integrated density / ROI length). Synapse density used vGluT1/Homer1 (glutamatergic) and vGAT/Gephyrin (GABAergic) markers. ROIs

avoided somata, and presynaptic signals (validated by postsynaptic colocalization) were measured as integrated densities in Fiji.

3.8. Time-lapse imaging of extracellular ATP and analysis of microglial responses

ATP1.0$^{\Delta Vglut1}$ mice (P19–20 or P67–74 days) were used for ex vivo two-photon imaging. Acute slices were prepared as previously described (5 slices/brain), containing hippocampal and cortical regions. Each slice was divided into two separate groups: one half imaged in hippocampal CA3, the other in cortical layer 2-3 (256×128 µm windows). The first slice was imaged within 8–13 minutes of sectioning, subsequent slices were incubated at room temperature (~20°C) and imaged hourly. Per slice, 10 minutes of imaging (0.5 frame/s) preceded z-stack acquisitions (3 µm steps, ~3–4 minutes). For imaging, a Nikon Eclipse FN1 microscope was used with A1R MP+ multiphoton system, Chameleon Vision II Ti:Sapphire laser (680–1080 nm), and ×25 water-dipping objective (NA 1.1, WD 2 mm). Excitation was at 920 nm and captured with 550/88 nm emission filter and GaAsP NDD PMT detector. recordings were analyzed in NIS-Elements 5.42.02 and ImageJ 1.53t. Mean Fluorescent Intensity (MFI) decreases were measured in flash-free zones (12.5×12.5 µm ROIs; 4/slice). Z-stacks quantified signal decay over time/depth using three 25×50 µm ROIs/slice. ATP flashes were manually identified at peak intensity for size, intensity, duration, rise/decay analysis. For microglial ATP response studies, CX3CR1-cre/tdTomato mice (P96–119) received bilateral AAV9-hsyn-cATP1.0 injections (3×100 nL; 1×10^{13} vg/ml) at lateral cortex coordinates (AP:3, ML:3.6, DV:4/3.2/2.5 mm). Slices prepared 5–7 weeks post-injection were imaged similarly (256×128 µm, 0.5 frame/s, three 4 µm Z-steps) at 930 nm excitation. ATP event properties and microglial displacement were extracted from max-intensity projections. Microglial process movement (% baseline change) was calculated: baseline = 100 s pre-ATP signal; response = peak signal near ATP event or 100 s average post-event if no peak. Some slices were pre-treated with 4 µM PSB0739 or 10 µM AZD8797 for 5 minutes. ATP sensor calibration used patch pipettes puffing ACSF with 10 nM–5 µM ATP. K-means clustering was employed in Python 2.7.0 by using scikit-learn's StandardScaler and Kmeans algorithms.

3.9. Selective depletion of microglia

$CX3CR1^{+/GFP}$ or C57B1/6J littermates received either control diet or PLX3397-containing diet for three weeks to establish microglia-depleted cohorts. Additional 50 µm sections were obtained from immersion-fixed or perfusion-fixed acute slice preparations through re-sectioning. Depletion efficacy was verified by confocal laser-scanning microscopy of native GFP microglial signals, with total cell counts (via Fiji counting tool) compared across identical cortical/hippocampal regions throughout the full depth of slice preparations.

3.10. Whole-cell patch-clamp recordings of microglia

Standard protocols for patching microglia were followed[197]. After designated incubation periods, slices were individually transferred to a submerged recording chamber with constant carbogenated (95% O_2/5% CO_2) ACSF perfusion at 3–3.5 ml/min. ACSF was maintained at 300–305 mOsm and continuously saturated with carbogen. Recordings occurred at 33–34°C using a dual-flow heater (Supertech Instruments). The pipette solution contained (in mM): 120 KCl, 1 $CaCl_2$, 2 $MgCl_2$, 10 HEPES, and 11 EGTA (pH 7.3, 280–300 mOsm), with pipette resistances of 3–6 MΩ. Cells were visualized under an Olympus BX61WI upright microscope with IR-DIC optics and UV illumination, targeting GFP-positive microglia >50 µm below the slice surface. Initial voltage-clamp at −40 mV facilitated gigaseal formation. After achieving whole-cell configuration, series resistance was monitored with only <5% variation required as a criteria for enabling analysis. Resting membrane potential was measured in current-clamp mode (0 pA, 10–15 s), averaging a 5-s stable segment. Cells then received current-step trains (−2 to −10 pA in 2 pA increments, 10 ms duration, 100 ms intervals). Input resistance was calculated via Ohm's law from voltage-current relationships. Recordings used a Multiclamp 700B amplifier, digitized at 10 kHz (National Instruments USB-6353 DAQ), acquired with custom C#.NET/VB.NET software, and analyzed using Delphi/Python tools.

3.11. Perforated patch-clamp recordings of microglia

Slices were incubated for at least 1 hour before individual transfer to a submerged recording chamber with carbogenated (95% O_2/5% CO_2) ACSF perfusion at 3-3.5 ml/min. Normotonic ACSF (300-305 mOsm) and hypotonic ACSF (50% dilution) were

maintained under carbogen saturation. Recordings occurred at room temperature. Daily-prepared gramicidin-B stocks (100 mg/ml in DMSO) were diluted to 100 µg/ml in filtered pipette solutions containing 100 µM Alexa Fluor 488 for membrane integrity monitoring. Borosilicate pipettes were prefilled with gramicidin-free solution, then backfilled with gramicidin/Alexa-488 solution (in mM: 120 KCl, 1 $CaCl_2$, 2 $MgCl_2$, 10 HEPES, 11 EGTA; pH 7.3, 280-300 mOsm; resistance 3-6 MΩ). Cells were visualized under an Olympus BX61WI microscope (IR-DIC/UV optics). At the beginning of the incubation period, a solution of 25 µM/ml Alexa-594 conjugated isolectin B4 (microglia-selective marker: I21413, ThermoFisher) dissolved in ACSF was pipetted on top of each slice (15 ml/slice) to visualize microglial cells. The Alexa-488 signal was monitored continuously to exclude membrane-ruptured cells. Initial voltage-clamp at -40 mV preceded perforation (35-50 MΩ series resistance, typically achieved 25-30 min post-seal). Recordings were required to have below <15% variation in series resistance to pass for the analysis of current responses. After perforation, resting potential was measured in current-clamp (0 pA, 2-5 s). Voltage-step trains (-140 to 60 mV, 20 mV increments, 100 ms duration, 3 repeats, 2000 ms intervals) were applied in normotonic ACSF and after 5 min hypotonic perfusion. Data acquisition used a Multiclamp 700B amplifier digitized at 10 kHz (National Instruments USB-6353) with custom C#.NET/VB.NET software. Steady-state currents (last 40 ms of steps) were extracted for I-V curve analysis (slope between -40 mV and 0 mV) using Delphi/Python software.

3.12. LFP recordings of spontaneous SWR activity

Acute slices (450 µm thick, 6 per animal) were prepared pairwise from control and microglia-depleted animals daily using identical solutions and equipment. To minimize preparation-related artifacts, the slicing sequence and incubation chambers were alternated between groups across consecutive recording days. Each experimental group included littermate controls. After ≥1 hour incubation, slices from both conditions were transferred pairwise to a dual-perfusion recording chamber for simultaneous local field potential (LFP) measurements. Slices rested on a metal mesh with ACSF flowing above and below (3–3.5 ml/min per channel) at 33–34°C (temperature control with Supertech Instruments). The chamber position for each condition was alternated between recordings. LFP recordings used ACSF-filled patch pipettes (3–6 MΩ) positioned at 80–100 µm depth in the CA3 pyramidal layer for both conditions. Data acquisition employed

a Multiclamp 700B amplifier, digitized at 10 kHz (National Instruments USB-6353 DAQ), and recorded via custom C#.NET/VB.NET software.

3.13. Digital signal processing and SWR analysis

All data underwent offline processing and analysis using custom software developed in Delphi 6.0 and Python 2.7.0. Signals were phase-preserved through two-way RC filtering. Sharp wave ripples (SWRs) were pre-detected on 30 Hz low-pass-filtered recordings using thresholds of 2–3 standard deviations (SD). Recordings without detectable events at 2 SD were classified as SWR-negative. All automated detections were manually verified. Detected SWRs were analyzed measuring sharp wave amplitude (peak amplitude on low-pass-filtered traces), SWR rate (inter-sharp wave intervals), and ripple peak amplitude (the height of peaks on 200 ± 30 Hz bandpass-filtered traces). The ripple peak nearest to each SWR maximum served as the trigger for phase-preserved averaging. Ripple amplitude was derived from the peak of the absolute bandpass signal after low-pass filtering. For quantification, approximately 100 consecutive events showing the highest amplitude values throughout each recording were selected.

3.14. Quantification and statistical analysis

All quantitative analyses were performed under blinded conditions. Biological replication was achieved through multiple animal-derived preparations, with pooled results presented in figures. Predefined exclusion criteria for slice quality (no visible macroscopic injury due to excess mechanical stress or mishandling) and immunostaining integrity (evident non-specific staining) were applied. Data normality was assessed via Shapiro-Wilk testing to determine appropriate parametric or non-parametric analyses. For two independent groups, Student's t-test or Mann-Whitney U-test was used. Three or more groups were analyzed with one-way ANOVA, two-way ANOVA, or repeated-measures ANOVA, followed by Dunn's, Dunnett's, or Tukey's post-hoc tests. All statistical analyses used GraphPad Prism 10.0.0 (GraphPad Software, Boston, MA). Data are presented as mean ± SEM or median (Q1-Q3), with significance defined as $p < 0.05$ and denoted as: ns ($p > 0.05$), * ($p < 0.05$), ** ($p < 0.01$), *** ($p < 0.001$), **** ($p < 0.0001$).

3.15. List of antibodies

Table 1: List of primary and secondary antibodies

Primary antibodies	**host**	**source**	**catalog nr.**	**RRID**
Gephyrin	Mouse	Synaptic Systems	147 021	AB_2232546
GFP	Chicken	Invitrogen	A10262	AB_2534023
Homer1	Rabbit	Synaptic Systems	160 003	AB_887730
IBA1	Guinea pig	Synaptic Systems	234004	AB_2493179
Kv2.1	Mouse	NeuroMab	75-014	AB_10673392
P2Y12R	Rabbit	Anaspec	AS-55043A	AB_2298886
TMEM119	Chicken	Synaptic Systems	400 006	AB_2744643
vGAT	Guinea pig	Synaptic Systems	131 004	AB_887873
VGLUT1	Guinea pig	Synaptic Systems	135 304	AB_887878

Secondary antibodies	**host**	**source**	**catalog nr.**	**RRID**
Alexa 488 Streptavidin	-	-	S-11223	-
Alexa 488 anti-chicken	donkey	Jackson ImmunoResearch Labs	703-546-155	AB_2340376
Alexa 488 anti-guinea-pig	donkey	Jackson ImmunoResearch Labs	706-546-148	AB_2340473
Alexa 488 anti-guinea-pig	donkey	Jackson ImmunoResearch Labs	706-546-148	AB_2340473

Alexa 488 anti-mouse	donkey	Thermo Fisher Scientific	A-21202	AB_141607
Alexa 488 anti-rabbit	donkey	Jackson	711-546-152	AB_2340619
Alexa 594 anti-guinea-pig	goat	LifeTech	A11076	AB_141930
Alexa 594 anti-mouse	donkey	Invitrogen	A-21203	AB_141633
Alexa 594 anti-rabbit	donkey	LifeTech	A21207	AB_141637
Alexa 647 anti-chicken	donkey	Jackson ImmunoResearch Labs	703-606-155	AB_2340380
Alexa 647 anti-rabbit	donkey	Jackson ImmunoResearch Labs	711-605-152	AB_2492288
Alexa 647anti-guinnea-pig	donkey	Jackson ImmunoResearch Labs	706-606-148	AB_2340477
Biotinylated anti-chicken	goat	Vector Laboratories	BA-9010	AB_2336114

4. Results

4.1. Migratory behavior and process polarization

4.1.1. Microglia translocate towards the top surface of slice preparations

We first investigated how injured sites of acute slice preparations (top and bottom surface of the slices) influence microglial cell body distribution without any additional damage inflicted upon the tissue. To ensure consistency across all observations, we employed a highly controlled preparation and incubation protocol, optimized for studying spontaneously occurring SWR activity (Figure 1a). We routinely prepared standardized, 300 µm-thick acute hippocampal slices from the same depth (within 3.44 – 1.24 mm interaural) obtained from CX3CR1$^{+/GFP}$ microglia reporter mice (P35 days old). To examine time-dependent effects, tissue samples were immersion-fixed at specific time points during incubation (0 min, 20 min, 1 hour, 2 hours, 5 hours). Within experiments, we distributed slices from different depths evenly across the specified time-points, in order to counter any artefact that might be introduced by a non-randomized sampling. After fixation, slices were washed with PB and embedded into agarose blocks. To capture microglial distributions along the depth of the slices, the preparations within the agarose block were resliced into 50 µm-thick sections using a vibratome. These sections were then mounted onto glass slides (Figure 1b), and intrinsic microglial fluorescence (CX3CR1$^{+/GFP}$) was captured via a laser confocal system. To quantify microglial cell body distribution and process remodeling, maximum intensity projections (MIP) of confocal stacks encompassing the entire tissue thickness (50 µm) were analyzed. Cell bodies were identified and masked using Fiji's "Analyze Particles" plugin, which enabled automated cell counting. These masks were then subtracted from the original images, allowing for independent analysis of microglial processes. As a validation step, we measured the average thickness of acute slices across the entire incubation period (mean ± SD: 262 ± 7 µm) and found no significant differences between groups (Kruskal–Wallis test, $p > 0.05$). For spatial quantification, we applied a standardized measurement grid across the full thickness of each cross-section, dividing it into seven equal zones (Figure 1c). Microglial cell body counts, and fluorescent intensity measurements of microglial processes were performed within each zone. Process area coverage was determined by

binarizing the images, masking out cell bodies, and measuring the percentage of the area occupied by microglial processes.

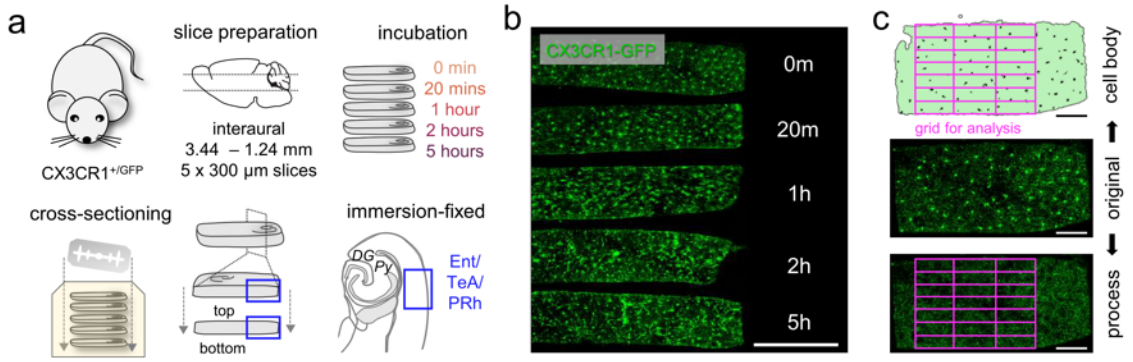

Figure 1: Paradigm for investigating microglial translocation in acute slice preparations. ***(a)*** *CX3CR1$^{+/GFP}$ littermates (males) were used to create slice preparations. Slices were immersion-fixed at different time-points, embedded in agarose blocks and re-sectioned. Ent/TeA/PRh areas were investigated.* ***(b)*** *Examples of maximum intensity projection images of the analyzed cross-sections preserving top/bottom directionality. Scale: 500 µm* ***(c)*** *Original images were processed in Fiji to only contain cell bodies or processes, then a grid (violet) was used for the systematic quantification of cell body (top) and process distributions (bottom). Scale: 100 µm.*

Our findings indicated that microglial cell bodies rapidly start to migrate towards the top surface of acute slice preparations, with most pronounced changes occurring at the superficial layer (Figure 2a). Over the course of 5 hours, the density of microglial cell bodies in this region increased by 75% (two-way ANOVA, $p < 0.001$). Notably, after just 2 hours of incubation, the uppermost layer exhibited a 42% higher density of cell bodies compared to the bottom layer (Figure 2b, $p < 0.01$). This was a surprising observation, since 1,5-2 hours of recovery spent in the incubation chamber is commonly considered to be the earliest time-point for starting measurements during acute slice experimentation. Importantly, the total number of microglia within the entire depth of cross-sections remained stable throughout the experiments (43.07 cells / grid at 0 min vs. 41.50 cells / grid at 5 hours; $p = 0.788$), indicating that cell loss did not contribute to the observed redistribution. Interestingly, we did not observe significant changes at the bottom region

of slices. We also wanted to explore potential signaling mechanisms driving microglial displacement, so we tested two well-established pathways: P2Y12 receptor (P2Y12R) signaling and fractalkine receptor (CX3CR1) signaling. Pharmacological inhibition of P2Y12R with PSB0739 had only a little effect on microglial translocation, whereas microglial migration towards the surface was significantly impaired in CX3CR1-knockout slices ($p < 0.0001$), highlighting the critical role of fractalkine signaling in this process (Figure 2c).

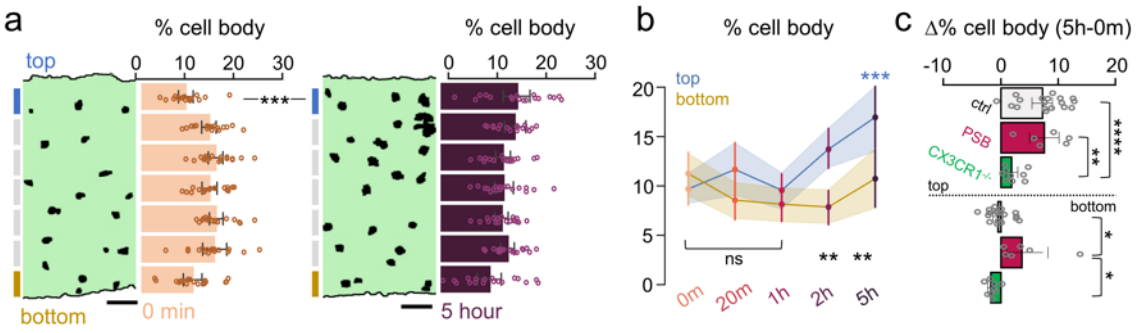

Figure 2: Microglial cell bodies translocate towards the top surface of acute slice preparations. ***(a)*** *Representative sections of processed images from acute slice cross sections. Black dots indicate microglial cell bodies. Rectangles on the left indicate layers of the grid used for analysis (top: blue, bottom: yellow) Scale: 50 µm. Vertical bar plots show cell body % with respect to grid layers. N = 3 animal, n = 3 slices/animal; P35 days; mean ± SEM, two-way ANOVA, Tukey's multiple comparison, F(24, 408) = 2.305, p = 0.0005.* ***(b)*** *Cell body distribution changes captured in time within the top (blue) and bottom layers (yellow). N = 3 animal, n = 3 slices/animal; P35 days; mean ± SEM. Blue stat.: compared to 0-min, black stat.: top/bottom means, two-way ANOVA, Tukey's multiple comparisons, F(24, 408) = 2.305, p = 0.0005.* ***(c)*** *Cell body distribution changes in control, PSB-treated and CX3CR1$^{-/-}$ conditions. Ctrl: N = 3 animal, n = 3 slices/animal; PSB: N = 2 animal, n = 3 slices/animal; CX3CR1$^{-/-}$: N = 3 animal, n = 3 slices/animal; P35 days; mean ± SEM; two-way ANOVA, Tukey's multiple comparison, F(2,60) = 13.65, p < 0.0001.*

4.1.2. Microglial processes polarize towards the top surface of slices

Since microglial processes move at rates that are orders of magnitude faster than their cell bodies[87], we next examined process remodeling in the same cross-sections. As it was described above, here we examined the % of the area occupied by microglial processes within a single grid layer (microglial cell bodies were masked out). Similarly to cell body redistribution, we observed a robust increase in microglial process density within the uppermost layer of slices (Figure 3a). Process coverage in this region increased by 21% within 2 hours ($p < 0.05$) and reached a 29% increase after 5 hours ($p < 0.0001$). Conversely, the bottom layer exhibited a 15% reduction in process density as early as 2 hours post-slicing ($p < 0.05$) and a 23% decrease by the 5-hour mark ($p < 0.0001$). Inhibiting P2Y12R or disrupting CX3CR1 signaling prevented these changes, further supporting a key role for fractalkine signaling during the redistribution of microglial processes.

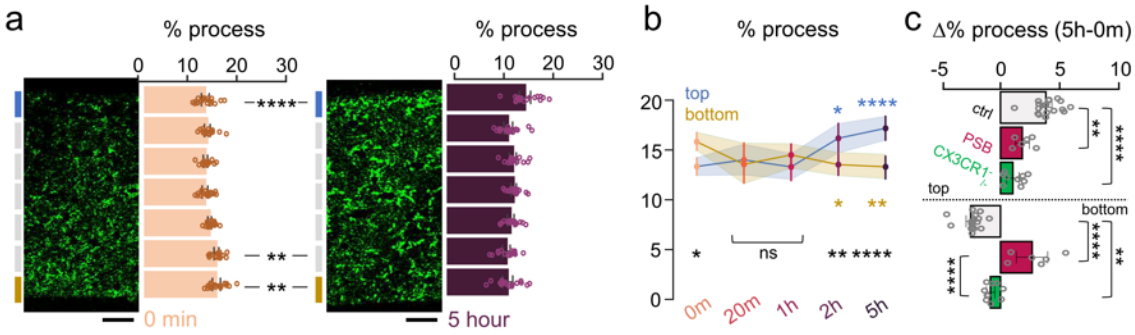

Figure 3: Microglial processes redistribute towards the top surface. (a) *Representative sections of processed images. Fluorescent signal (CX3CR1$^{+/GFP}$, green) indicates microglial processes without their cell bodies. Rectangles on the left indicate layers of the grid used for analysis (top: blue, bottom: yellow) Scale: 50 µm. Vertical bar plots show the % of the area occupied by processes with respect to grid layers. N = 3 animal, n = 3 slices / animal; P35 days; mean ± SEM, two-way ANOVA, Tukey's multiple comparison, F(24,408) = 4,766, p < 0.0001.* ***(b)*** *Process distribution changes captured in time within the top (blue) and bottom layers (yellow). N = 3 animal, n = 3 slices/animal; P35 days; mean ± SEM. Blue and yellow stat.: compared to 0-min, black stat.: top and bottom means compared, two-way ANOVA, Tukey's multiple comparisons, F(24,408) = 4,766, p < 0.0001.* ***(c)*** *Process distribution changes in control, PSB-treated*

and CX3CR1$^{-/-}$ conditions. Ctrl: N = 3 animal, n = 3 slices/animal; PSB: N = 2 animal, n = 3 slices / animal; CX3CR1$^{-/-}$: N = 3 animal, n = 3 slices/animal; P35 days; mean ± SEM; two-way ANOVA, Tukey's multiple comparison, F(2,60) = 17.23, p < 0.0001.

4.1.3. Process polarization captured by 2-photon time-lapse imaging

We also wanted to capture these microglial responses in real time, so we performed continuous time-lapse confocal imaging of CX3CR1$^{+/GFP}$ labelled microglia within acute slices for at least 6 hours after preparation. Acute slices were prepared in exactly the same manner as for the previous experiment (Figure 4a). These recordings revealed that individual microglial cells indeed exhibit directed movement towards the top surface of the tissue, in agreement with our quantitative measurements (Figure 4b). Based on these observations, we concluded that cell bodies and processes display robust coordinated migration patterns in acute slices, as they are collectively shifting towards the uppermost layer of the slice, as supported by both our anatomical and real-time imaging data.

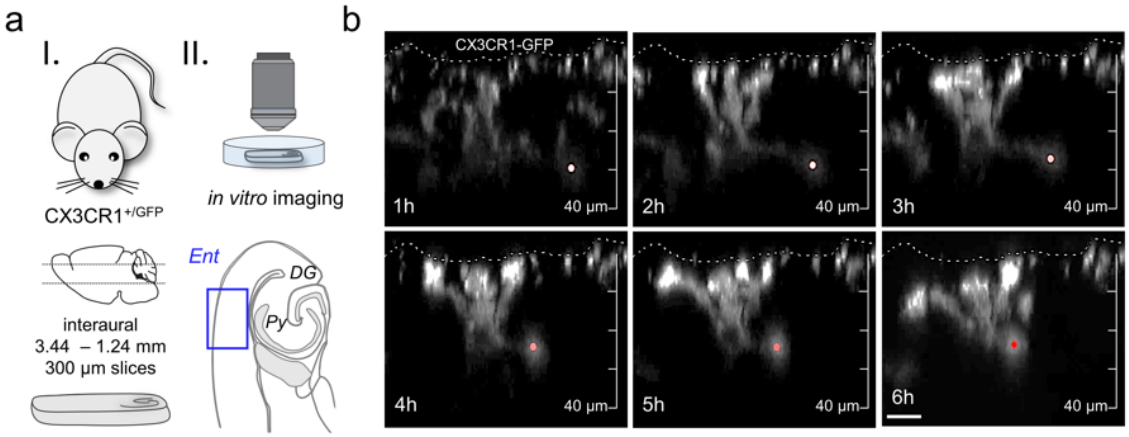

Figure 4: Real time imaging of cell body and processes migration. (a) *We used CX3CR1$^{+/GFP}$ mice (males, P45–80 days) to create 300 µm thick acute slice preparations. Subsequently, slices were immediately transferred into a recording chamber, where microglial cell bodies and processes were continuously tracked via 2P imaging for 6 hours.* ***(b)*** *Representative images taken from time-lapse 2P imaging sessions: Translocation of a single microglial cell body (indicated with red dot) and its processes (CX3CR1$^{+/GFP}$, white) towards the surface of the acute slice preparation (stripped white line). Scale: 10 µm.*

4.1.4. Time-lapse imaging reveals rapid changes in microglia morphology

It is well documented, that upon injury or in certain pathologies microglia can transform their morphology into a more amoeboid shape by retracting their processes, which corresponds to a less ramified shape, also referred to as the 'activated' phenotype[44]. In this case, they display a dramatically decreased number of process endings, which probably enables the migration and reorganization of cell bodies and processes towards injured sites. We hypothesized that microglia in acute slices are likely to display this phenotypic transformation after slice preparation, considering their previously observed cutting-induced migratory response (Figure 2-3). This notion was supported by looking at individual microglia morphologies in our time-lapse imaging recordings, where we indeed observed robust transitioning of microglia morphology to a more "activated" phenotype. (Figure 5a). We initially decided to also confirm this quantitatively, by comparing the total percentage of area covered by processes (Figure 5b) in the cross-sections of acute slices used for the investigation of process redistribution (Figure 3a). This comparison showed that the area covered by microglial processes are significantly reduced when comparing acute slices at 0 min with slices that were incubated for 5 hours (Mann–Whitney (two-sided), $p < 0.0001$).

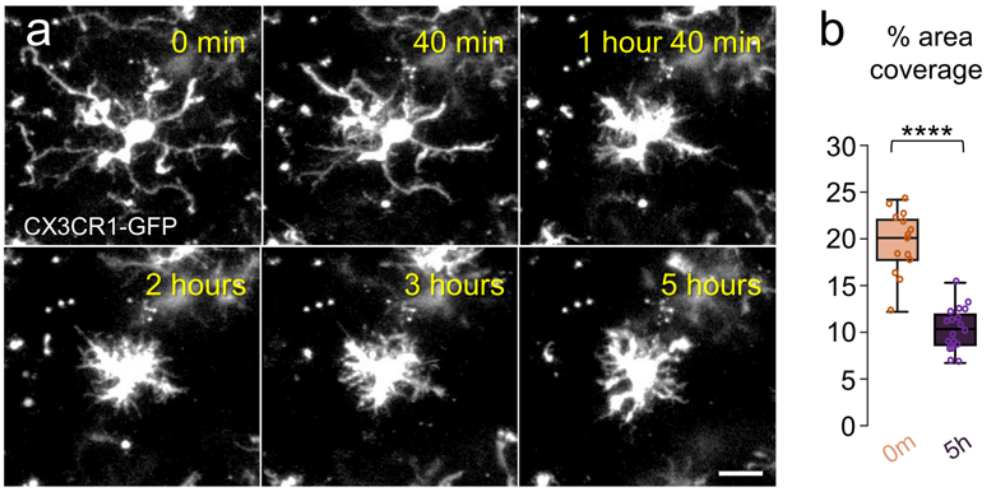

Figure 5: Time-lapse imaging of microglial morphological transformation. (a) *$CX3CR1^{+/GFP}$ signal of individual microglia during time-lapse imaging in acute slice*

preparations. Scale: 10 µm. ***(b)*** *Area covered by microglia processes at 0 min (orange) vs. 5 hours (purple) spent in incubation. N = 3 animal, n = 3 slices/animal, P35 days; Mann–Whitney (two-sided), p < 0.0001. Boxes: interquartile range, whiskers: min–max, vertical bar: median.*

4.1.5. Framework for quantifying morphological features of microglia

To systematically characterize the extent and timing of microglial transformations, we decided to perform a detailed time-course analysis. Brain slices were obtained from CX3CR1$^{+/GFP}$ mice (P35 and P95 days, two separate experiments) and immersion-fixed at time points as described earlier (Figure 6a). In this case, a separate set of mice from the same age group were transcardially perfused to obtain control samples from the same regions, to gain tissue samples that represented an undisturbed, more physiological state for comparison (Figure 6a, bottom). To preserve fine structural details, fixed slices were embedded in agarose and re-sectioned to obtain the middle 100 µm section for each slice (Figure 6b). This step was necessary to exclude regions of the tissue that were within the vicinity (~40 µm) of acute slice surfaces during the incubation process, as we saw robust migratory behavior (Figure 2-3) within these areas which would have confounded our results. After this step, slices were immuno-stained with DAPI to label microglial cell bodies, and with IBA1 to increase the visibility of fine processes. To minimize potential distortions due to tissue mounting, all preparations were maintained in a free-floating state until imaging. Imaging was performed in 0.1 M PB using a 60× water immersion objective. Image stacks were collected at a high resolution (0.2 µm/pixel resolution with a Z-step size of 0.4 µm). We acquired confocal z-stacks from cortical (Ent, TeA, PRh) and hippocampal (CA2-3 stratum radiatum) regions from all time-points (Figure 6c), and applied an automated, unbiased morphological analysis software[184] to assess microglial structural changes. This open-source MATLAB-based software was designed to reconstruct the 3D-architecture of individual microglia and extract 59 parameters describing their morphological feature, by applying automated cell segmentation (Figure 6c, 1-2.), watershed-based separation (Figure 6c, 3.), and skeletonization (Figure 6c, 4.) during analysis.

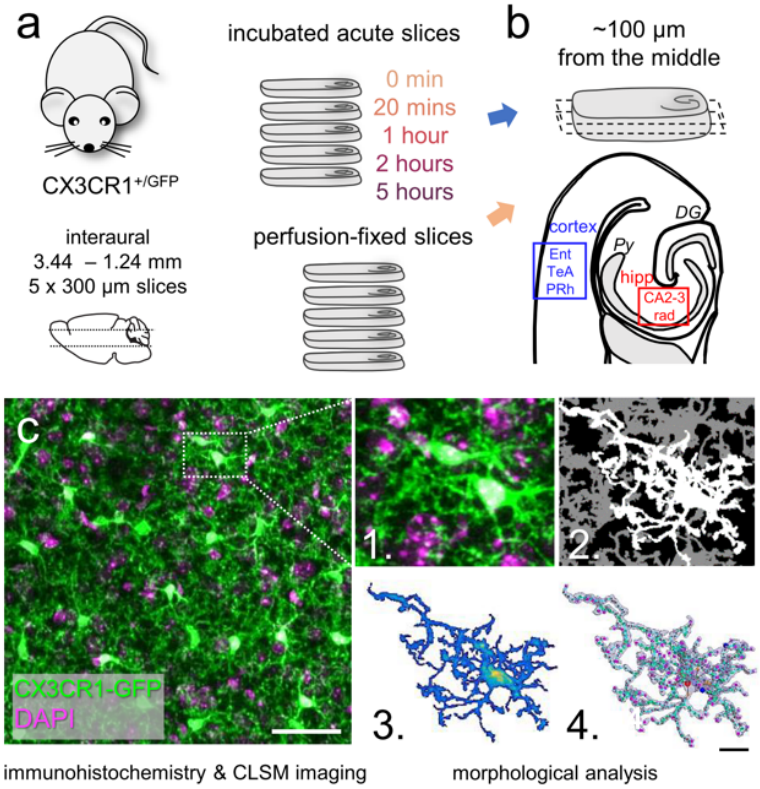

Figure 6: Framework for quantifying morphological features of microglia. ***(a)*** *Acute slices were obtained from CX3CR1$^{+/GFP}$ (male littermates) and immersion-fixed after different time-points (blue arrow), or slices were obtained from perfusion-fixed animals (orange arrow).* ***(b)*** *Slices were re-sectioned in order to obtain the middle region (100 µm), and measurements were performed in Ent, TeA, PRh cortical and CA2-3 stratum radiatum hippocampal regions.* ***(c)*** *Immuno-stained images (Scale: 20 µm) were analyzed in an automated pipeline: (1-2.) images are segmented into separate cells. (3.) Cells are segmented into different compartments: cell body (yellow) and processes (blue) of individual cells are identified. (4.) 3D-models of individual microglial skeletons are constructed (right, bar: 10 µm) (two independent experiments, N = 4–4 animal, n = 3 slices/animal). (Scale: 50 µm).*

4.1.6. Quantitative morhological features indicate rapid transformation of microglia towards an ameboid shape

We decided to use the parameters called 'sphericity' and '# of ending nodes' for quantification (Figure 7a-b), as these were previously described as reliable indicators capable of capturing phenotypic transformation[184]. In this case, the 'sphericity' parameter quantified how amoeboid the structure of a given microglia is, where higher values correspond to a more spherical shape (Figure 7b, black values). The # of ending nodes parameter simply quantified the number of process endings for each microglia based on the 3D-reconstructions (Figure 7b, violet values).

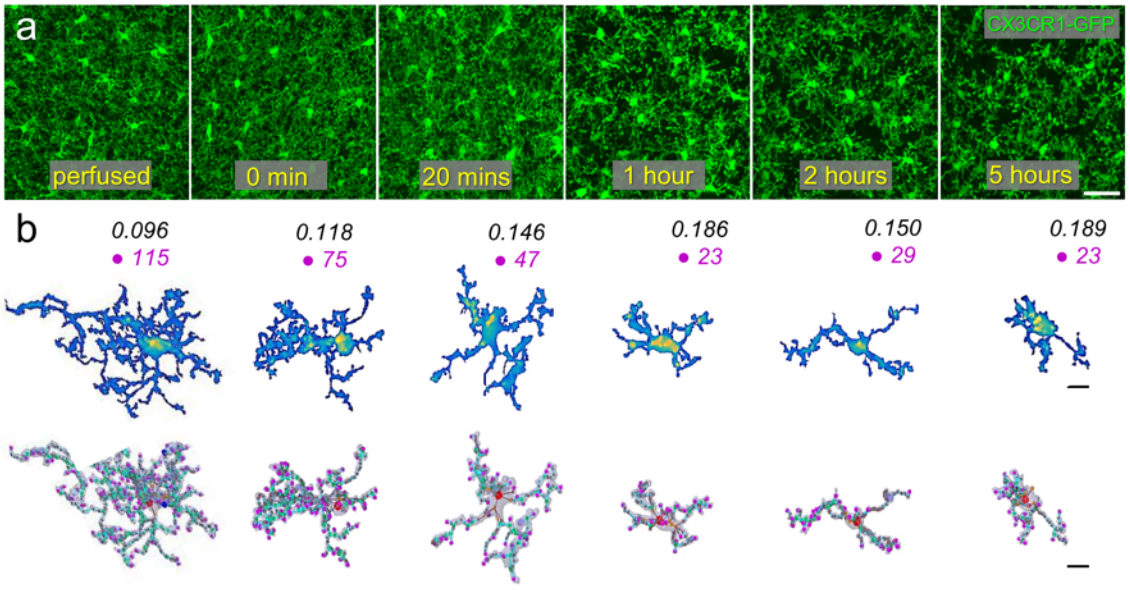

Figure 7: Rapid transformation of morphological features in acute slice preparations. ***(a)*** *Maximum intensity projections of analyzed z-stacks from the cortex, across the different time point after slice preparation (Scale: 50 µm).* ***(b)*** *Representative examples of individual microglia identified by the analysis tool (yellow: cell body; blue/purple: processes; Scale: 5 µm) with quantified morphological parameters above (sphericity in black and # of ending nodes in violet). Bottom: Reconstructions of skeletons corresponding to the microglial cells above (violet dots: process endings, red dots: cell body, Scale: 5 µm).*

Our observations revealed drastic time-dependent changes in microglial morphology within acute brain slices (obtained from P35 days old animals) on a population level (Figure 8a). Quantitative analysis showed that microglial sphericity values (which increase as cells retract their processes and adopt a more amoeboid shape) doubled between 1- and 2-hours post-slicing in both cortical and hippocampal regions (Fig. 8a, one-way ANOVA, $p < 0.0001$). At the same time, the number of process endings exhibited a striking decline: Within 20 min, process endings dropped by ~50%. By 1–2 hours, process endings had decreased by ~80% compared to baseline levels ($p < 0.0001$). We also investigated whether the observed changes would occur in older mice, by analyzing the time-dependent morphological changes in slices prepared from 95-day-old animals (Figure 8b), and we found that microglial phenotype changes tightly matched those observed in slices from younger animals.

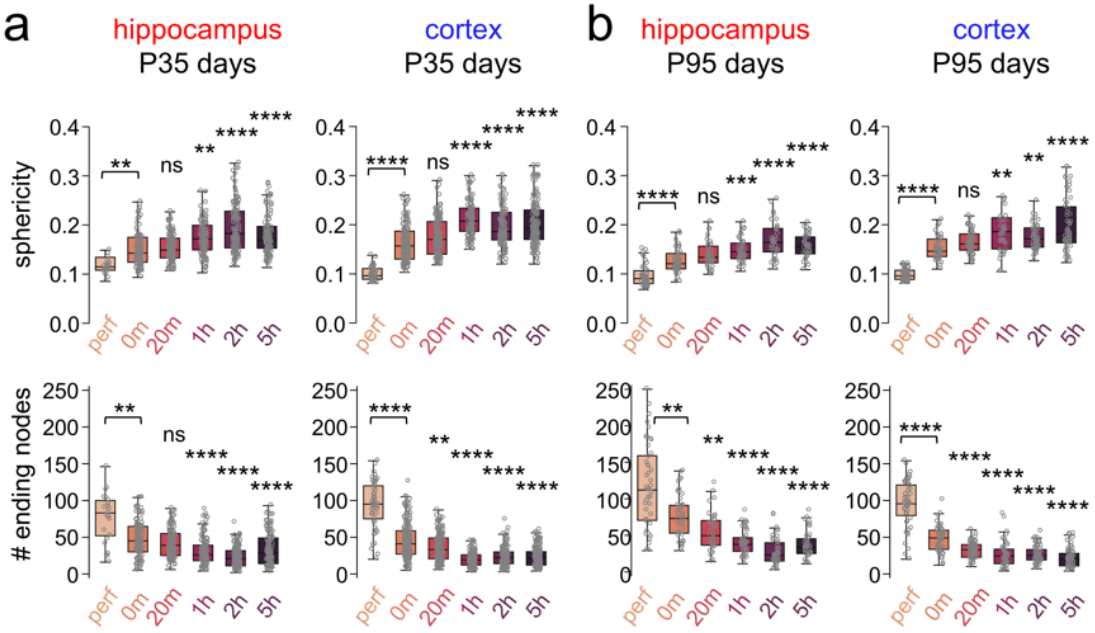

Figure 8: Acute slice microglia rapidly transform their morphology in acute slices. (a) *Top: sphericity values of individual microglia in cortex (blue) and in hippocampus (red) from P35-days-old animals. Bottom: number of process endings / microglia (# of ending nodes). N = 8 animals, one-way ANOVA, Dunnett's multiple comparison, $p < 0.0001$ (comparisons from 20 min to 5 h time-points are made to 0 min) Boxes: interquartile range, whiskers: min–max, vertical bar: median.* ***(b)*** *Same as in (a) for data obtained*

from P95-day-old animals. N = 5 animals, one-way ANOVA, Dunnett's multiple comparisons, p < 0.0001. ***(c)*** *Comparison of Sphericity and # of process endings values between CX3CR1$^{-/-}$ (green), P2Y12R$^{-/-}$ (purple), and WT (grey), N = 3 animal/condition (only males), n = 5 slices/animal, P35 days, two-way ANOVA with Tukey's multiple comparison test, p < 0.0001. Boxes: interquartile range, whiskers: min–max, vertical bar: mean.*

4.1.7. P2Y12R and CX3CR1 pathways modulate phenotypic transition of microglia

We also wanted to investigate the molecular mechanisms which we did earlier during the examination of migratory behavior (Figure 2-3c), namely, purinergic (P2Y12R) and fractalkine (CX3CR1) signaling. In this case, slices from P2Y12R$^{-/-}$ mice showed a significantly reduced magnitude of morphological changes at the 5-hour time point compared to wild-type controls (Fig. 7c, violet, two-way ANOVA). In contrast, slices from CX3CR1$^{-/-}$ mice exhibited accelerated microglial process retraction, reaching peak changes at 2 hours post-slicing, but ultimately converging with control levels by 5 hours (Figure 7c, green, two-way ANOVA). These findings indicate that both P2Y12R and CX3CR1 signaling contribute to the robust microglial response in acute slices, where P2Y12R are likely to occupy a promoting function in microglial remodeling, while CX3CR1 seems to modulate the timing and extent of these changes.

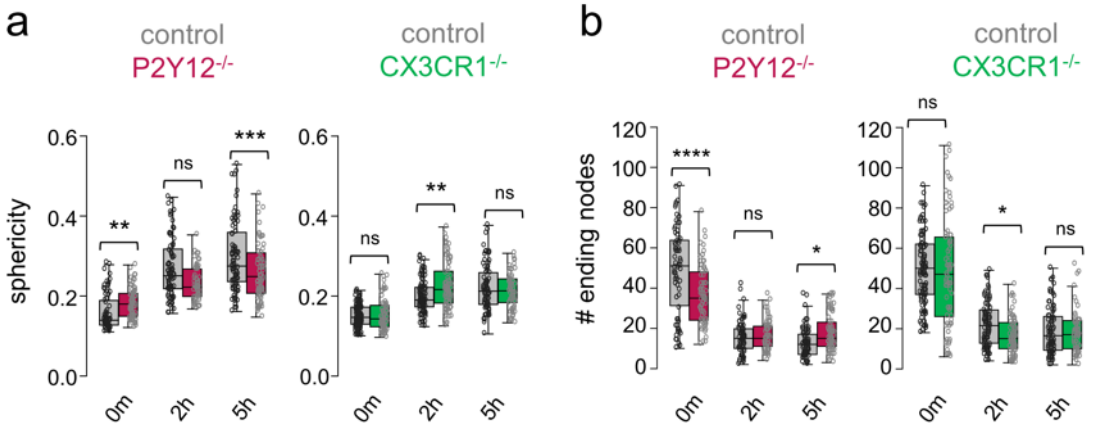

Figure 9: P2Y12R and CX3CR1 pathways modulate phenotypic transition. (a) *Comparison of sphericity values between P2Y12R$^{-/-}$ (purple), CX3CR1$^{-/-}$ (green), and WT (grey) conditions.* ***(b)*** *Comparison of # (total number) of ending nodes between P2Y12R$^{-/-}$ (purple), CX3CR1$^{-/-}$ (green), and WT (grey) conditions. N = 3 animal/condition (only males), n = 5 slices/animal, P35 days, two-way ANOVA with Tukey's multiple comparison test, p < 0.0001. Boxes: interquartile range, whiskers: min–max, vertical bar: mean.*

4.2. Morphological transformation and electrophysiological properties

4.2.1. Framework for comparing acute slice-resident microglia features across different laboratories

Given the widespread use of a huge variety of techniques, tools, solutions and methodologies during acute brain slice experimentation, we wanted to investigate how generalizable our observations were to microglia in acute slices prepared by different laboratories or with different techniques. First, we wanted to investigate slice preparations that are created by independent laboratories, each using their own distinct, but well-established protocols (Figure 10). Initially, we created a standardized protocol for the experiment (Figure 10a) which was sent to the other labs to ensure the synchronization of certain methodological parameters. The protocol contained instructions about the time-points and method of fixation (0 min, 20 min, 1 hour, 2 hours, 5 hours, immersion-fixed), as well as we asked researchers to keep track of surface direction (top/bottom of slices during incubation). We also instructed the other labs to prepare acute slices from the same region and with the same thickness (300 µm-thick acute hippocampal slices from 3.44 – 1.24 mm interaural depth). Importantly, we also specified that each slice should spend 1 hour in 4% PFA, and then transferred into wash plates containing 0.1 M phosphate buffer (PB) and washed with PB 3 times for 10 min. All slices were stored and transported by being submerged under 0.1 M PB, supplemented with 0.05 % sodium azide. Importantly, while each lab maintained its native slicing and incubation methods, all samples underwent identical histological processing, imaging, and analysis in a blinded

manner at our laboratory (as described previously) in order to ensure methodological consistency for the evaluation of differences.

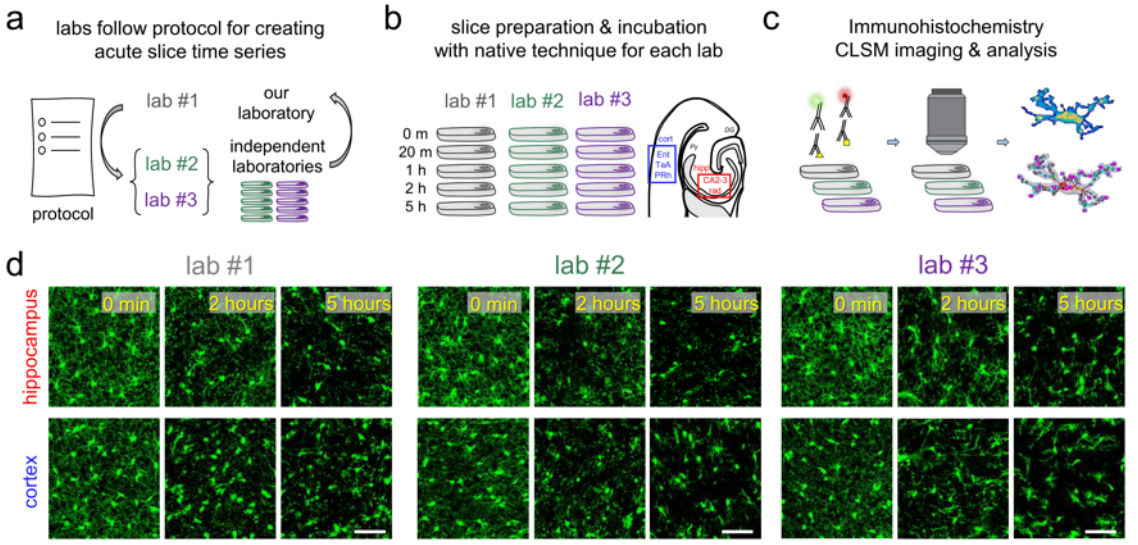

Figure 10: Framework for the blinded comparison of acute slice-resident microglia prepared by different laboratories. ***(a)*** *Schematics of experiment. Laboratories received a protocol to synchronize slice parameters, fixation timepoints and methods, while they were allowed to use their own native acute slice preparation method.* ***(b)*** *Measurements were performed in Ent/TeA/PRh cortical areas, and in CA2-3 stratum radiatum region of the hippocampus from C57Bl/6J animals (only males).* ***(c)*** *Acute slice preparations were sent to our laboratory after preparation for transport where they were treated together during immunostaining, imaging, and morphological analysis.* ***(d)*** *Maximum intensity projections of confocal images showing microglia (IBA1) in the hippocampus (top, red) and in the cortex (bottom, blue). Scale bar: 50 µm. (N = 3-2-2 animal, n = 1 slice/animal/timepoint).*

4.2.2. Microglial phenotypic transformation is similarly prevalent in acute slices prepared by different laboratories

In line with our earlier observations, both the sphericity of microglial cells (Figure 11a) and the total number of ending nodes (Figure 11b) showed closely identical, gradual changes towards an activated phenotype. We also obtained similar results considering

microglial cell body migration and process movements (Figure 11c), suggesting that the observed changes are generalizable features across different laboratories.

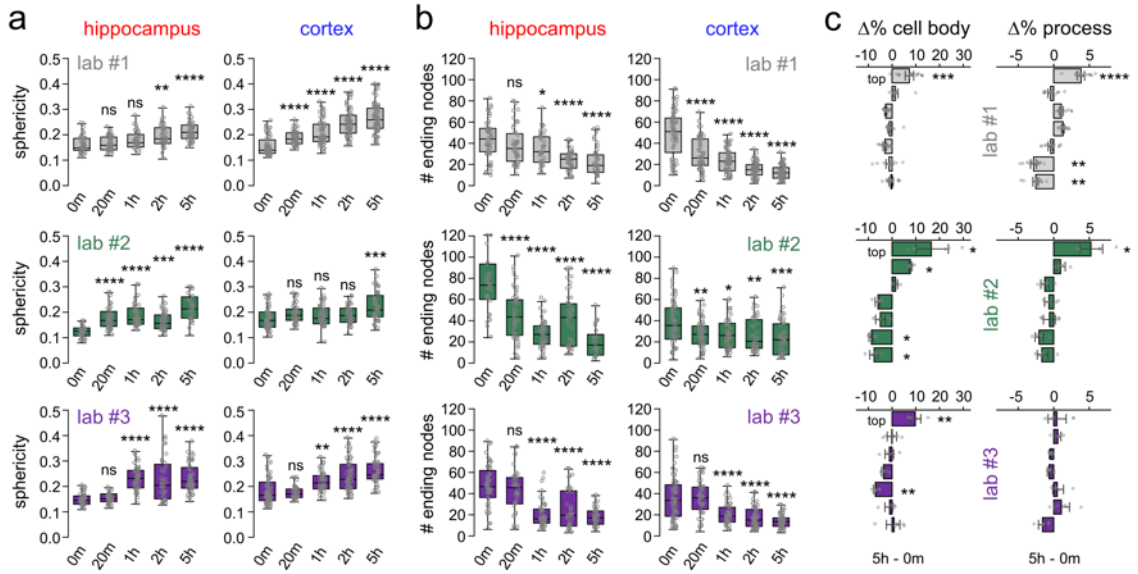

Figure 11: Phenotypic transformation is prevalent in acute slices prepared by different laboratories. ***(a)*** *Quantification of extracted morphological features across different laboratories regarding sphericity in hippocampus (left) and in cortex (right). N = 3 animal/lab1; 2 animal/lab#2; 2 animal/lab#3; n = 3 slices/animal, P65 days, one-way ANOVA with Dunnett's multiple comparison test, p < 0.0001. Boxes: interquartile range, whiskers: min–max, vertical bar: mean.* ***(b)*** *Same as in (a), regarding # (total number) of ending nodes/cell in cortex (left) and in hippocampus (right). N = 3 animal/lab1; 2 animal/lab#2; 2 animal/lab#3; n = 3 slices/animal, P65 days, median ± SEM, one-way ANOVA with Dunnett's multiple comparison test, p < 0.0001. Boxes: interquartile range, whiskers: min–max, vertical bar: mean.* ***(c)*** *Bar plots representing measured changes of microglial cell body numbers (left) and area covered by processes (right) in percentages calculated between 0 min and 5 h across the top and bottom layers of acute slice preparations. N = 3 animal/lab1; 2 animal/lab#2; 2 animal/lab#3; n = 3 slices/animal, P65 days, median ± SEM, two-way ANOVA with Dunnett's multiple comparison test, p < 0.0001, mean ± SEM.*

4.2.3 Phenotypic transformation does not depend on slice thickness or temperature of cutting solution

We went on further to test more parameters that might influence the observed phenotypic changes, so first we examined some modifications in cutting parameters that were common between the laboratories during comparison. We also tested thick acute slices (~450 µm thick) which are regularly used for the investigation of network mechanisms[187,193]. In this case, we found even more pronounced migratory behavior towards the same direction (top surface of acute slices) both considering cell bodies and processes (Figure 12a). While the majority of acute slice studies use ice-cold cutting solutions, in some rare cases, warm temperatures were found to result in more viable cells in the tissue[163,164]. Since temperature fluctuations can also modulate microglial function, we went on to test whether warmer cutting solutions would influence morphological transitions. In this case, we found identical trends to what we saw by using the ice-cold cutting solution (Figure 12a-b), so we concluded that the ice-cold temperature is not a considerable driving cause behind the observed phenotypic transition.

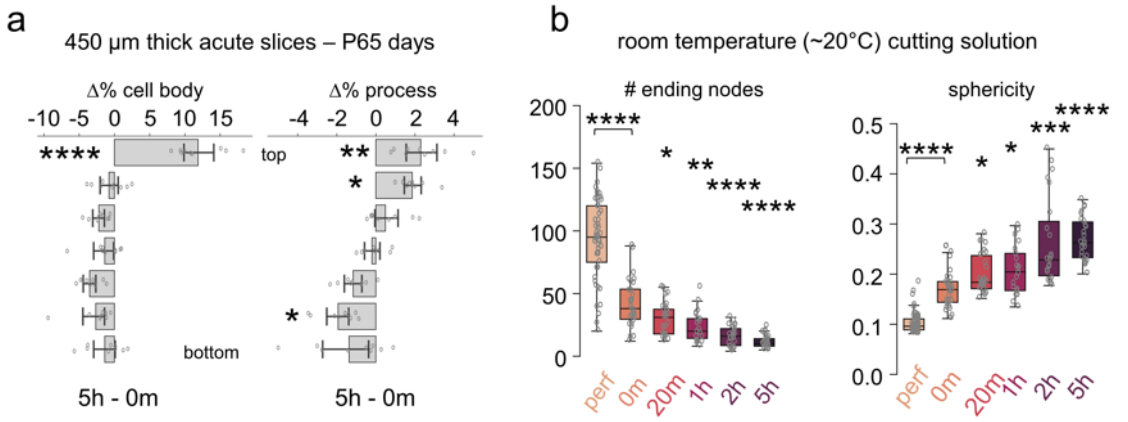

Figure 12: Phenotypic transformation does not depend on slice thickness or temperature of cutting solution. (a) *Bar plots represent measured changes of microglial cell body (left) and area covered by processes (right) in percentages calculated between 0 min and 5 hours across the top and bottom layers of acute slice preparations (~450 µm thick). N=3 animals, n=3 slice/animal, P65 days, mean ± SEM, two-way ANOVA with Tukey's multiple comparison test, p<0.0001.* ***(b)*** *Quantification of extracted*

morphological features from acute slices prepared with room temperature standard ACSF cutting solution, regarding sphericity in cortex (left) and in hippocampus (right). N=3 animals, P65 days, one-way ANOVA with Dunnett's multiple comparison test; asterisks indicate comparison with 0 min values, p<0.0001.

4.2.4. Phenotypic transformation is prevalent in acute slice preparations harvested at earlier developmental stages

Microglia are well known to play important roles during development, which can differ significantly from the functions that are carried out in more adult phases[110]. Importantly, acute slice experimentation is also widely used in developmental research, so we wanted to examine whether phenotypic transformations occur to the same extent in slices harvested earlier during development (P18-20 days). We found identical time-dependent changes in these acute slices as well (Figure 13), which underscored the broad impact of cutting-induced changes that were observed initially.

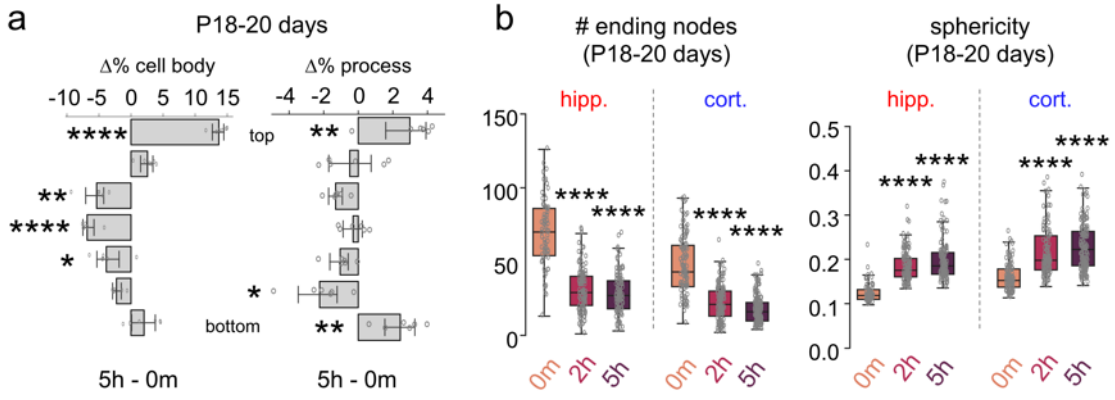

Figure 13: Phenotypic transformation is also prevalent in acute slices harvested at earlier stages (P18-20) during development.(a) *Bar plots represent measured changes of microglial cell body (left) and area covered by processes (right) in percentages calculated between 0 min and 5 hours across the top and bottom layers of acute slice preparations (~300 µm thick). N=3 animals, n=3 slice/animal, P19 days, mean ± SEM, two-way ANOVA with Tukey's multiple comparison test, p<0.0001.* ***(b)*** *Quantification of extracted morphological features from acute slices regarding sphericity in cortex (left)*

and in hippocampus (right). N=3 animals, P18-20 days, one-way ANOVA with Dunnett's multiple comparison test; asterisks indicate comparison with 0 min values, p<0.0001.

We concluded that phenotypic transformation in acute slice preparations is characterized by robust migratory behavior towards superficial layers, paired with increased sphericity and reduced branching, which was also prevalent within the deeper layers of slices. Considering that these changes were highly reproducible across a variety of contexts (different laboratories and experimental conditions), this phenotypic transformation is likely to represent a general response induced by injury-related signals during the slice preparation process, which does not depend on cutting techniques. Furthermore, these results highlighted the important roles of P2Y12R and CX3CR1 signaling pathways in modulating these responses.

4.2.5. Microglia gradually depolarize during phenotypic transformation in acute slice preparations

Functional states of microglia have been shown to be closely linked to changes in their membrane properties. While ramified microglia typically maintain a hyperpolarized resting potential (-40 to -50 mV)[171], they can show chronic depolarization in response to inflammatory signals, such as LPS or pro-inflammatory cytokines[170], which state also correlates with an activated phenotype. First, we wanted to investigate whether slice preparation induces the same response in microglia, so we performed electrophysiological recordings to monitor changes in their membrane properties over the 5-hour long incubation period which we used previously. We prepared acute slice time-series in exactly the same manner as described before from $CX3CR1^{+/GFP}$ animals and performed whole cell patch-clamp recordings on microglia guided by the native GFP signal (Figure 14a) within the CA2-3 stratum radiatum region. We used a special pipette solution optimized for electrophysiological recordings of microglia, which did not contain ATP or its metabolites in order to avoid activation (in mM: 120 KCl, 1 $CaCl_2$, 2 $MgCl_2$, 10 HEPES, and 11 EGTA, pH: 7.3, 280–300 mOsm). Based on general guidelines[172] and on our initial observations concerning superficial layers of acute slices, only cells located deeper than ~50 µm were targeted. All cells were initially in voltage-

clamp mode and held at −40 mV holding potential during the formation of the gigaseal. After the whole-cell configuration was established, resting membrane potential values were measured by changing the recording configuration to current-clamp mode with 0 pA for a short period of time (10–15 s) and evaluated from the recorded signal via averaging a 5 s period. Thereafter, responses to a pulse train of current steps (−2 to −10 pA with 2 pA increments and 10 ms duration) were recorded for the quantification of the input resistance via Ohm's law, based on the slope of voltage responses. After recording, each recorded microglia were separated into 1-hour-long time-bins based on the time elapsed from the cutting to the start of the recording.

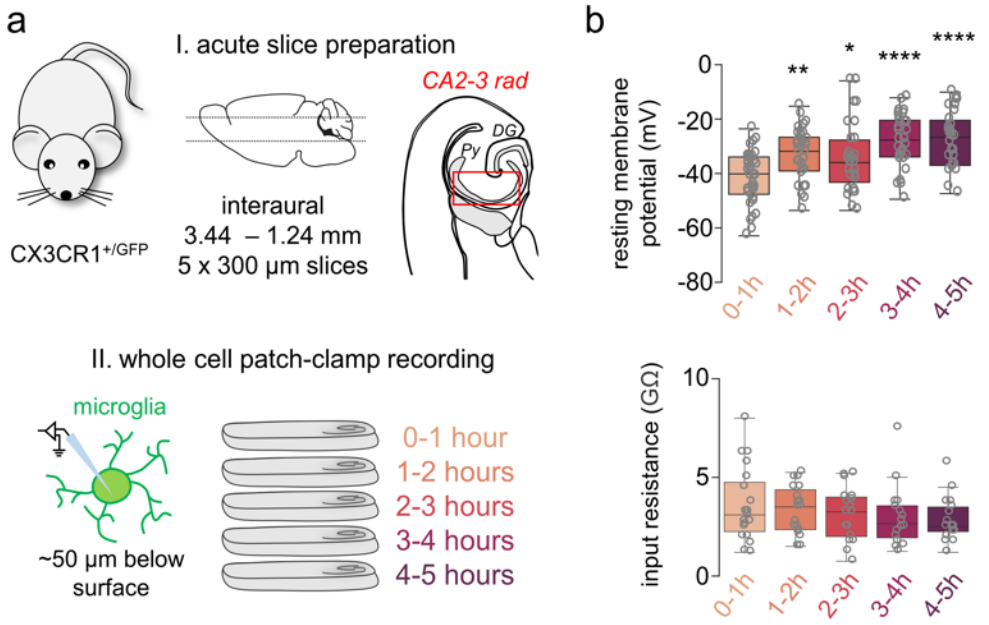

Figure 14: Phenotypic transformation coincides with microglial membrane potential depolarization. ***(a)*** *Acute slices obtained from CX3CR1+/GFP (male/female littermates). Microglia were measured in whole cell patch-clamp, targeted ~50 µm below the surface (CA2-3 stratum radiatum).* ***(b)*** *Resting membrane potential(top)/input resistance(bottom) during recovery. N = 10 animal (7 males, 3 females), n = 5 slices/animal, P90 days; N = 158 cells, one-way ANOVA, Dunnett's multiple comparisons, F(4,150) = 9.768, p < 0.0001 (top), ns (bottom). Boxes: interquartile range, whiskers: min–max, vertical bar: median.*

Our results showed that microglia gradually became more depolarized during the 5 hours of the incubation period (Figure 14b, top), which reached significance as early as the 1-2 hours' time-bin after slice preparation (n= 158 cells, N=10 animals, one-way ANOVA with Dunnett's multiple comparison test, $p<0.01$), while we did not observe significant changes in input resistance (Figure 12b, bottom). These results indicated that the tandem-pore domain halothane-inhibited K^+ channel 1 (THIK-1) - which has been implicated in influencing microglial membrane potential[102] - is likely to be downregulated upon transitioning towards an activated state, which is in line with previous observations[194]. Importantly, THIK-1 function has been shown to influence microglial states mainly under physiological conditions[102], which indicates that microglial membrane properties are likely to be influenced by the activity of other ion-regulating channels after injury or in pathological conditions.

4.2.6. The NKCC1 ion transporter modulates microglial membrane properties both in physiological and pathological conditions

In an earlier study, the Na^+-K^+-$2Cl^-$ cotransporter (NKCC1) has been shown to regulate microglia phenotype and volume during pathological states[195], since its expression and functionality is increased within injured and posttraumatic conditions[196,197]. We were interested in whether the NKCC1 can also influence microglia membrane properties in acute slice preparations in response to injury or due to osmotic stress. To test this, we employed perforated patch-clamp recordings on microglia from both wild-type (WT) and microglia-specific NKCC1 knockout ($NKCC1^{-/-}$) mice. We used this method in order to maintain the intracellular Cl^- concentration unaffected by the pipette solution, providing a more accurate representation of the cells' native state (Figure 15a). Recordings were conducted in voltage-clamp mode at a holding potential of -40 mV, with voltage steps ranging from -140 mV to +60 mV in 20 mV increments, each lasting 100 ms. This setup enabled the construction of I-V plots for individual cells, allowing us to compare membrane properties of WT and $NKCC1^{-/-}$ microglia. To further explore the role of these channels, we exposed the cells to a hypotonic ACSF solution (50% dilution for 5 minutes) in order to induce cellular swelling. This condition is known to activate volume-regulated anion channels (VRACs), which are largely Cl^- permeable[198,199]. By comparing the

current responses under normotonic and hypotonic conditions, we aimed to identify the characteristics of the swelling-induced currents.

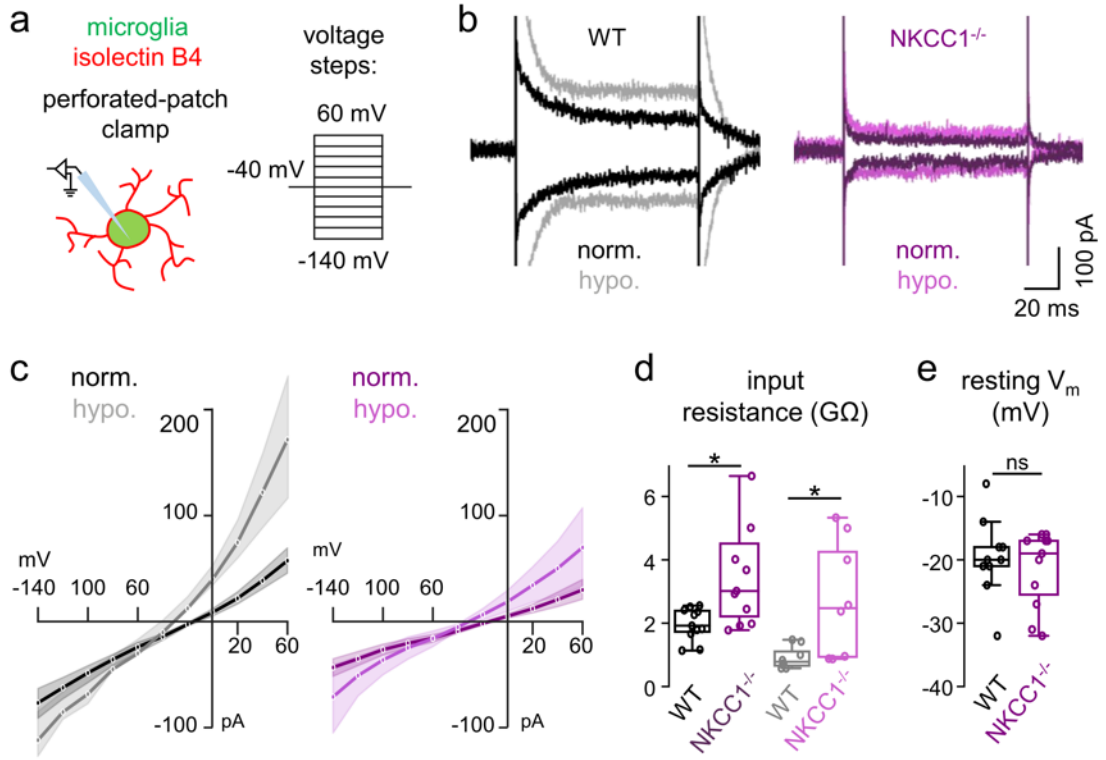

Figure 15: NKCC1 ion transporter modulates microglial membrane properties and phenotype. ***(a)*** *Schematic representation of the experiment. Perforated patch-clamp recordings were performed on isolectin B4–labeled microglial cells in acute hippocampal slice preparations. Current responses to a train of voltage steps were measured in voltage-clamp mode (holding potential: −40 mV).* ***(b)*** *Example traces of recordings from WT (black: normotonic, gray: hypotonic) and NKCC1$^{-/-}$ (purple: normotonic, violet: hypotonic) animal. Traces show responses at −140 and +60 mV voltage steps in both conditions.* ***(c)*** *Left: Average I-V curve responses from WT in normotonic (N = 11 cells, black with SEM) and in hypotonic (N = 8 cells, gray with SEM) condition. Right: Average I-V curves from NKCC1$^{-/-}$ in normotonic (N = 11 cells, purple with SEM) and in hypotonic (N = 8 cells, violet with SEM) condition.* ***(d)*** *Input resistance of WT versus KO cells in normotonic condition. (F) Input resistance of WT versus KO cells in hypotonic condition. Mann–Whitney, $p < 0.05$.* ***(e)*** *Resting membrane potential in normotonic condition of WT*

versus NKCC1 KO microglial cells measured in current-clamp mode (0 pA injected current). Boxes: interquartile range, whiskers: min–max, vertical bar: median.

We observed distinct differences between WT and NKCC1$^{-/-}$ microglia, as the I-V curves revealed that knockout microglia exhibited significantly higher input resistance compared to WT, particularly at more positive voltage levels under both normotonic and hypotonic conditions (Figure 15c). Specifically, as also indicated by the slope of the I-V curves between the -40 mV and 0 mV, we measured significantly higher input resistance in knockout microglia when compared to WT (Figure 13e, Mann–Whitney, $p < 0.05$). Despite these differences, the resting membrane potential did not show a statistically significant difference (Mann–Whitney, not significant). This suggested that while NKCC1 deletion affects ion regulation, it does not alter the resting membrane potential significantly. To further analyze the effects of NKCC1 deletion, we isolated the swelling-induced current component by subtracting the currents obtained under normotonic conditions from those recorded during the hypotonic response.

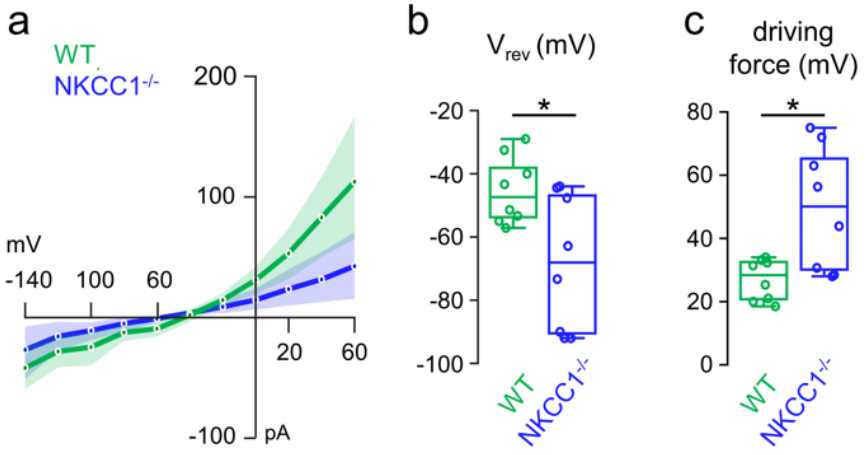

Figure 16: Absence of NKCC1 transporter leads to reduced intracellular Cl^- concentration. ***(a)*** *Calculated swelling-induced I-V curve responses (N_{WT} = 11 cells, N_{KO} = 8 cells, with SEM)* ***(b)*** *Input resistance of WT versus KO cells in normotonic condition. (F) Input resistance of WT versus KO cells in hypotonic condition. Mann–Whitney, $p < 0.05$.* ***(e)*** *Resting membrane potential in normotonic condition of WT versus NKCC1*

KO microglial cells measured in current-clamp mode (0 pA injected current). Boxes: interquartile range, whiskers: min–max, vertical bar: median.

The resulting I-V plot of the swelling-induced currents showed a more negative reversal potential in KO cells (Figure 16a, Mann–Whitney, $p < 0.05$). This finding indicated lower intracellular Cl^- concentration in knockout microglia. Finally, we calculated the driving force ($DF = V_{rest} - E_{swell}$) for each WT and knockout cell, which provided a more direct measure of ion regulation efficacy than ionic reversal potentials. Our results showed significantly higher DF values in knockout microglia compared to WT (Figure 16b, Mann–Whitney, $p < 0.05$). This supported the hypothesis that the absence of NKCC1 leads to reduced intracellular Cl^- concentration, affecting the cells' ability to regulate ions effectively.

4.3. Injury-induced ATP dynamics and microglial responses

4.3.1. Framework for investigating extracellular ATP dynamics in acute slice preparations

Our results showed that microglial cell body migration (Figure 2c), process extension towards the slice surface (Figure 3c) and gradual morphological transformation (Figure 9) were all markedly affected by P2Y12 signaling solely at baseline conditions. All these results were indicative of elevated purinergic signaling in acute slices after the preparation process. We aimed to understand the spatial and temporal patterns of extracellular ATP release and its implications for microglial function, so we made use of a genetically encoded fluorescent ATP sensor ($GRAB_{ATP}$), which allows for the dynamic monitoring of extracellular ATP with high temporal resolution[200].

First, we generated a novel mouse strain ($ATP1.0^{\Delta Vglut1}$) which expressed the $GRAB_{ATP}$ sensor in VGluT1 positive neurons. Slices were prepared from mice aged between P67–74 days, and we employed two-photon imaging to record 10-minute-long videos (256×128 μm image size, 0.5 frame/s rate, 920 nm excitation wavelength) capturing the fluorescent signal of a single image plane ~50 μm below the surface of acute slice preparations (Figure 17a). We were focusing on regions of the cortex (entorhinal,

temporal association, perirhinal) and hippocampus (CA 2-3 str. radiatum). Time-lapse imaging was followed by z-stack acquisitions from the same regions to also capture extracellular ATP gradients along the depth of slice preparations (Figure 17a). This process was repeated hourly after slice preparation to monitor changes over the 5-hours of incubation.

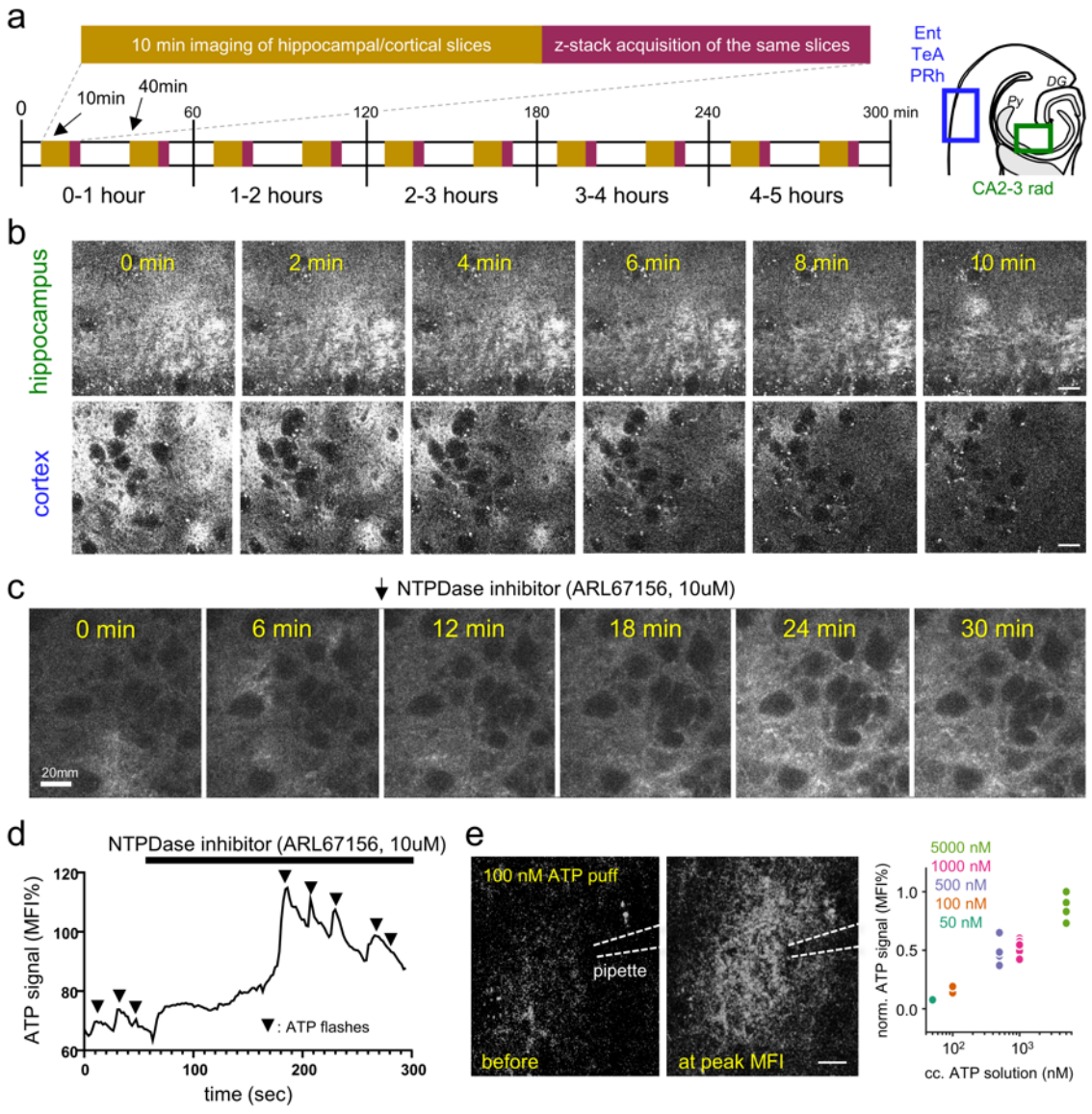

Figure 17: Framework for investigating extracellular ATP dynamics in acute slice preparations. (a) *Ex-vivo 2P imaging of the ATP sensor (GRAB$_{ATP}$) in VGluT1 neurons, followed by z-stack acquisition. (N = 3 animals, males, ~P70 days).* ***(b)*** *Representative images of the 10-minutes-long videos recorded immediately after cutting from regions of*

the hippocampus (green) and cortex (blue). Scale: 20 µm. ***(c)*** *Representative images taken from the time-lapse video showcasing the effect of NTPDase inhibitor (ARL67156, 10 µM), resulting in gradual increase of ATP signal. Note, that NTPDase blockade does not abolish focal ATP release events. Scale bar: 20 µm.* ***(d)*** *Graph representing the effect of NTPDase inhibitor (ARL67156, 10 µM), which resulted in gradual increase of ATP signal, while also preserving smaller peaks indicating focal ATP release events.* ***(e)*** *ATP sensor signal before and after a 100 nM ATP puff from a pipette within the acute slice tissue ~50 µm below the surface. ATP was diluted in standard ACSF (left). The measured normalized MFI% signal of ATP puffs elicited with different ATP concentration pipette solutions (right). Note that the ATP sensor signal scales linearly with ATP concentration. Scale bar: 5 µm.*

4.3.2. Passive efflux of ATP from injured cells form an increasing extracellular ATP gradient towards acute slice surfaces

The imaging experiments from the first slices revealed high fluorescent signal which rapidly decayed during the 10 minutes of recording. This result suggested elevated extracellular ATP levels in both the hippocampal CA3 region and cortical layers shortly after slice preparation (Figure 17b). We wanted to confirm that the rapid decrease in mean fluorescent intensity (MFI) was not the result of optical bleaching but reflected the activity of extracellular ecto-ATPase. To this end, we used the ecto-ATPase blocker ARL67156, while ATP dynamics were similarly monitored, but for a longer imaging period (Figure 17c). In this case, we used slices that were incubated for at least 4 hours, where we did not observe immediate, high fluorescent intensity and decreasing signal characteristics. At baseline conditions, the MFI signal was stable on a longer timescale and only displayed small peaks that were the result of small, focal ATP increase-events realized in a flash-like activity pattern (Figure 17d). Following NTPDase inhibition, the MFI signal rapidly increased, indicative of functional ecto-ATPase activity that can rapidly metabolize extracellular ATP which in turn manifests as a decrease in the MFI signal. Importantly, the observed ATP flashing activity as evidenced by the small peaks on the MFI signal persisted after NTPDase inhibition. We also wanted to calibrate the measured intensity of the signal by the direct application of solutions with given ATP

concentrations. To this end, we used standard recording pipettes filled with 10, 50, 100 nM or 0.5, 1, 5 µM ATP, diluted in standard ACSF. The pipettes were positioned within the tissue ~50 µm below the slice surface during time-lapse imaging sessions, while the ATP solution was delivered by the application of gentle puffs (Figure 17e, left). We observed immediate, ATP concentration-dependent focal increases in MFI signal, which showed a nice linear correlation between concentration and signal intensity. These results confirmed that - within our experimental setting - the dynamic changes in $GRAB_{ATP}$ fluorescent intensity reflected functional alterations of extracellular ATP levels in a linear fashion within the 50 nM - 5 µM range.

Our quantifications showed that the initially high fluorescent signal followed by gradual decrease (Figure 17b, 18b) was most prominent near the acute slice surface, as evidenced by our confocal z-stacks (Figure 18a). Importantly, these images indicated that the intensity gradient showing higher extracellular ATP levels near the surface was largely maintained throughout the total 5 hours of experimentation, with gradually decreasing overall intensity both in areas of the hippocampus and in the cortex (Figure 18c). Based on the characteristics of these signals, we hypothesized that this signal was a direct consequence of cutting-induced passive ATP outflow from injured cells, which resulted in higher extracellular concentration near the cutting surface due to a higher ratio of injured cells. Based on our NTPDase inhibition data (Figure 17c,d), we concluded that these signals were gradually decreasing as a direct consequence of the functional ecto-ATPase activity within the slices.

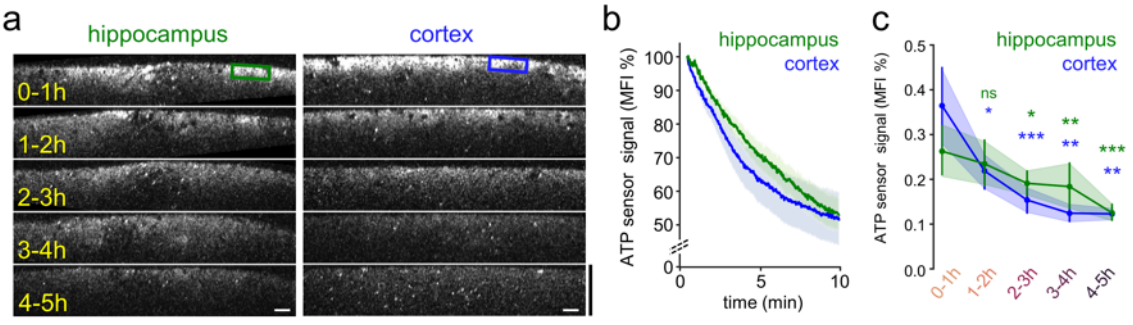

Figure 18: Slice cutting results in the passive efflux of ATP from injured cells with an increasing gradient towards cut surfaces. (a) *ATP sensor signal (MFI%) showing a continuous decrease of extracellular ATP levels from early slices (measured within the*

first hour after slice preparation). Two-way RM ANOVA, Time: F(1.169, 21.04) = 67.03, p < 0.0001. Regions: F(1, 18) = 0,3801, p = 0,5452, mean ± SEM. ***(b)*** *Side-views of confocal Z-stacks captured within each hour after slice preparation: elevated ATP levels at the slice surface (0–25 µm, left). Horizontal scale: 20 µm, vertical scale: 125 µm.* ***(c)*** *Quantification of (b), ATP levels show a time-dependent decrease (5-h vs. to 0-1 h). Two-way RM ANOVA, Tukey's multiple comparison, F(4,64) = 8.267, p < 0.0001, mean ± SEM (N = 3 animals, n = 3 slices, 4 ROIs/region).*

4.3.3. Slice cutting also induces endogenous, focal ATP release events

Interestingly, we found another type of extracellular ATP activity which comprised of intense, focal flashing events (Figure 19a), that were regularly observed in all slice preparations across different time-points. To characterize this flashing activity, we isolated the event-related peaks from the background MFI signal (Figure 19b). Our quantification showed that while ATP events similarly occurred both in regions of the hippocampus and the cortex (Figure 19b), both event intensity and incidence were higher in the cortex (Figure 19c). The average ATP event incidence was 12.3 ± 2.2 in the hippocampus and 25.4 ± 5.2 in the cortex during the 10-minute imaging periods, resembling systemic inflammation- or laser ablation-induced flashing activity in vivo[200]. These results indicated that slice cutting induces two different types of extracellular ATP dynamics: the passive outflow of ATP from injured cells maintaining a gradient towards the acute slice surface (Figure 18), accompanied by endogenous, focal ATP release events sustained for hours after slice preparation (Figure 19).

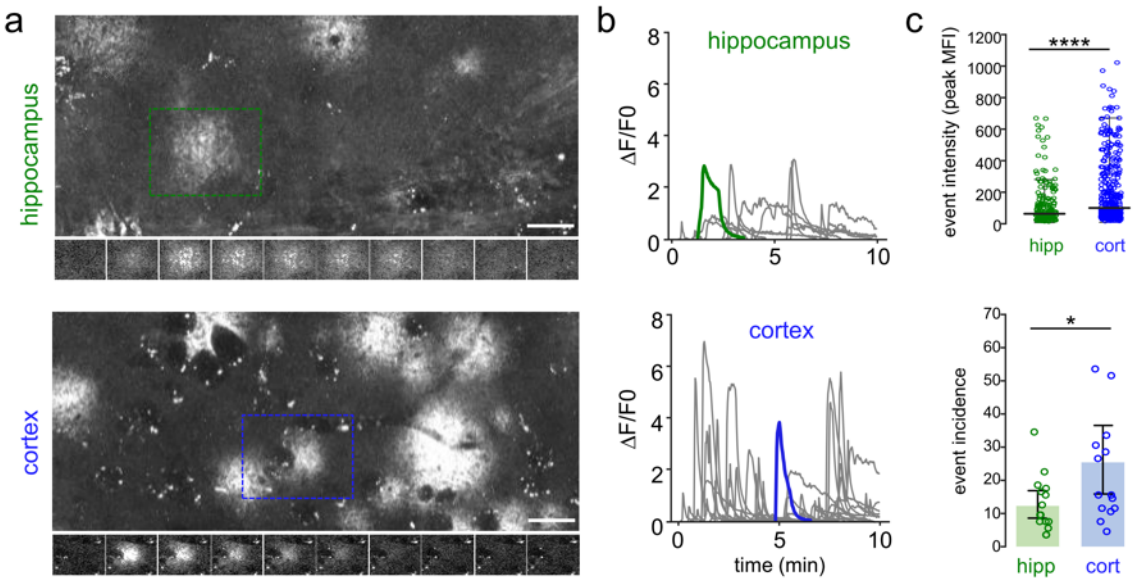

Figure 19: Slice cutting induces endogenous, focal ATP release events. ***(a)*** *Occurrence of ATP flashing activity in the hippocampus (green, top row) and in the cortex (blue, bottom row), timelines at the bottom show the evolution of two specific ATP events within the green/blue squares (10 s/image). Scale: 20 µm.* ***(b)*** *ΔF/F graphs showing focal ATP event peaks measured from hippocampus (green) and cortex (blue) that were isolated from the background.* ***(c)*** *Intensity/incidence values of focal ATP events in cortex (n = 360, green) vs. hippocampus (n = 181, blue). Incidence number represents ATP events/10-min imaging/slice. Mann–Whitney (two-sided), p < 0.0001, median ± SD (left); unpaired t-test (two-sided), p = 0.0258, mean ± SEM (right).*

4.3.4. Secondary-injury induced extracellular ATP dynamics mimic slice cutting-induced release events

We wanted to examine whether we could replicate the injury-related induction of elevated fluorescent signal by inflicting secondary injuries at later time-points during the incubation process. To test this, a secondary injury was inflicted manually using a sterile blade between 10 minutes-long imaging sessions. For these experiments, the ATP sensor was delivered via AAV injections to CX3CR1-cre/tdTomato mice or slices were prepared from the previously described ATP1.0$^{\Delta Vglut1}$ mice. The age of mice varied between P19-

20 and P69-99. Our results confirmed that at sites of secondary injuries the same sudden rise in extracellular ATP and consequent decay manifested (Figure 20a) as we observed in the case of early imaging of slices immediately after slice preparation (Figure 20a). The difference between injured and non-injured areas were most apparent when we compared the MFI signal from both regions and with areas recorded at baseline conditions (Figure 20b). The effect was observable even ~ 4 hours after slice preparation with immediate, intense ATP responses, which was prevalent in both older (P74 days) and late postnatal (P20 days) animals.

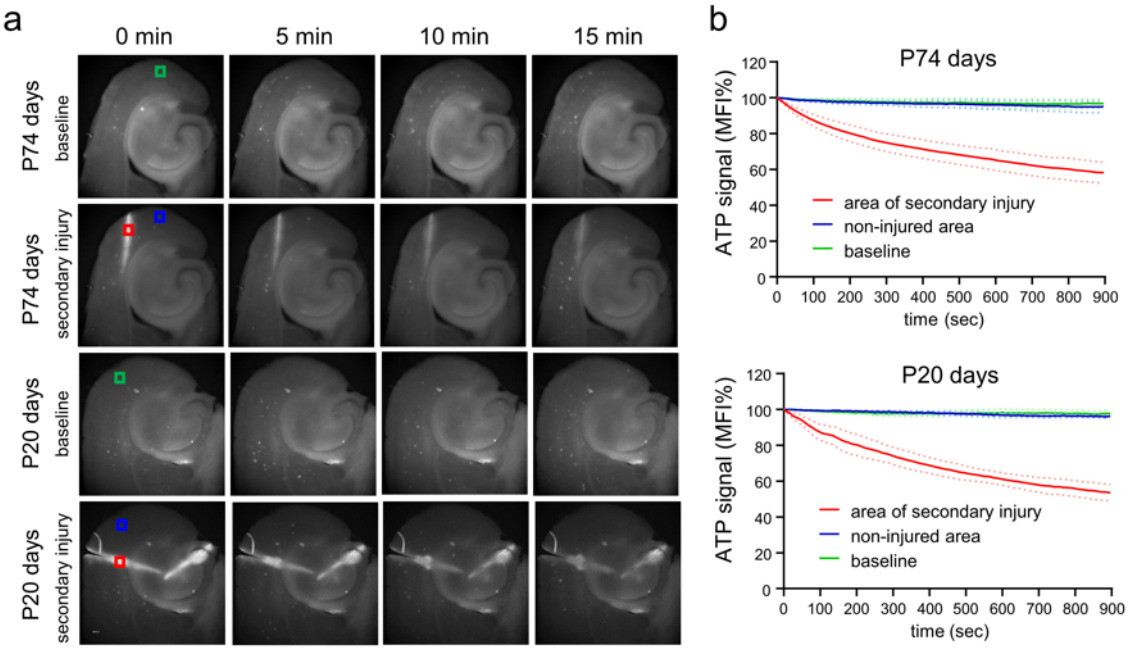

Figure 20: Secondary injury-induced extracellular ATP dynamics mimic slice cutting-induced release events. ***(a)*** *Secondary mechanical injuries resulting in immediate, intense ATP release (red) compared to non-injured sites (blue) or at baseline conditions (green) recorded ~4 hours after slice preparation.* ***(b)*** *Quantification of the difference in baseline fluorescent intensity and consequent decay, which develops similarly in slices from both P74 and P20 mice. N=5 animals, n=3 slices/animal. Two-way repeated measures ANOVA with Geisser-Greenhouse correction, **p<0.01 for secondary injury vs non injured areas and not significant for non-injured areas in injured vs non injured slices. Scale bar: 500 µm.*

4.3.5. Focal ATP events can be separated into two distinct clusters

Since our observations revealed a previously undescribed, focal type of ATP dynamics, we went on to characterize this phenomenon in more detail. Initially, we observed that the ATP event parameters (amplitude, duration, area) showed a log-normal distribution with a high degree of variance, suggesting different mechanisms or sources behind ATP release. To see whether these parameters might reflect distinct types of focal events, we went on to deploy K-means clustering analysis. This method revealed at least two separate groups in both regions of the hippocampus and in the cortex, differentiating a dimmer/faster/smaller (flash) and a significantly brighter/slower/bigger (surge) subset of events. By comparing the event parameters to events evoked by mechanical puffs of ATP from pipettes (Figure 21, black circles), flash intensities were usually around or below the 100 nM ATP concentration range, while surges were between the 100 nM–1 µM ATP range. Importantly, most of the ATP events did not exceed ~1 µM concentration, indicating effective degradation upon release.

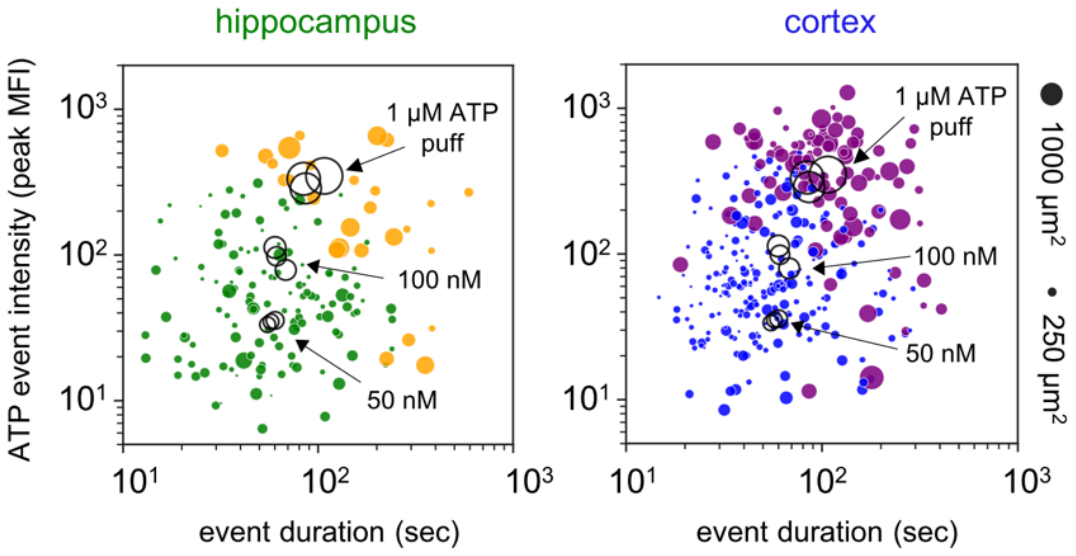

Figure 21: Focal ATP events can be separated into two distinct clusters. *K-means clustering reveals two different event clusters. The size of dots correspond to the size of flashes/surges (black indication) from the hippocampus (green/yellow) and the cortex (blue/purple). Black circles indicate ATP puffs with different concentrations.*

4.3.6. Distinct clusters of ATP events show evolving temporal dynamics

Further quantification of event parameters indicated that there is a significant separation in all measured parameters when comparing the two identified clusters of flashes with surges (Figure 22a) both in the case of hippocampal and cortical events. Our initial observations indicated that there might be a time-dependent evolution of the different event types, so we went on to investigate the time-course of clustered events. This analysis revealed that the prevalence of surges significantly increased between 1-2 hours of slice preparation (Figure 22b), while it gradually decreased towards the 5th hour of the recovery period, similarly in the hippocampus and the cortex.

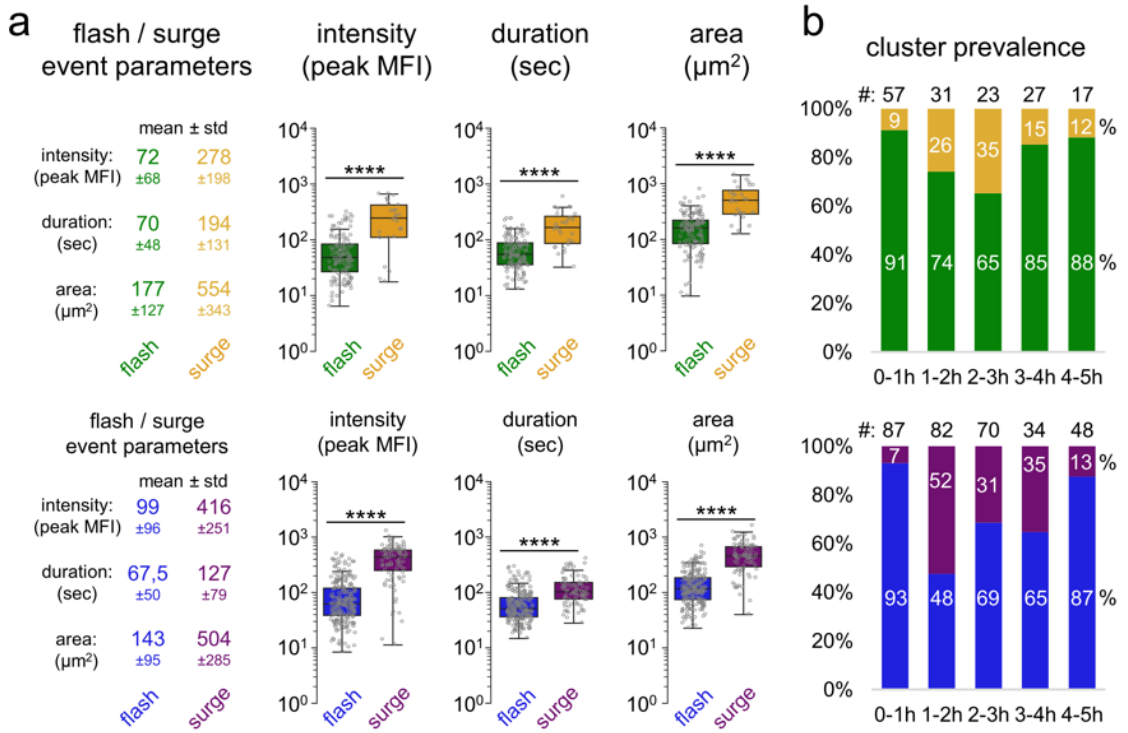

Figure 22: Focal ATP events form two distinct clusters with evolving temporal dynamics. ***(a)*** *ATP flash/surge characteristics show significant separation in all measured parameters (event intensity, duration, area), Mann–Whitney (two-sided), $p < 0.0001$ ($N = 3$ animals, $n = 10$ slices, 5–5 slices/timepoint). Boxes: interquartile range, whiskers: min–max, vertical bar: median.* ***(b)*** *Cluster prevalence changes over time after slice preparation. Note: substantial increase of ATP surge (yellow:*

hippocampus and purple: cortex) prevalence 1–2 h after slice preparation (N = 3 animals, n = 10 slices, 5–5 slices/timepoint).

4.3.7. ATP event characteristics are slightly modulated by microglial receptor antagonists

Direct, localized application from pipettes or passive ATP outflow from injured cells during laser ablations had been shown previously to attract microglial processes[90,91]. Importantly, both P2Y12R and CX3CR1 signaling pathways have been implicated to be critical during process movement and locomotor activity, as also indicated by our results concerning the migratory behavior towards the slice surface (Figure 2-3c). Since we observed robust endogenous flashing ATP activity, which was maintained for hours after slice preparation, we wanted to examine whether these focal ATP events could also influence microglia process locomotion and function in a P2Y12R/CX3CR1-dependent manner. To this end, we used viral injections (AAV9-hsyn-cATP1.0) to express the $GRAB_{ATP}$ sensor in cortical neurons of microglia reporter mice (CX3CR1-cre/tdTomato, P96-119). After 5-7 weeks of expression, we performed ex vivo two-photon imaging experiments similarly as described before (256 × 128 μm image size, 0.5 frame/s rate) but in this case we used 930 nm excitation wavelength and simultaneously imaged 3 planes that were 4 μm apart. This configuration enabled us to capture both microglia process movements and focal ATP events more effectively in a larger tissue volume. Time-lapse images were converted into maximum intensity projection (MIP) videos for analysis. Since we wanted to explore possible roles of P2Y12R and CX3CR1 signaling, we also performed recordings in the presence of their receptor antagonists PSB0739 and AZD8797, respectively.

K-means cluster analysis revealed the same separation of events to flash/surge cluster groups both at baseline conditions and in the presence of P2Y12R or CX3CR1 antagonists, with some alterations in parameter values (Figure 23a). Quantification revealed that ATP surges were more intense in slices subjected to CX3CR1 blockade compared to control and PSB conditions. On the other hand, the CX3CR1 blockade also resulted in shorter, while P2Y12R blockade in longer duration times of ATP surges compared to control (Figure 23b).

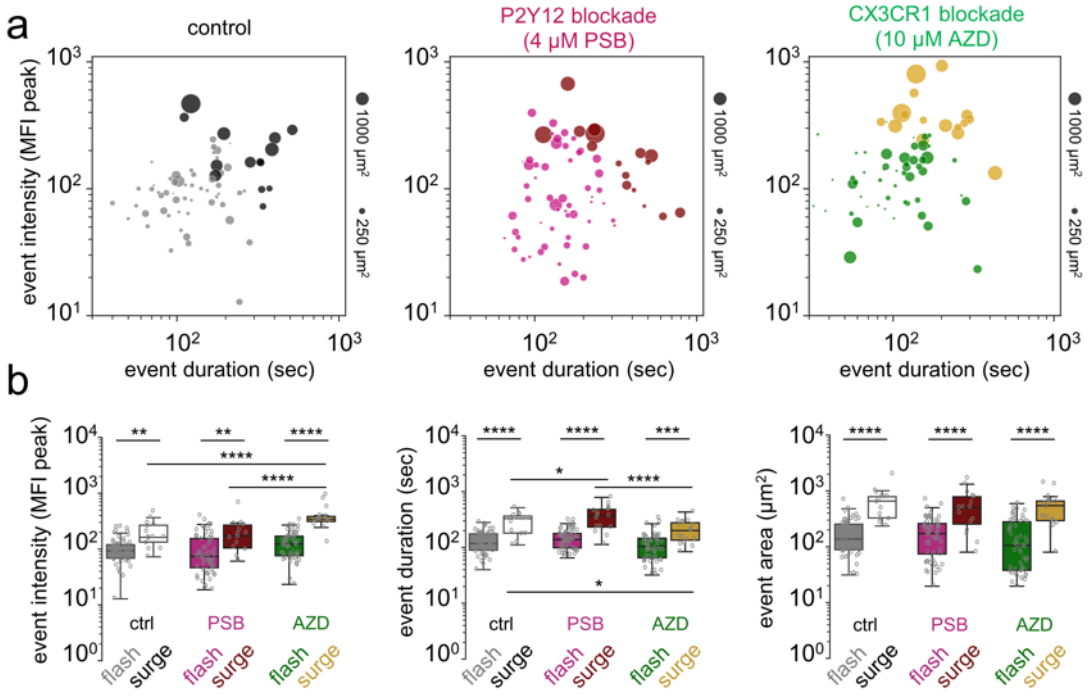

Figure 23: Focal ATP release event characteristics are slightly modulated by microglial receptor antagonists. ***(a)*** *K-means clustering analysis of event parameters in control/PSB/AZD conditions. Dot sizes represent the area of events (scale in right) Grey: control, pink: PSB, green: AZD show flashes, black: control; purple: PSB; yellow: AZD show surges (N = 9 animals, n = 6 ctrl, 8 PSB, 5 AZD treatment).* ***(b)*** *Comparison of ATP flash/surge characteristics of control, PSB and A treatment. Two-way ANOVA, Tukey's multiple comparisons, Intensity: F(1, 206) = 92.31, Duration: F(1, 206) = 133, Area: F(1, 206) = 115.8, p < 0.0001 (N = 9 animals, n = 6 ctrl, 8 PSB, 5 AZD-treated slices). Boxes: interquartile range, whiskers: min–max, vertical bar: mean.*

4.3.8. Framework for investigating microglial process recruitment by endogenous focal ATP events

Importantly, time-lapse recordings indicated that microglia processes might be rapidly (within 1–3 min) recruited to spontaneously emerging focal ATP events with a directed movement (dm) towards the center of flashes/surges (Figure 24a). To quantify process

locomotion induced by endogenous ATP dynamics, individual ATP events were extracted from MIP time-lapse videos to contain baseline (before peak), surge peak (maximum intensity of the event) and post event regions (Figure 24a-b). We identified the ROIs as the area occupied by the surge/flash event at maximum peak intensity. The corresponding changes of the fluorescent (cATPs, green) and microglia-related signals (tdTomato, red) were extracted in a baseline-corrected manner from these regions (Figure 24b, 25). The changes in the tdTomato signal corresponded to directed microglia process movements, which were quantified as the difference between baseline (100 s before the ATP event peak) and the first detected peak (Figure 24b, movement peak). When there were no detectable peaks within 300 s after the peak in cATPs signal, a 100 s region of the tdTomato signal following the cATPs signal peak was averaged and taken as a change value.

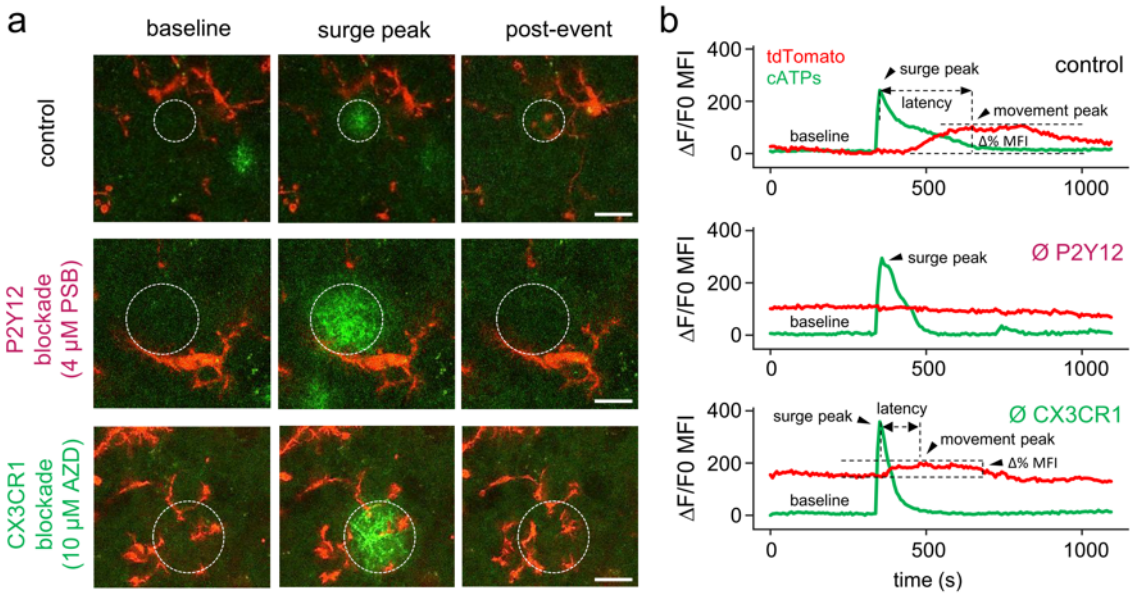

Figure 24: Quantification of microglia process recruitment by surge ATP events. (a) *Representative MIP images taken from videos recorded to capture ATP events (green) and consequent process displacement (red) in control conditions (black, top row) or in the presence of P2Y12R (purple, middle row) and CX3CR1 (green, bottom row) antagonists. White dotted circles demarcate ROIs indicating the ATP event area at maximum intensity (surge peak). Scale bars: 10 µm.* ***(b)*** *ΔF/F traces show the evolution of ATP surges in time (green) separated to three main phases: baseline, surge peak and*

post event, which were used for quantification. Superimposed ΔF/F signal shows the process accumulation (red) measured within the ATP surge territories (ROIs), as demarcated in a) with white dotted circles.

We also analyzed events within the flash cluster group in the same manner as in case of surges, and we found that these events were also readily recruiting microglial processes (Figure 25). Our initial observations indicated that process movements were impaired in the presence of P2Y12R and CX3CR1 antagonists, both in the case of surge/flash events (Figure 24-25).

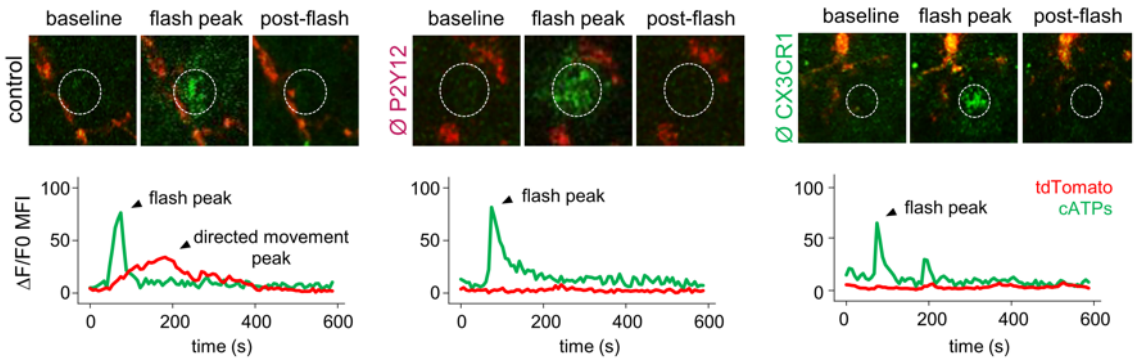

Figure 25: Flash ATP events recruit microglia processes similarly to surges. *Representative MIP images displaying ATP flash events (green) and consequent process displacement (red) in control conditions (black, left) or in the presence of P2Y12R (purple, middle) and CX3CR1 (green, right) antagonists. White dotted circles demarcate ROIs indicating the ATP event area at maximum intensity (flash peak). Scale bars: 5 µm. ΔF/F traces show the evolution of ATP flashes in time (green), and superimposed ΔF/F signal shows the process accumulation (red) measured within the ATP flash territories.*

Quantification showed that blockade of P2Y12R or CX3CR1 receptors largely prevented microglia process recruitment to flashes, while movements towards surges were less affected by AZD treatment (Figure 26a). Interestingly, no effect on movement speed was observed, indicating that P2Y12 and CX3CR1 blockade might specifically influence the initiation of directed process movements (Figure 26b). The majority of ATP events were

followed by direct movement, while blocking P2Y12 receptors reduced the prevalence of directed process movement significantly, and CX3CR1 receptor antagonists moderately (Figure 26c). In control slices, a significantly higher proportion of ATP events elicited directed movements at earlier time-points after slice preparation (44 events before, and 22 events after 3 hours of incubation), which difference was diminished in the presence of PSB (12 vs. 15) or AZD (26 vs. 26, Figure 26c). Microglia movement to ATP flashes was affected by both P2Y12R and AZD, whereas movements to ATP surge events were only affected by PSB (Figure 26d). Overall, our data indicated that directed microglial process recruitment to focal ATP events are mediated by P2Y12R and CX3CR1 signaling, contributing to microglial phenotype changes in acute brain slices.

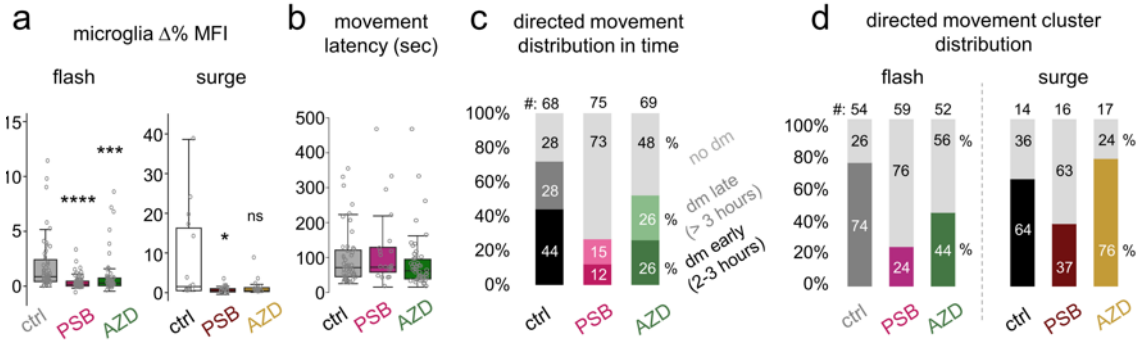

Figure 26: Focal ATP events dynamically recruit microglial processes in a P2Y12- and CX3CR1-dependent manner. ***(a)*** *Microglia process recruitment to flashes/surges represented as the difference in tdTomato signal (Δ%MFI) within flash/surge areas (ROIs).* ***(b)*** *Latencies of process movements (N = 9 animals, n = 6 ctrl, 8 PSB, 5 AZD-treated slice), measured as time elapsed between surge/flash peak and process movement peak (as described in Figure 22-23) Kruskal–Wallis-test with Dunn's multiple comparison test, Δ%MFI: $p < 0.0001$ (left), Latency: $p = 0.19$ (right). Boxes: interquartile range, whiskers: min–max, vertical bar: median.* ***(c)*** *Directed movements (dm - by both flash and surge events) recorded during early (2–3 h) vs. late (3–6 h) time-points after slice preparation. Numbers at the top (#: XX) correspond to number of events. (N = 9 animals, n = 6 ctrl, 8 PSB, 5 AZD treated slices).* ***(d)*** *Distribution of process movement prevalence in response to flashes / surges (9 animals, 6 ctrl, 8 PSB, 5 AZD treated slice). Numbers at the top (#: XX) correspond to number of events. The colors of dark grey (control), pink (PSB), green (AZD) represent the prevalence of microglial*

process movements towards flashes, the colors black (control), purple (PSB), yellow (AZD) represent movements towards surges (N = 9 animals, n = 6 ctrl, 8 PSB, 5 AZD-treated slices) Light grey areas represent events with no corresponding directed movement from microglia.

4.4. Injury-induced changes in P2Y12 expression and microglia-neuron interactions

4.4.1. Framework for quantifying time dependent P2Y12 receptor expression in acute slice preparations

Our results so far demonstrated important functional roles for P2Y12R in acute slice conditions, since it was implicated in microglia process polarization (Figure 3), morphological transformation (Figure 9) and in directed motility towards ATP-release events (Figure 26). Importantly, previous studies have shown that P2Y12 signaling also plays a pivotal role in sensing and influencing neuronal activity and fate[89], while it can undergo significant downregulation upon injury or inflammatory challenges[201]. Since our observations in acute slice preparations indicated robust injury-related actions that were effectively modulating microglia phenotype, we wanted to quantitatively examine whether changes in P2Y12R expression occur in line with these mechanisms during the incubation process.

To this end, we created acute slice time-series from CX3CR1$^{+/GFP}$ animals, and preparations were immersion-fixed at different timepoints during incubation as described previously, but this time we only investigated regions of the cortex (Figure 27a). For the quantitative visualization of P2Y12R we employed a post-embedding immunofluorescent labelling technique (Figure 27b), allowing for unbiased assessment of labelling intensity changes[202]. The technique described by Holderith et al.[202] was slightly modified for this study. In brief, fixed slices were washed in phosphate buffers (PB), treated with 1% uranyl-acetate, dehydrated in ascending alcohol series, and finally embedded in resin blocks (Figure 27b-1). Each block contained all slices from a respective time series of one animal. Ultrathin sections were cut at 200 nm thickness, ensuring each section contained the full width of all acute brain slices (Figure 27b-2). Thereafter, sections were encircled with silicon polymer to retain incubating solutions on glass slides, resin-etched,

and primary/secondary antibodies were applied in the blocking solution at room temperature (Figure 27b-3). Following further washes, slides were rinsed in distilled water, sections were mounted, coverslipped and finally went through confocal imaging while ensuring that measurements along the whole depth (except for the top and bottom 40 µm region) of acute slices can be performed (Figure 27b-4). Quantitative analysis of images was performed by at least two observers, who were blinded to the origin of the samples and the experiments.

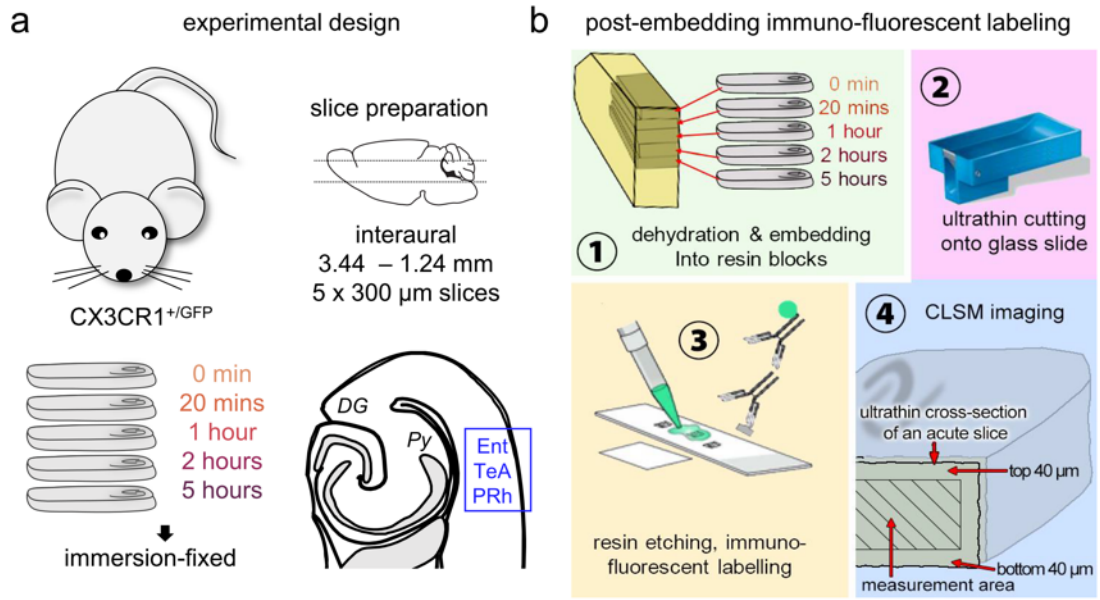

Figure 27: Framework for quantifying time dependent P2Y12 receptor expression in acute slice preparations. ***(a)*** *CX3CR1$^{+/GFP}$ littermates (N = 3 animals, only males, P35 days) were used to create acute slice time-series. Measurements were performed within Ent/TeA/PRh cortical areas.* ***(b)*** *After fixation, slices were dehydrated and embedded into resin blocks (1), ultrathin slices were cut onto glass slides (2), and resin etching was followed by post-embedding P2Y12R immunofluorescent labelling (3). Finally, z-stack images were gathered from preparations via high-resolution CLSM (4). Each ultrathin section represented the whole cross-section of one acute slice (4), measurements were done throughout the whole depth range of acute slices within a single image plane.* ***(c)*** *P2Y12R labelling via the post-embedding technique. Microglial cell bodies (left), thick*

processes (middle), thin processes (right) and P2Y12R labelling (top) or P2Y12R labelling only (bottom). Scale: 2 µm.

4.4.2. P2Y12 receptors are rapidly downregulated in acute slices, most prominently at thick and thin microglial processes

In line with the robust extracellular purinergic activity evidenced immediately after acute slice preparation, we observed a consistent, rapid decrease in P2Y12R labelling intensity during the incubation process (Figure 28a). Most prominent changes were already prevalent after 1 hour of incubation, followed by a slight increase towards the 5-hour timepoint (Figure 28b). The loss of P2Y12R was most pronounced in thick and thin processes, with decreases of 25% (after 20 minutes) and 29% (after 1 hour), respectively, and a 20% decrease (after 1 hour) in microglial cell bodies.

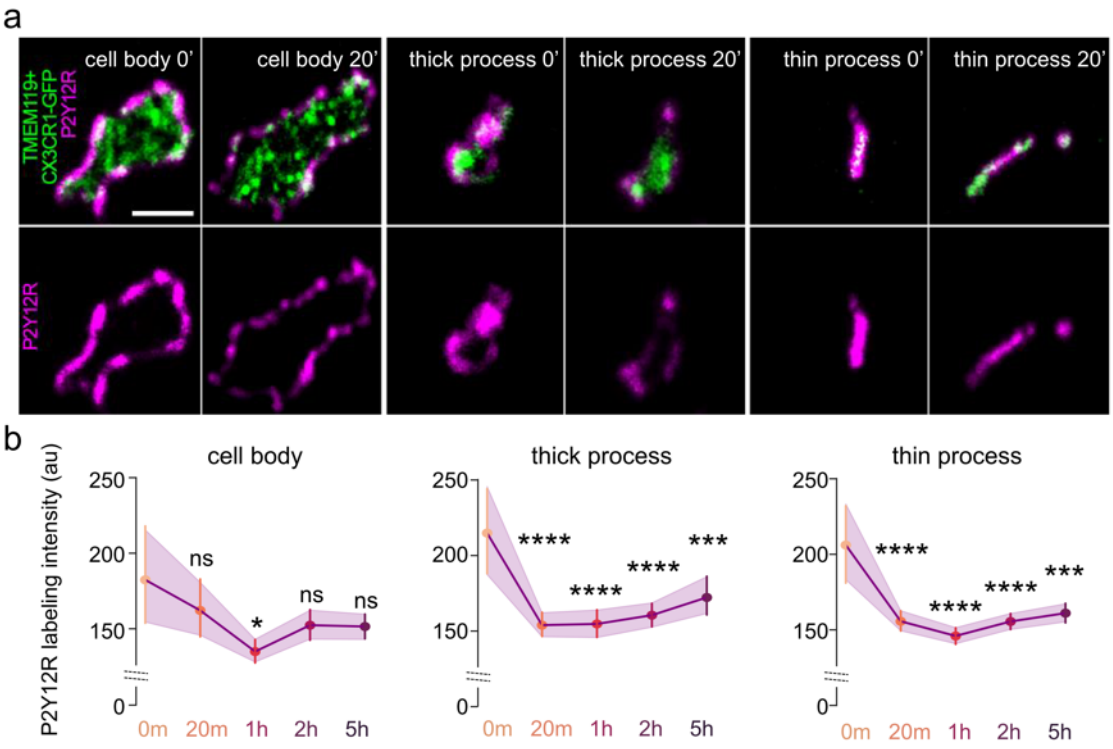

Figure 28: Rapid downregulation of P2Y12 receptors is most prominent on thick and thin processes. (a) *P2Y12R labelling using the post-embedding labeling technique. Microglial cell bodies (left), thick processes (middle), thin processes (right) and P2Y12R*

labelling (top) or P2Y12R labelling only (bottom). Scale: 2 µm (N = 3 animal, n = 3 slices/animal). ***(b)*** *Quantification of P2Y12R labelling intensity at microglia cell body (left), thick processes (middle) and thin processes (right.) N = 3 animal, P35 days; n = 3 slices/animal; One-way ANOVA, Dunnet's multiple comparisons, Body: F(4, 40) = 2.746, p = 0.04 (left), Thick: F(4, 62) = 9.698, p < 0.0001 (middle), Thin: F(4, 154) = 13.09, p < 0.0001 (right), mean ± SEM. Comparisons are made to 0 min values.*

4.4.3. Gradual decrease in soma contact prevalence is preceded by rapid initial increase in somatic area coverage

Since P2Y12R-signalling is crucial for the formation of somatic junctions which represent main interaction sites between microglial processes and neuronal soma[89], we wanted to investigate whether the prevalence of these contacts or the area covered on neuronal cell bodies by microglial processes was affected by the downregulation of P2Y12R. To this end, we used the classical pre-embedding approach on acute slice time-series prepared from CX3CR1$^{+/GFP}$ littermates and enhanced the GFP-signal of microglia to locate process endings, while we used Kv2.1 labelling to identify neuronal cell bodies (Figure 29a). Neuronal somata were considered to receive a contact when there was no space between neuronal soma and microglial process labeling on at least a 0.5 µm long co-localized segment. The area of process coverage was measured with a step size of 300 nm on single-channel images, while Kv2.1-positive cells were randomly selected between those which were fully included in the captured volume. The surface was calculated by measuring the circumference of the soma on every section and multiplied by the thickness of the section. The surface of microglial process contacts was measured in a similar manner.

Our analysis revealed a gradual decrease in the percentage of neuronal soma contacted by microglial processes, dropping by ~23% after 5 hours of incubation (Figure 29b). Initially, microglial process coverage doubled immediately after cutting, indicating rapid microglial actions, but decreased back to control values after 5 hours (Figure 29c).

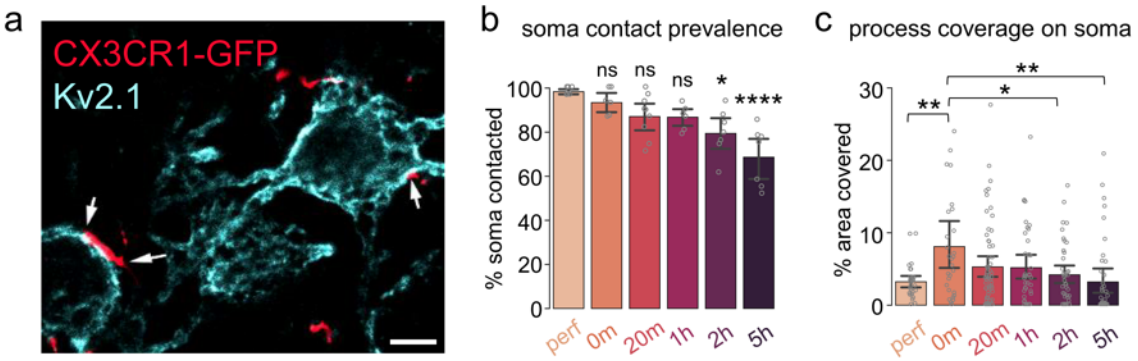

Figure 29: Gradual decrease in soma contact prevalence is preceded by rapid initial increase in somatic area coverage. (a) *Representative section of MIP image created from z-stacks used to quantify microglial contact prevalence/process coverage on neuronal soma. White arrows: areas where microglial processes form putative contacts on neuronal soma (overlap of microglia and Kv2.1 labelling, Scale: 5 µm). CX3CR1$^{+/GFP}$ littermates (only males, P65 days).* ***(b)*** *Quantification of contact prevalence (left) and somatic coverage of neurons (right) by microglial processes (N = 3 animals, n = 7–9 regions of interest analyzed/timepoint, 30-60 neurons/timepoint P65 days). One-way ANOVA, Dunn's multiple comparisons, F(5,36) = 9.118, p < 0.0001 (left), F(5,235) = 3.409, p = 0.0054 (right), mean ± SEM.*

4.4.4. 3-dimensonal dipartite model reveals that microglia morphology significantly influences somatic junction prevalence

While these results confirmed a robust downregulation of P2Y12R in thick and thin microglial processes during the incubation period, sufficient receptor expression seemed to have persisted in order to maintain functional P2Y12R-signalling and somatic junctions. Furthermore, the initial, rapid increase of somatic area covered by microglia processes seemed to be a counter-active mechanism in response to tissue disturbance. Importantly, the rapid downregulation and subsequent plateau of P2Y12R expression on thick and thin processes (Figure 28b) seemed to follow a different pattern in time when compared to the gradual loss of somatic junctions (Figure 29b). On the other hand, gradual morphological changes (Figure 8) seemed to align well with changes in contact prevalence (Figure 29b). We were interested in whether the observed decrease in process

numbers and length during morphological transformation could have manifested in the observed decrease in somatic junction prevalence. To answer this question, we employed a 3-dimensional bipartite model of neurons and microglia, which was supported by basic anatomical and morphological parameters taken from our datasets and from the literature[203] (Figure 30a,b). In brief, the model was designed to generate a bipartite graph with a fixed number of neurons (200) and microglia (30) randomly positioned within an area without overlapping, so that the density of neurons was 90000 / mm^3. Neurons had 15 μm and microglia had 10 μm sized cell bodies (in diameter). Microglia were randomly, but evenly distributed within the area, where microglial cell bodies were not allowed to be closer than 30 μm. Upon contact generation, each microglia had a maximum reach set as a parameter (30 and 20 μm in our case), and if a given neuron was within reach, a contact was established (Figure 30, b, c). The graph was randomly generated 100 times and contact distributions of neurons and microglia was calculated as mean ± SEM across the different simulations (Figure 30c,d).

The model showed that microglia with a maximum reach of 30 μm were sufficient in covering the whole neuronal population with only ~2% of neurons left without somatic contacts at a given time (Figure 30c). Importantly, the model also indicated that the majority of microglia had been connected to 10 neuronal partners on average, which results were consistent with our anatomical observations (unpublished data) measured at baseline conditions (Figure 30a, c, e). When we decreased the maximum reach of individual microglia to 20 μm, we observed a significant increase in the number of uncontacted neurons (~20%), while both of these changes were also in line with our measurements regarding morphological transformation (process length *in vivo*: 29.34 ± 1.09 μm vs. 5 hours after slice preparation: 18.29 ± 14.18 μm) and decrease in somatic junction prevalence after 5 hours spent in incubation (Figure 30b, d, f). Ultimately, these results demonstrated that the model could effectively reproduce key anatomical features of microglia-neuron somatic contacts, while also suggesting that the measured decrease in somatic contact prevalence is likely to arise due to differences in microglial morphology between the 0-minutes and 5-hour timepoints.

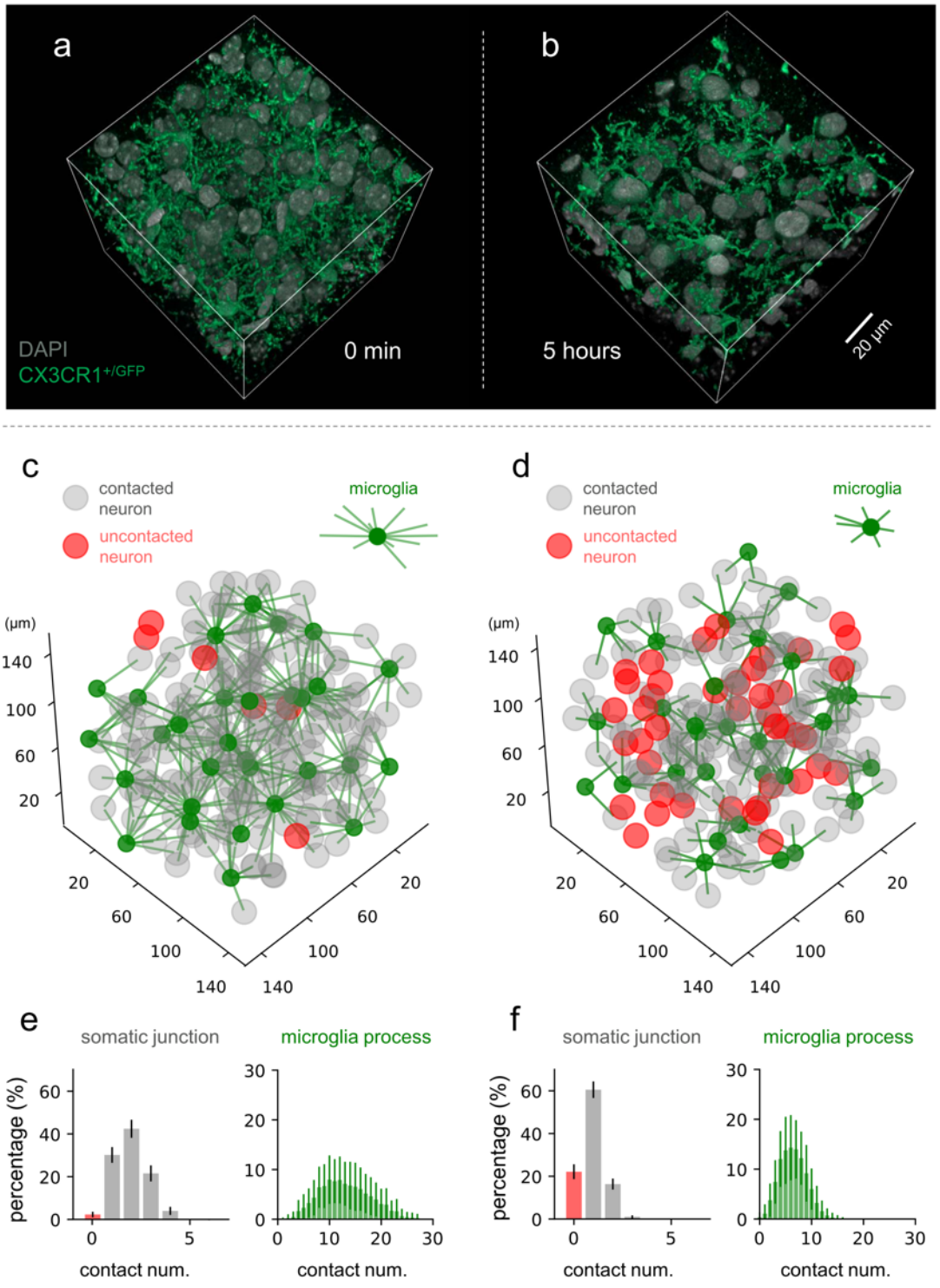

Figure 30: Constraints in microglia morphological features significantly decreases somatic junction prevalence. (a) *3-dimensional reconstruction of an acute slice preparation showing neurons (DAPI, grey) and microglia (CX3CR1$^{+/GFP}$, green) immediately (0 min) after slice preparation.* ***(b)*** *Same as in (a), but the slice were fixed 5*

hours after preparation. ***(c)*** *Representative instance of a randomly generated bipartite graph of neurons (n= 200, grey) and microglia (n= 30, green) with anatomically relevant features. Maximum reach for individual microglial processes is 30 µm. Neurons left without somatic junctions are colored to red. On the top right corner, a representative instance of a randomly selected microglia from the graph is shown with its processes.* ***(d)*** *Similar as in a) with maximum reach for microglial processes set to 20 µm.* ***(e)*** *Bar graphs displaying percentages of neurons (left, grey) and microglia (right, green) with given number of somatic junctions/microglia processes, respectively. Format: mean ± SEM. Values are averaged across a 100 randomly generated graph with maximum reach set to 30 µm. Bar representing percentage of neurons with 0 somatic connections is colored red.* ***(f)*** *Similar as in c) with maximum reach for microglial processes set to 20 µm.*

4.4.5. Microglia-synapse interactions are altered after slice preparation

Acute slice preparations have been extensively used in the past to examine mechanisms behind synaptic plasticity, such as long-term or short-term potentiation/depression (LTP/D or STP/D). Conversely, it also has been demonstrated that the density of synaptic elements can rapidly increase after acute slice preparation in the form of synaptic sprouting[190–192], while underlying mechanisms have not yet been revealed. Importantly, microglial cells are long recognized as pivotal regulators of synaptic elements, both during development and in the adult CNS[87,110,112]. Since we observed dramatic changes in case of somatic contacts, we also wanted to explore whether interactions with synaptic elements are altered after the insult of slice preparation. To investigate the role of microglial influence on both glutamatergic and GABAergic synapses, we employed the previously described post-embedding approach to label synaptic elements and microglial processes in acute brain slices (Figure 27). Synapses were identified via the co-localization of pre- and postsynaptic markers VGLUT1 (vesicular glutamate transporter 1) and Homer1 in case of glutamatergic, while VGAT (vesicular GABA transporter) and Gephyrin were used for GABAergic synapses (Figure 31a, 32a, 33c). Double staining techniques were employed to ensure specificity and sensitivity, validated by the sufficient match between pre- and postsynaptic markers. Regions of interest (ROIs) were randomly

selected within the neuropil, deliberately avoiding cell bodies to focus on synaptic regions.

First, we looked at microglial contacts with distinct synaptic elements (Figure 31a). Interestingly, we observed rapid alterations in microglial contact prevalence with glutamatergic synapses, where contact numbers increased by 46% immediately after slicing, then gradually returned to baseline (Figure 31b, left). This response closely mimicked the behavior we saw in case of somatic area coverage (Figure 29c). In contrast, GABAergic synapses showed a 33% decrease with microglial contacts within 20 minutes, further dropping to 47% after 5 hours (Figure 31b, right).

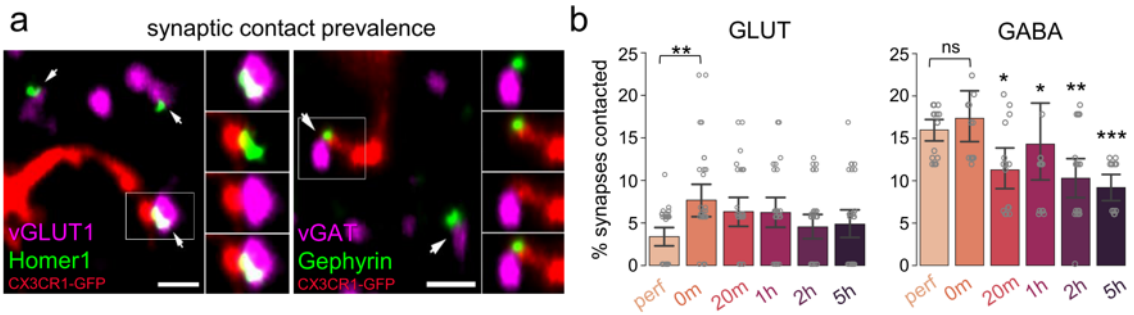

Figure 31: Microglia-synapse interactions are altered after slice preparation. (a) *Single image planes from confocal z-stacks used for the quantification of synaptic contact prevalence by microglial processes on glutamatergic (left) or GABAergic (right) synapses. (Insets show channel pairs from boxes, pre- and postsynaptic marker, microglia and postsynaptic marker, microglia, and presynaptic marker, merged.) White arrows indicate individual synapses contacted by processes (bars: 1 µm). CX3CR1$^{+/GFP}$ littermates were used (only males, P65 days).* ***(b)*** *Bar plots show microglial contact prevalence onto glutamatergic (left) or GABAergic (right) synapses (N = 3 animals, n = 15–18 ROI analyzed / timepoint, P65 days) Kruskal–Wallis, Dunn's multiple comparisons, p = 0.019 (left), p < 0.0001 (right), mean ± SEM (compared to 0 min).*

4.4.6. Microglia are key modulators of synaptic sprouting in acute slice preparations

Next, we used the quantitative post-embedding labeling (Figure 32a) to examine whether the commonly observed synaptic sprouting is also observable in our acute slices. Indeed, analysis showed that both glutamatergic and GABAergic synaptic densities increased over time. Glutamatergic synapses showed a 20% increase already after 1 hour, and peaked at a 28% increase after 5 hours, while GABAergic synapses peaked at 20% increase after 2 hours (Figure 32b).

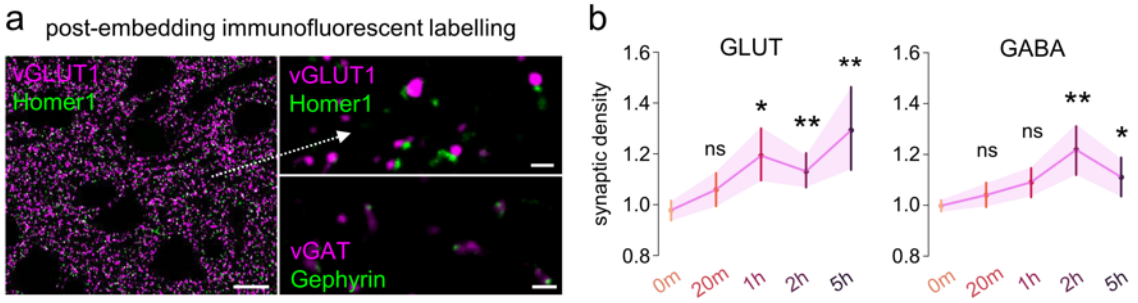

Figure 32: Synaptic sprouting occurs in acute slice preparations at baseline conditions. ***(a)*** *MIP images of confocal z-stacks used for the quantification of glutamatergic and GABAergic synaptic densities, created by using the post-embedding technique. Glutamatergic labeling by the co-localization of vGLUT1 (purple) and Homer1 (green, left, bar: 5 µm) zoomed-in inset show glutamatergic labeling (right, top; bar: 1 µm). The inset at the bottom show GABAergic labeling by the co-localization of vGAT (purple) and Gephyrin (green, right, bar: 1 µm) labelling.* ***(b)*** *Synaptic density changes of glutamatergic (left) and GABAergic (right) synapses at given time-points after acute slice preparation (N = 6 animal, n = 6 regions analyzed / slice / timepoint, P65 days); Kruskal–Wallis, Dunn's multiple comparisons, p = 0.0024, mean ± SEM (compared to 0 min).*

In order to assess the role of microglia during synaptic sprouting, synaptic densities were measured similarly in slices prepared from control mice or mice treated with PLX5622, a CSF1R inhibitor known to eliminate microglia in vivo (Figure 33a). This treatment was

administered for three weeks prior to slice preparation, which led to the successful depletion of microglia from the CNS (Figure 33b). Previous studies have shown that depletion of microglia with PLX3373 or PLX5622 does not substantially alter neuronal cell numbers or morphology, nor does it cause cognitive or behavioral deficits, although a slight increase in dendritic spine numbers has been observed[204–206]. Surprisingly, the expected increase in glutamatergic synaptic density was abolished during the absence of microglia, resulting in a 27% lower density compared to controls after 5 hours (Figure 33d, left). GABAergic synapses initially increased in density, peaking at 1 hour, but then significantly decreased by 2 hours (Figure 33d, right). These results highlighted the role of microglia in regulating synaptic dynamics in acute brain slices. Importantly, microglia appeared to facilitate glutamatergic while repressing GABAergic synapse formation in the early stages (under 1 hour) following acute slicing. These findings underscored the critical role of microglia in influencing the neuronal network through microglia-neuron interactions, even within acute brain slices following tissue injury.

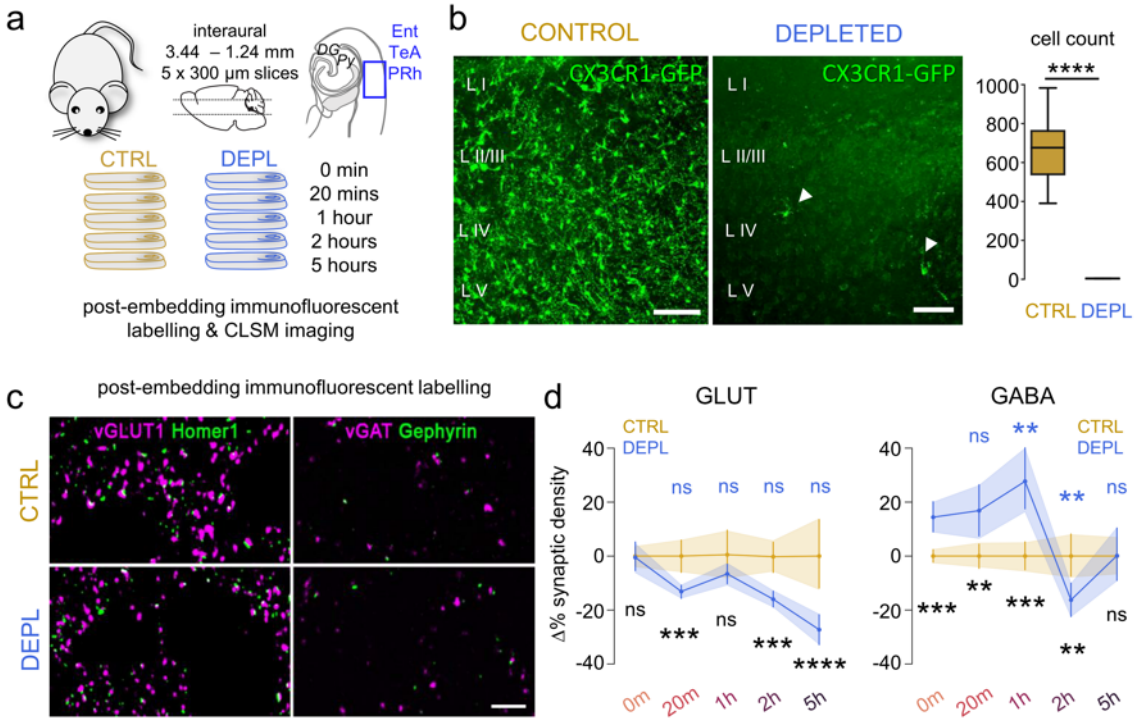

Figure 33: Microglia are key modulators of synaptic sprouting in acute slice preparations. (a) *CX3CR1$^{+/GFP}$ littermates (only males) were used to create control (CTRL; N = 3, P65 days; brown) and microglia depleted (DEPL; N = 3, P65 days; blue)*

subgroups. Slice preparations were obtained from both groups and immersion-fixed at different timepoints. ***(b)*** *MIP images taken from control (left) or depleted (middle) slices (scale: 100 µm). White arrows show a few remaining identified microglia within the depleted slices. Left: Quantification comparing the total number of microglial cells in control (brown) vs. depleted (blue) slices (N = 6 animal/condition, P65 days); Mann–Whitney (two-sided), p < 0.0001, median ± SD. Boxes: interquartile range, whiskers: min–max, vertical bar: median.* ***(c)*** *MIP images created from confocal z-stacks used to compare densities of glutamatergic (left) or GABAergic (right) synapses in control (top) or depleted (bottom) slices (bar: 5 µm).* ***(d)*** *Comparison of glutamatergic(left) or GABAergic(right) density changes during incubation. Averages of control (brown) vs. depleted condition (blue). (N = 6 animal / condition, n = 6 regions analyzed / slice / timepoint, P65 days); Two-way RM ANOVA, Tukey's multiple comparisons, F(4,184) = 4.668, p = 0.0013 (left), F(4,184) = 19.08, p < 0.0001 (right), mean ± SEM.*

4.5. Microglial influence on network synchrony

4.5.1. Network synchrony emerges in parallel with synaptic sprouting in acute slice preparations

Previously we observed that microglia are actively increasing somatic coverage on neuronal soma immediately after slice preparation (Figure 29c), as well as their presence at glutamatergic connections (Figure 31b), which ultimately influenced synaptic sprouting (Figure 33d). Importantly, microglia can exhibit a dual role within the CNS, as in certain conditions microglia fulfill neuroprotective roles through synaptic maintenance and promoting tissue repair by the secretion of cytokines. However, microglia can also release neurotoxic substances and pro-inflammatory cytokines which can exacerbate neuronal damage[144,145,207]. We wanted to examine whether alterations in microglia function observed after acute slice preparations are supportive in nature and could positively influence network activity. The sharp wave-ripple (SWR) complex is a widely studied synchronous activity originating in the CA3 region of the hippocampus, associated with essential cognitive processes such as memory formation, consolidation, and planning[208]. Importantly, our slice preparation method was initially developed to investigate the mechanisms behind SWR generation, since within these slice preparations

SWR activity spontaneously emerges within the CA3 region after sufficient time spent in recovery within the incubation chamber[187–189,209].

We utilized our slice preparation technique to investigate whether observed changes in microglia-neuron interactions are contributing to the recovery of neuronal synchrony and facilitate the emergence of SWRs. First, we created thick (~450 μm) acute slice preparations from CX3CR1$^{+/GFP}$ mice which were hourly transferred into a recording chamber while preserving the original orientation (the surface of acute slices within the incubation chamber remained at the top within the recording chamber), where electrodes within pipettes filled with artificial cerebrospinal fluid (ACSF) were placed into the CA3 region of the hippocampus to perform local field potential (LFP) recordings (Figure 34a). The pipettes were positioned at a depth of ~80–100 μm below slice surface, ensuring accurate measurement of neuronal activity. The dual flow recording chamber[188] allowed ACSF to flow both above and below the slices at a rate of 3–3.5 ml/min per channel, maintaining a temperature of 33–34 °C. This setup ensured optimal conditions for neuronal activity to emerge. From the LFP recordings SWRs were detected above a threshold of 2 times the standard deviation (SD) of the signal (Figure 34b). From these recordings we analyzed various SWR features, including peak amplitude, SWR rate and ripple amplitude (Figure 34c). Initially, our recordings confirmed that SWR events with stable amplitude and frequency parameters only emerged after 2 hours spent in the incubation chamber (Figure 34b,c), which aligned with the time-point when glutamatergic and GABAergic synaptic densities peaked during synaptic sprouting (Figure 32b). These results suggested that microglia mediated synaptic sprouting might have contributed to the recovery of neural synchrony.

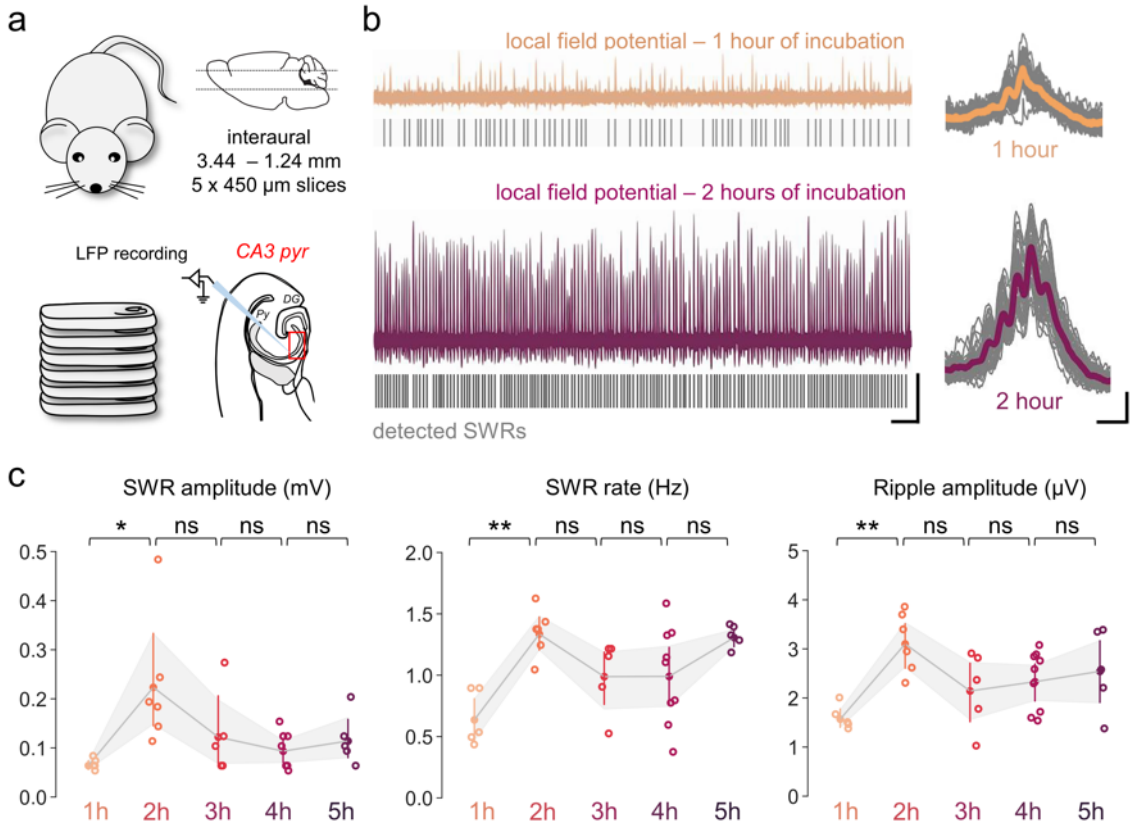

Figure 34: SWR emerges after synaptic sprouting in acute slice preparations. (a) *Schematic representation of experiment. CX3CR1$^{+/GFP}$ littermates (N=8; P65 days) were used to create acute hippocampal slice preparations and placed into an interface-type incubation chamber. Subsequently, slices were transferred hourly into a recording chamber to measure sharp-wave ripple (SWR) activity via local field potential recordings (LFP) registered from the CA3 pyramidal layer of the hippocampus.* ***(b)*** *Representative LFP recordings (left) measured after 1 (yellow) or 2 hours (purple) spent in incubation. Grey lines represent detected SWR events. Bars: 10 s, 50 µV. Representative averaged traces of detected SWRs (right, N=#50 in total) measured after 1 hour (yellow: average, grey: individual events) or 2 hours (purple: average, grey: individual events) of incubation. Bars: 100 ms, 25 µV.* ***(c)*** *Quantification of SWR amplitude (left), rate (right) and Ripple amplitude (right) comparing events measured after different time spent in the incubation chamber before recording. N=8 animals, P65 days; One-way ANOVA with Tukey's multiple comparison test, p<0.05 (left), p<0.01 (middle), p<0.05 (right).*

4.5.2. Microglia contribute to the emergence of network synchrony in acute slice preparations

To test microglial influence on the emergence of SWR activity, we devised a similar experiment where we went on to systematically compare the emergence and observed features of SWR activity in acute slice preparations harvested from control or loss of microglial function animals. To this end, acute slice preparations were similarly obtained from control (CX3CR1$^{+/GFP}$ littermates), microglia depleted (CX3CR1$^{+/GFP}$ littermates, PLX3397 was used for depletion, see: Figure 33b), P2Y12R knockout (P2Y12R$^{-/-}$) or CX3CR1 knockout animals (CX3CR1$^{-/-}$). Knockout mice had control mice (C57Bl/6J mice) as a comparison from the same age group (~65 days old). Each recording day six slices from control or loss of function animals were prepared in pairs, which were also measured in a pairwise manner to ensure consistency (Figure 35a). This included simultaneous slice harvest, incubation and measurement of slices, while the same solutions and equipment were used throughout each experimental day. The position of slices within the recording chamber was also alternated in order to minimize artefacts that might arise from the experimental configuration.

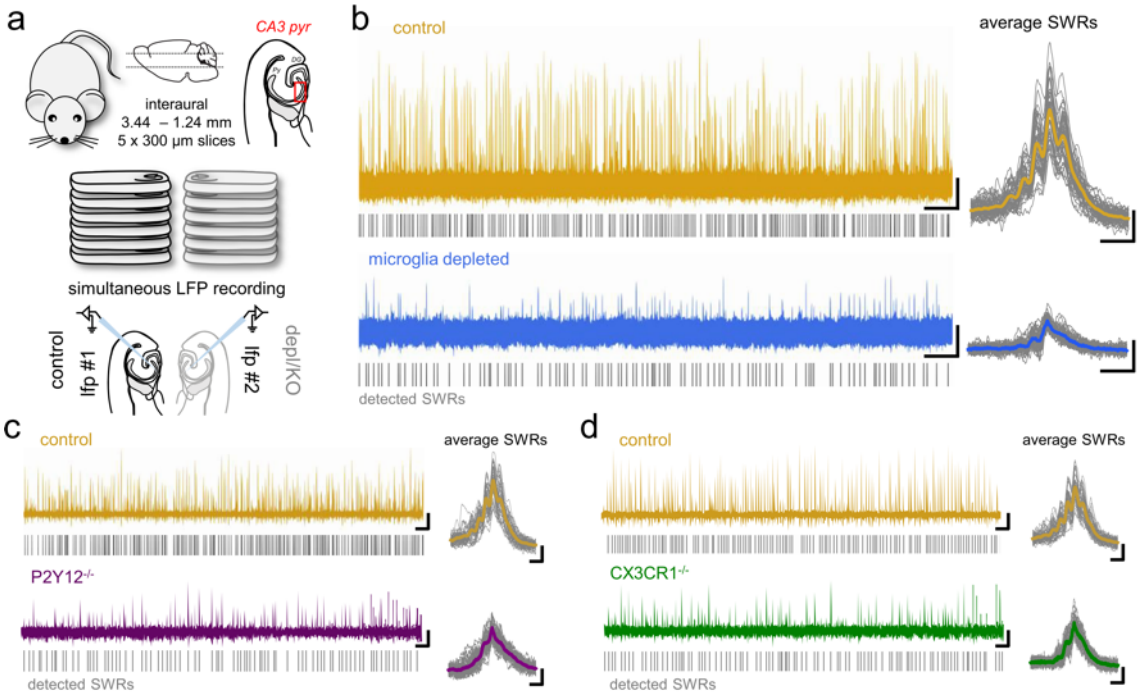

Figure 35: Framework for investigating the emergence of SWR activity in control and loss of microglia function acute slices. ***(a)*** *Schematic representation of experiment. Acute hippocampal slices were obtained from control or loss of function groups and slices were measured in a pairwise manner. SWR activity was recorded from CA3 pyr. Depletion: CX3CR1$^{+/GFP}$ littermates (only males) were subjected to 3 weeks of either control/ PLX3397 diet (CTRL; N = 6, P65; gold, DEPL; N = 6, P65; blue) Knockouts: C57Bl/6J (N = 5 and N = 6) vs. P2Y12KO (N = 5) or CX3C1KO (N = 6), P65 days).* ***(b)*** *Representative LFP recordings (left; bar: 30 s, 50 µV), average SWR events (right, N = 50, Scale: 100 ms, 25 µV) from control (top, gold) and depleted (bottom, blue) slices. Grey lines: individual SWR events.* ***(c)*** *Same as in b), control (top, gold) and P2Y12RKO (bottom, purple) slices.* ***(d)*** *Same as in b), control (top, gold) and CX3CR1KO (bottom, green) slices.*

In order to track the emergence of SWR activity, each pair of slices were recorded for 30 minutes, and if no detectable SWR event was present during the recording, the slice was considered unable to generate SWR activity. We went on to quantify the emergence of SWR activity within these conditions (Figure 36). Our results indicated that microglia-depleted acute slice preparations were significantly less sufficient in generating detectable SWR activity (control: 50% vs. depleted: 11%), while loss of P2Y12R had a minor effect (control: 46.6% vs. P2Y12^{KO}: 33.3%), and CX3CR1 function did not influence the prevalence of SWR in acute slices (control: 52.8% vs. CX3CR1^{KO}: 52.8%).

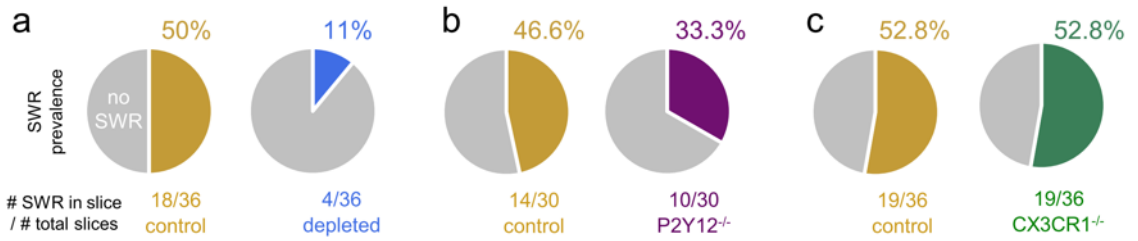

Figure 36: Spontaneous emergence of SWR activity is impaired in depleted and P2Y12R knockout slices. ***(a)*** *Pie-charts represent SWR activity occurrence in control (gold), and depleted (blue) acute slice preparations.* ***(b)*** *Same as in a) but controls are*

compared to P2Y12KO (purple). ***(c)*** *Same as in a) but controls are compared to CX3CR1KO slices (green). The grey area represents no spontaneous SWR activity (N = 6 ctrl vs. 6 depl animal, N = 5 ctrl vs. 5 P2Y12KO animal, N = 5 ctrl vs. 5 CX3CR1KO animal, 5 slices/animal, P65 days).*

We went on to analyze the characteristics of the recorded SWR events in order to reveal further differences that might have been the consequence of microglia function loss. Importantly, our results showed significant alterations within the parameters of spontaneously occurring SWR parameters (Figure 37). We observed that the amplitude of SWRs were significantly impaired in microglia depleted slices (ctrl vs. depleted: ~4,6-fold $p < 0.0001$; ctrl vs. $P2Y12^{-/-}$: ~ 1.7-fold, $p < 0.05$; ctrl vs. $CX2CR1^{-/-}$: ~ 1,5-fold, $p < 0.05$). We only observed significant difference in SWR rate when comparing control with depleted slices (ctrl vs. depleted: ~1.6-fold, $p < 0.05$), while the amplitude of ripple frequency was significantly impaired in all comparisons (ctrl vs. depleted: ~2.1-fold, $p < 0.001$; ctrl vs. $P2Y12^{-/-}$: ~1.3-fold, $p < 0.001$; ctrl vs. $CX2CR1^{-/-}$: ~ 1.2-fold, $p < 0.001$; Mann-Whitney test). Taken together, these results suggest that the positive influence of microglia on SWR activity observed in acute slice preparations is in part mediated by microglial P2Y12R- and CX3CR1-signalling, and that microglial actions were pivotal for the maturation of ex vivo acute slices.

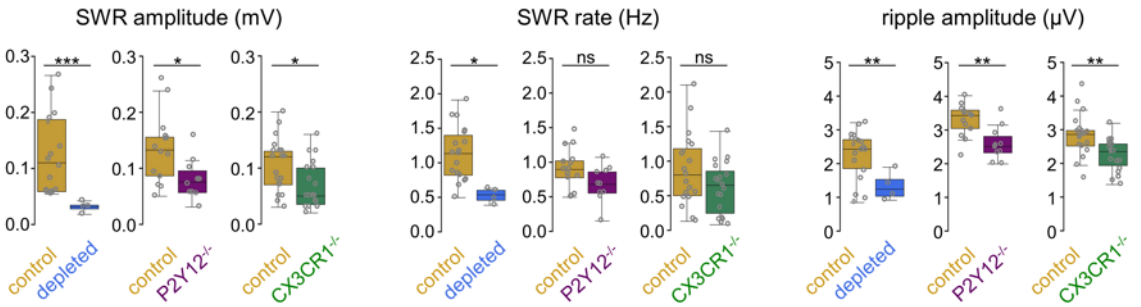

Figure 37: The absence of microglia, microglial P2Y12 or CX3CR1 dysregulates sharp-wave ripple activity*. Quantification of SWR amplitude (left), rate (middle) and Ripple amplitude (right) from control (gold), depleted (blue), P2Y12 KO (purple), and CX3CR1 KO (green) slices. (N = 6 ctrl vs. 6 depleted animal, N = 5 ctrl vs. 5 P2Y12 KO, N = 5 ctrl*

vs. 5 CX3CR1 KO animal, 5 slices / animal, P65 days); Mann–Whitney (two-sided), $p < 0.001$. (Each group had its own controls from littermates.) Boxes: interquartile range, whiskers: min-max, vertical bar: median.

Importantly, the observed phenotypic changes of microglia paired with their influence on somatic and synaptic elements ultimately resulted in more resilient SWR activity, also highlighting the pivotal role of microglia in facilitating recovery after injury imposed by the slice preparation process. Taken together, these results underscored the neuroprotective nature of microglia in modulating neuronal viability, activity and network synchrony.

5. Discussion

Acute brain slices represent a well-established experimental approach that has been instrumental in studying the CNS from the scale of individual synapses to complex neuronal networks. Studies utilizing this technique have yielded seminal discoveries concerning all the different constituents of the CNS including neurons and glial cells collectively. Importantly, an increasing number of studies emphasize that cellular components of the CNS are highly interconnected and depend on each other for proper functioning, creating a need for more synergistic experimental approaches and holistic thinking in the future. Since microglia has been shown to be particularly sensitive to environmental cues while they interact dynamically with all other cell types[19,25,119,136], they are ideally positioned for investigating mechanistic roles behind these interactions. We deliberately utilized this feature as we systematically tracked alterations of acute slice microglial functions and their influence on neuronal networks during an experimentally relevant timeframe, using various sample sets from multiple laboratories. Furthermore, we employed advanced experimental techniques including a highly sensitive fluorescent ATP sensor to reveal previously undocumented features of injury-related mechanisms taking place after slice preparation. We show that while injury induces marked phenotypic changes in microglia, they preserve protective roles to maintain viability and spontaneous activity of neuronal networks in a P2Y12R- and CX3CR1-dependent manner. We believe that mechanisms revealed here have important implications beyond acute slice experimentation or studies centered around microglia, while it could definitely facilitate improvements in ex vivo methodologies. Finally, findings on injury-related microglial actions may also have important implications for common neurological disorders.

5.1. Injury-induced cell body and process migration

First, we studied how injured areas within acute slice preparations influenced microglial cell body motility and process polarization at baseline levels, without any additional stimulus presented after slice harvesting. While locomotor and process polarization behavior have been previously observed in acute slices, these investigations all employed additional application of ATP or tissue insult via laser ablations[128,183]. Importantly, active migration of microglia within the brain parenchyma is a characteristic response to

neuronal injury and inflammation *in vivo*, widely studied with the same experimental approaches[90,91]. To the best of our knowledge, here we presented the first population-level description of baseline cell body and process distribution changes along the full depth of slices, investigated in an experimentally relevant timeframe for most ex vivo studies (0 to 5 hours after slicing). Migration and chemotactic responses have been shown to be governed by extracellular ATP which acts as a guiding signal for microglia via purinergic receptor activation, particularly through P2Y12 receptors[200,210,211]. Our results are in line with these observations, while we demonstrate that microglia sense and gradually reorganize their cell body and processes along the extracellular ATP gradient in a P2Y12- and CX3CR-dependent manner, facilitating targeted migration towards areas of neuronal injury, and possibly initiating neuroprotective responses[212]. It has to be noted here, that oxygenation levels along the depth of the slice, as well as higher neuronal activity at the top surface could also manifest as a gradient signal[213–215] which might affect microglia distribution. Importantly, the ability of microglia to traverse across the neuropil could be critical in case of acute slices, considering the high volume of damaged tissue that needs to be maintained near the cut surfaces. The repositioning of microglial cell bodies is probably essential for recapitulating a homeostatic environment across the injured parenchyma, as it is well-documented that activated microglia display a facilitated phagocytic capacity necessary for clearing cellular debris[206]. This might be particularly important, given that early recognition and effective clearance of non-viable cells are known to be critical factors during aging and in neurodegenerative disorders[99,126,211]. The deployment of activated microglia into the injured areas is also likely to mitigate neuronal excitotoxicity and promote recovery via the release of trophic molecules like TGF-β1 where it is most needed[212,216], making this phenomenon an essential constituent of microglial neuroprotection. While the pivotal role of ATP as a signaling molecule in mediating these mechanisms is already well established, our results demonstrate that the CX3CL1-CX3CR1 signaling pathway also seems to be critical, implicated mostly in cell body migration towards injured sites. Indeed, the CX3C family of chemokines has been proposed as a candidate for neuronal rescue signal, as healthy neurons highly express fractalkine repressing microglial activation, while downregulation of fractalkine in injured neurons can allow microglial activation to occur[76,78].

5.2. Structural changes and morphological transformation

Our findings indicated that morphological transformation of microglia represented a generic response to injury after acute slice preparation, since comparable changes were seen in younger (P35 day) and older (P95 day) mice, and even at earlier stages during postnatal development (P18–20). We also demonstrated that different slice preparation techniques carried out by independent laboratories did not influence the gradually increasing density of reactive microglia morphology along the whole depth of acute slices. When comparing these results with studies that investigated other types of pathological conditions, microglia 1 hour after slice preparation showed similar morphological characteristics to what was observed at peri-infarct cortical areas and in experimental stroke models[184,217–219] using the same automated morphology analysis tool. Moreover, a ~50% drop in the number of process endings represented a similar difference to what microglia showed in tissue samples from control vs. Alzheimer's disease patients[220]. Importantly, this difference already occurred as early as 20 minutes spent within the incubation chamber. Taken together, these results further support the notion that the observed morphological alterations represent functional adaptations of microglia during the transitioning from homeostatic to pathological conditions, allowing an adequate response to changing environmental demands. In such conditions, activated states characterized by retracted processes allow for more effective migratory behavior to injured sites, while they also seem to be critical in enhancing the phagocytic capacity and ability to clear cellular debris[211]. Importantly, these morphological adaptations were demonstrated to be triggered by extracellular ATP, which is readily released upon injury[200]. When released, ATP serves as a reliable signal contributing directly to structural changes, while the transformation could also be modulated by various pro-inflammatory mediators like IL-1β and TNF-α[221]. Thus, the observed morphological plasticity of microglia seem to be pivotal in combating injury-induced alterations and subsequently promote tissue recovery.

5.3. Electrophysiological correlates of phenotypic transition

To date, electrophysiological data from in vivo microglia have not been published, meaning that such correlates of an undisturbed, physiological state is not yet available.

The vast majority of electrophysiological investigations focusing on microglia have been conducted in isolated cell-cultures or in acute and organotypic slices[170,171]. Microglia within isolated cell cultures typically display an activated state characterized by amoeboid morphology, which correlates with a unique pattern of inwardly and outwardly rectifying K^+ currents paralleled by decreased input resistance[171]. Importantly, acute and organotypic slices have been shown to preserve a microglial phenotype that is closer to the resting state when compared to isolated single-cell cultures. This was also reflected in their electrophysiological signatures, as within brain slices the inwardly/outwardly rectifying currents only appeared as a consequence of additional injury-related insults like facial-nerve cut, ischemic insult or induced status epilepticus before slice preparation[170]. These results demonstrated that microglia are capable of radically transforming their electrophysiological identity during phenotypic transformation, since acute slice microglia compared to cultures were shown to display higher input resistance, slightly depolarized resting membrane potential (between -40 and -20 mV) and lack of voltage-gated K^+ currents during baseline conditions. Importantly, the resting membrane potential of microglia has been shown to correlate with morphology in acute slices, suggesting that the activity of THIK-1 K^+ channels are mainly responsible for stabilizing the membrane potential and morphology within the ramified state, while locally increasing extracellular K^+ concentration can decrease ramification[102,222]. It has been proposed that transitioning into a more reactive phenotype might reflect a decreased expression of THIK-1, as activation via LPS treatment can result in significantly downregulated THIK-1 mRNA paired with more ameboid morphology[102]. Importantly, our results supported the idea that membrane depolarization, rapid P2Y12R downregulation and transition of microglia into a reactive morphology are co-occurring features of microglia in acute slices, confirming that THIK-1 is probably continuously downregulated after tissue disturbance. Since THIK-1 has been postulated to be less important in shaping microglial function during injury or inflammation, this necessitated the exploration of other candidates influencing microglia membrane properties. Our results indicated that NKCC1 channels are ideally placed to shape the electrophysiological identity of microglia both at resting state and upon tissue disturbance, by directly influencing microglial membrane properties and Cl^- ion regulation during these conditions. Importantly, it has also been demonstrated that NKCC1 is involved in shaping microglia morphology and primed inflammatory state[223].

5.4. Extracellular coding of injury-related signals

We used a newly developed, highly sensitive ATP sensor expressed by glutamatergic neurons within the hippocampus and the cortex to monitor extracellular ATP dynamics. It is well documented that extracellular ATP, and its derivatives can markedly influence microglial responses through NTPDase and P2Y12R mediated actions[90,224–227]. Importantly, we demonstrated in line with others that acute brain tissue damage results in elevated extracellular ATP levels[228–231], while the microglial process recruitment to spontaneously emerging focal ATP events in acute slice preparations have never been described before. As expected, our results indicated elevated ATP-levels close to the slice surfaces, and the manifestation of ATP gradients were likely the main driving force behind the observed microglial dislocation and prevalent morphological transitioning occurring throughout the slices. Additionally, our observations reinforced general guidelines established by others during electrophysiological investigations, which states to avoid measurements taking place within the top 50 μm of slice preparations[172]. We show that this region does not only include a higher density of dead cells, but extreme levels of extracellular ATP sustained for hours after slice preparation paired with a gradually increasing density of activated microglia intruding into the area. We demonstrated the existence of a unique form of endogenous, sustained purinergic activity manifested deep within the tissue, consisting of several minutes long focal ATP release events between the nanomolar to micromolar range, sustained for hours after slice cutting. Since the acute slice model is widely used in developmental brain research, we also performed these experiments on slices from early postnatal mice (~P19-20). Interestingly, we observed the very same mechanisms as in adulthood with regard to all of our observations. The immediate ATP release induced by injury, subsequent decay of ATP levels and flashing ATP events were all observed on a similar time- and intensity-scale in slices from a wide (P19–P119) age range. Based on event characteristics, flashing ATP activity is likely to represent a form of endogenous, spatiotemporal injury-encoding mechanism mainly driven by astrocytic activity, which was recently described in vivo[239,240]. While the astrocytic origin of these events have been confirmed by these studies, we observed ATP events near several neuronal cell bodies, supporting the notion

of ATP release from neuronal source. Importantly, these events were also recruiting microglial processes towards the occupied area. Based on the high variance of ATP event characteristics that separated them into distinct clusters of flashes and surges, it is possible that such signals can manifest simultaneously with distinct cellular origins. Due to the lack of appropriate tools to selectively block ATP release from different sources, the precise origin of endogenous ATP events within acute slices are yet to be confirmed by future studies. Extracellular ATP is known to be influenced by NTPDase and Ecto-5'-nucleotidase enzymes, which metabolize ATP to ADP, AMP and adenosine, respectively[225,232]. Upon ecto-ATPase blockade we observed the rapid elevation of extracellular ATP levels which maintained, or in some cases even enhanced the occurrence of these ATP events, possibly via ATP induced ATP release. Importantly, we observed regional differences in ATP event characteristics, which could either be the result of non-homogeneous sensor expression or may also reflect differences in responsiveness to injury within distinct brain regions.

5.5. Influence of endogenous ATP events on microglia and neurons

We observed that microglia responded readily to focal ATP events by P2Y12R-dependent fast process movements. Importantly, P2Y12 receptors represent a core marker for microglia in the healthy brain[69,233,234], while downregulation of P2Y12R is generally associated with reactive phenotypes and microglial dysfunction both in vivo and in ex vivo conditions[89,235–238]. We demonstrated with a fully quantitative post-embedding method[202] that rapid downregulation of P2Y12R occurs extensively at thick and thin processes of microglia already after 1 hour spent in incubation. Importantly, this rapid and sustained decrease was paralleled by the prolonged responsiveness of microglia processes to focal ATP events within the investigated time window (0–5 hours) and possibly beyond, indicating a close connection between the two phenomenon. Interestingly, resting-state microglia within the healthy brain is often described to have highly motile processes constantly surveying the brain parenchyma, which behavior was posited to not involve P2Y12R signaling but depend on THIK-1 activity[102]. Conversely, several studies utilizing acute brain and retinal preparations posited that ramified morphology and baseline motility is preserved ex vivo[177–182]. Our results strongly indicate

that baseline motility of microglia processes in acute slices represent a distinct behavior when compared to the surveying state observed in vivo, as it is generally guided by endogenous ATP events through P2Y12R signaling. Importantly, despite the observed P2Y12R downregulation in ex vivo conditions microglia seem to retain their ability to extend their processes towards the extracellular presence of ATP irrespective of it being endogenously released, directly applied or passively released by laser-induced tissue ablation. It is important to note that purinergic signaling has also been postulated to regulate neuronal activity via extracellularly produced or glia-derived adenosine[239,240] which can contribute to A1R mediated feedback suppression[239,241]. Specifically, ATP had been shown to trigger the recruitment of microglia processes in vivo, which resulted in the conversion of ATP to AMP by the microglial hydrolyzing ectoenzyme CD39, which is converted to adenosine by CD73 also expressed by microglia and other cells[14]. Based on these, it is an interesting possibility that the observed injury-induced ATP events followed by process recruitment might represent an elevated form of microglia-mediated negative feedback mechanism which operates in order to protect the neuronal network from excessive activation. In addition to purinergic signaling, we demonstrated that the blockade of CX3CR1 receptors also impaired microglia process recruitment towards ATP flashes. The main function of the neuronal CX3CL1 is posited to provide an inhibiting effect that is keeping microglia phenotypes within the quiescent, surveilling mode[78]. Interestingly, microglia-neuron fractalkine interactions have been shown to inhibit NMDA-mediated Ca^{2+} influx and neuronal apoptosis, further supporting the neuroprotective nature of microglia within these conditions[242]. Taken together, these observations strengthened the notion that microglia are key players in encoding and transducing signals related to neuronal injury. Following insult, the rapid release of ATP serves as a beacon that orchestrates microglial responses to cellular distress in a P2Y12 and CX3CR1-dependent manner, which induces neuroprotective behavior essential for maintaining homeostatic neuronal activity.

5.6. Alterations of microglia-neuron interactions

Collectively, our results concerning phenotypic states of microglia demonstrated marked alterations in cell body and process distribution, morphology, P2Y12R expression,

parallelled by injury-induced extracellular ATP dynamics affecting process movements. Importantly, these observations were all expected to influence microglia–neuron interactions, particularly through P2Y12R signaling, known to be important for microglial interactions with neuronal somata under various conditions[89,112,184,237]. Indeed, our data indicated that while the prevalence of somatic junctions slowly and gradually decreased, the percentage of somatic area covered by microglial processes showed a more than two-fold increase immediately after slice preparation, similar to what is observed in vivo after acute ischemia[89]. Our 3D modeling of microglia-neuron somatic junctions revealed that resting-state microglia morphology and density within the cortex is optimal for covering the whole neuronal population. However, changes in morphology, particularly a shorter maximum reach of processes, can in itself cause an increased number of uncontacted neurons, similar to what we measured directly after 5 hours of incubation. These results indicate that microglia maintains as many somatic junctions as physically possible, despite the robust, injury-induced structural and morphological transformation limiting its reach, which highlights the importance of these interaction sites. This was paralleled by a similar, rapid increase of contact prevalence at glutamatergic synapses, while contacts on GABAergic synapses were gradually decreasing. Several previous studies have demonstrated that synaptic sprouting is a characteristic feature of acute slice preparations[190–192], but the underlying mechanisms have not yet been revealed. Microglia are well-known regulators of synaptic elements in various conditions throughout development and aging[108,116,243–245], as they are capable of secreting cytokines and growth factors, which can promote synaptic plasticity and facilitate the formation of new synaptic connections in response to neuronal injury. To this end, we investigated whether acute slice microglia might also contribute to synaptic density changes. Indeed, we found that the absence of microglia profoundly impaired synaptic sprouting. Of note, elevated GABAergic synaptic density in microglia-depleted mice observed immediately after cutting could be explained by effects not related to injury, as the lack of microglia has been shown to elevate GABAergic synapse density in vivo[246]. While microglial contacts can directly facilitate spine formation of functional synapses[108,243,245,247], the rapid microglia-mediated effects in ex vivo brain slices were surprising. Nonetheless, their observed capacity to influence synaptic sprouting to this extent immediately after injury might involve both the removal of unwanted or damaged

synapses and the facilitation of new synaptic connections. One possible mechanism could be the release of brain-derived neurotrophic factor (BDNF) from activated microglia, which had been shown to promote synaptic growth and neurorepair[248]. Importantly, revealing more about microglial actions on sprouting within this context could be fundamental for the development of therapeutic strategies concerning neurodegenerative diseases[249]. Thus, further studies will be required to understand the molecular mechanisms underlying these effects.

5.7. Microglia-dependent modulation of network synchrony

Finally, our results demonstrated that the observed microglia-related mechanisms actively influenced the emergence of SWR activity in hippocampal acute slice preparations, largely mediated by purinergic, and moderately by fractalkine mechanisms. These results indicated that the presence of microglia and P2Y12R/CX3CR1 signaling is essential for the recovery of physiological-like network activity in ex vivo slices. These results indicated that in other conditions related to tissue disturbance, interventions aimed to inhibit these microglial actions could also render the neuronal network less capable of producing healthy activity patterns. In line with our observations, previously it has been demonstrated that hippocampal field excitatory postsynaptic potentials (fEPSPs) recover in correlation with synaptic changes in ex vivo slices[191]. We also show that a huge increase in SWR amplitude, rate and frequency occurs in line with synaptic sprouting reaching a balanced state of excitatory/inhibitory synaptic densities. These notions are supported by the fact that SWR generation relies on sufficiently large tonic excitatory activity followed by the action of reciprocally connected parvalbumin-positive basket cells[187]. These results indicate that a delicate balance is maintained between excitation and inhibition by microglia-related actions during the course of sprouting, allowing SWRs to emerge. Results from other studies support these notions, as partial depletion of microglia promoted asynchronous activity without overall change in frequency[116], as well as microglia depletion had been shown to decrease spontaneous or evoked glutamatergic activity[250]. In addition to synaptic reorganization, previously described neuroprotective roles mediated by P2Y12R and CX3CR1 signaling are also likely to be key contributors in recapitulating and maintaining the neuronal network in a homeostatic state. Through

these pathways, microglia could actively influence various neuronal parameters, including excitability and synaptic transmission. Moreover, local release of ATP and cytokines by activated microglia can alter neuronal membrane properties directly, changing action potential firing and synaptic plasticity[251]. It has also been established that microglia can dampen excess neuronal activity through the release of ATP acting on A1R[14]. These results further support the notion that microglia are critical in maintaining the neuronal network within a physiological regime after tissue disturbance.

5.8. Future directions

Our results demonstrate that microglia in acute slices undergo rapid phenotypic transformation towards a more reactive phenotype and can actively influence the neuronal network through altered microglia–neuron interactions. In particular, we highlighted the role of purinergic- and fractalkine-signaling in mediating these actions, which needs to be considered during ex vivo experimentation in the future. However, it is important to note that other signaling pathways could also influence microglia–neuron communication, including presently unknown forms of interactions. Since microglial morphology strongly reflects the state of the tissue and the progression of pathological actions, monitoring these changes and comparing related microglial phenotypes could facilitate the exploration of new underlying mechanisms. Furthermore, more refined ex vivo models and paradigms for tissue preparation could also be established by high throughput screenings of microglial features, as they represent an efficient and reliable readout for homeostatic state[252,253]. Previous attempts to facilitate the viability of ex vivo tissue samples mainly focused on neuronal readouts[160,163], our observations indicate that microglial features should also be considered during further developments. We also aim to highlight the importance of interactions between microglia and the neuronal network, which may be further emphasized by the sensitivity of microglia to a broad range of changes in their environment. While at present, the cellular composition of acute slices may not represent an undisturbed physiological state, ex vivo models represent instrumental tools for examining various factors contributing to the reactivity of microglia, with broad future implications to test how alterations in microglial function might contribute to certain pathologies. Further studies could also explore sex-related

differences, which could potentially influence the observed microglia-related effects. Testing the effect of different types of anesthetics within such conditions could also have important implications, since the widely used isoflurane before slice preparation has been shown to modulate microglial process dynamics[102]. Importantly, future research endeavors should aim to further elucidate the nuanced roles of microglia in pathological and physiological contexts. Our results demonstrate that acute slice preparations provide a powerful platform for investigating the roles and interactions of microglia with other constituents of the CNS. A deeper understanding of such mechanisms would be essential for the development of therapeutic interventions concerning a plethora of neurological diseases. Hopefully, our results will be useful in the future for other explorations and contribute to a better understanding of how microglia influence neural circuit dynamics in health and disease.

6. Conclusions

Results presented in this thesis explored injury-induced behavior of acute slice-resident microglia in a detailed, time-dependent manner. We utilized a newly developed, highly sensitive ATP sensor to monitor extracellular ATP dynamics, revealing elevated ATP levels near slice surfaces, with ATP gradients driving microglial dislocation and morphological transformation. Our findings indicate that both migratory behavior and transitioning into an amoeboid morphology are influenced by P2Y12R and CX3CR1 signaling. Additionally, our electrophysiological experiments indicate that microglia gradually depolarize during this process, while we identify NKCC1 channels as key mediators of ion-regulation contributing to microglial phenotype and function. Furthermore, we demonstrate the existence of a previously unknown form of purinergic activity deep within the tissue, characterized by focal ATP release events that persist for hours after slice preparation. This injury-induced, endogenous purinergic activity occurs across a wide age range and in multiple brain regions, exhibiting significant heterogeneity in event size, intensity, and duration. Microglia respond rapidly to these ATP events via P2Y12R- and CX3CR1-dependent fast process movements. In parallel, we observed robust, rapid downregulation of P2Y12R at both thick and thin microglial processes. Interestingly, despite P2Y12R downregulation, microglia retain their ability to extend processes toward ATP events, indicating that a sufficient number of receptors remain functional to sustain microglial responsiveness. Furthermore, our results reveal marked injury-induced alterations in microglia-neuron interactions in acute brain slices. While the prevalence of somatic junctions gradually decreases during incubation, the somatic area covered by microglial processes increases rapidly after cutting. In parallel, contact prevalence at GABAergic synapses shows a continuous decreasing trend, whereas contact numbers at glutamatergic synapses initially increase. In line with these observations, the absence of microglia impairs synaptic sprouting during the incubation process, suggesting that microglial interactions can directly influence synaptic regulation in acute slices. Finally, we revealed that microglia-related mechanisms actively promote the spontaneous emergence of neuronal synchrony in hippocampal slices, which mechanisms are also mediated by P2Y12R and CX3CR1 signaling. These findings underscore the dynamic role of microglia in acute slices, responding quickly to injury and modulating network structure and function to facilitate the restoration of neuronal activity.

7. Summary

Acute brain slices represent a well-established experimental approach for investigating the CNS from nanoscale events to complex circuits. Simultaneously, it also serves as an invaluable tool for examining microglia, the primary immunocompetent cellular population within the CNS. However, it is important to keep in mind that microglia exhibit rapid and dynamic phenotypic alteration due to injury introduced by the slice preparation process, which significantly influences microglial interactions with other CNS constituents. Our results demonstrate that injury-induced microglial phenotypes are actively engaging in processes that ultimately promote the reorganization of the neuronal network and facilitate the recapitulation of network activity. Along these lines, results discussed in this thesis imply that functional alterations of microglia should be considered by all studies using ex vivo models, since their immunogenic activation due to injury can also robustly influence the functioning of other CNS-resident cells. Importantly, while the process of slice preparation inherently involves tissue damage, it simultaneously provides a unique opportunity to gain insights into these microglia-related processes and their contributions to network functioning. Our findings provide a comprehensive framework for the functional investigation of microglial phenotypic transitions in a time-dependent manner, which could provide more insights into these processes in future research endeavors. Importantly there are still invaluable lessons to be learned about how changes in environmental conditions shape microglial phenotypes, which processes are likely to involve currently unknown pathways and mechanisms. Hopefully, these findings will inspire others to utilize these models in order to simulate time-dependent changes in microglial states. In addition, it would be equally beneficial to explore pathways which could inhibit such transitioning into reactive phenotypes. These experiments could facilitate the understanding and treatment of CNS diseases that are influenced by chronic alterations in microglial function, which concerns nearly all of our currently untreatable and most detrimental neurodegenerative disorders. These possibilities are highlighting the potential of acute slice models both as a tool for basic research and as a translational platform for the development of therapeutic strategies modulating microglial activity.

8. References

1. Herculano-Houzel, S. The glia/neuron ratio: How it varies uniformly across brain structures and species and what that means for brain physiology and evolution. *Glia* **62**, 1377–1391 (2014).
2. Mota, B. & Herculano-Houzel, S. All brains are made of this: a fundamental building block of brain matter with matching neuronal and glial masses. *Front. Neuroanat.* **8**, (2014).
3. Luo, L. Architectures of neuronal circuits. *Science* **373**, eabg7285 (2021).
4. Yuste, R. From the neuron doctrine to neural networks. *Nat Rev Neurosci* **16**, 487–497 (2015).
5. Cembrowski, M. S. & Spruston, N. Heterogeneity within classical cell types is the rule: lessons from hippocampal pyramidal neurons. *Nat Rev Neurosci* **20**, 193–204 (2019).
6. Molyneaux, B. J., Arlotta, P., Menezes, J. R. L. & Macklis, J. D. Neuronal subtype specification in the cerebral cortex. *Nat Rev Neurosci* **8**, 427–437 (2007).
7. Markram, H. *et al.* Interneurons of the neocortical inhibitory system. *Nat Rev Neurosci* **5**, 793–807 (2004).
8. Klausberger, T. & Somogyi, P. Neuronal Diversity and Temporal Dynamics: The Unity of Hippocampal Circuit Operations. *Science* **321**, 53–57 (2008).
9. Poulin, J.-F., Tasic, B., Hjerling-Leffler, J., Trimarchi, J. M. & Awatramani, R. Disentangling neural cell diversity using single-cell transcriptomics. *Nat Neurosci* **19**, 1131–1141 (2016).
10. Zhang, M. *et al.* Molecularly defined and spatially resolved cell atlas of the whole mouse brain. *Nature* **624**, 343–354 (2023).
11. Yao, Z. *et al.* A high-resolution transcriptomic and spatial atlas of cell types in the whole mouse brain. *Nature* **624**, 317–332 (2023).
12. Allen, N. J. & Lyons, D. A. Glia as architects of central nervous system formation and function. *Science* **362**, 181–185 (2018).
13. Ullian, E. M., Christopherson, K. S. & Barres, B. A. Role for glia in synaptogenesis. *Glia* **47**, 209–216 (2004).
14. Perea, G., Sur, M. & Araque, A. Neuron-glia networks: integral gear of brain function. *Front. Cell. Neurosci.* **8**, (2014).

15. Kugler, E. C., Greenwood, J. & MacDonald, R. B. The "Neuro-Glial-Vascular" Unit: The Role of Glia in Neurovascular Unit Formation and Dysfunction. *Front. Cell Dev. Biol.* **9**, (2021).
16. Cserép, C., Pósfai, B. & Dénes, Á. Shaping Neuronal Fate: Functional Heterogeneity of Direct Microglia-Neuron Interactions. *Neuron* **109**, 222–240 (2021).
17. Fields, R. D. & Stevens-Graham, B. New Insights into Neuron-Glia Communication. *Science* **298**, 556–562 (2002).
18. Rangel-Gomez, M. *et al.* Neuron–Glial Interactions: Implications for Plasticity, Behavior, and Cognition. *J. Neurosci.* **44**, (2024).
19. Agulhon, C. *et al.* What Is the Role of Astrocyte Calcium in Neurophysiology? *Neuron* **59**, 932–946 (2008).
20. Syková, E., Svoboda, J., Šimonová, Z. & Jendelová, P. Chapter 4: Role of astrocytes in ionic and volume homeostasis in spinal cord during development and injury. in *Progress in Brain Research* (eds. Yu, A. C. H., Hertz, L., Norenberg, M. D., Syková, E. & Waxman, S. G.) vol. 94 47–56 (Elsevier, 1992).
21. Theparambil, S. M. *et al.* Astrocytes regulate brain extracellular pH via a neuronal activity-dependent bicarbonate shuttle. *Nat Commun* **11**, 5073 (2020).
22. Araki, T., Ikegaya, Y. & Koyama, R. The effects of microglia- and astrocyte-derived factors on neurogenesis in health and disease. *European Journal of Neuroscience* **54**, 5880–5901 (2021).
23. Song, H., Stevens, C. F. & Gage, F. H. Astroglia induce neurogenesis from adult neural stem cells. *Nature* **417**, 39–44 (2002).
24. Cassé, F., Richetin, K. & Toni, N. Astrocytes' Contribution to Adult Neurogenesis in Physiology and Alzheimer's Disease. *Front. Cell. Neurosci.* **12**, (2018).
25. Kuhn, S., Gritti, L., Crooks, D. & Dombrowski, Y. Oligodendrocytes in Development, Myelin Generation and Beyond. *Cells* **8**, 1424 (2019).
26. Michalski, J.-P. & Kothary, R. Oligodendrocytes in a Nutshell. *Front. Cell. Neurosci.* **9**, (2015).
27. Bradl, M. & Lassmann, H. Oligodendrocytes: biology and pathology. *Acta Neuropathol* **119**, 37–53 (2010).

28. Duncan, G. J., Simkins, T. J. & Emery, B. Neuron-Oligodendrocyte Interactions in the Structure and Integrity of Axons. *Front. Cell Dev. Biol.* **9**, (2021).
29. Saab, A. S., Tzvetanova, I. D. & Nave, K.-A. The role of myelin and oligodendrocytes in axonal energy metabolism. *Current Opinion in Neurobiology* **23**, 1065–1072 (2013).
30. Hickman, S., Izzy, S., Sen, P., Morsett, L. & El Khoury, J. Microglia in neurodegeneration. *Nat Neurosci* **21**, 1359–1369 (2018).
31. Kwon, H. S. & Koh, S.-H. Neuroinflammation in neurodegenerative disorders: the roles of microglia and astrocytes. *Translational Neurodegeneration* **9**, 42 (2020).
32. Herz, J., Filiano, A. J., Wiltbank, A. T., Yogev, N. & Kipnis, J. Myeloid Cells in the Central Nervous System. *Immunity* **46**, 943–956 (2017).
33. Prinz, M., Priller, J., Sisodia, S. S. & Ransohoff, R. M. Heterogeneity of CNS myeloid cells and their roles in neurodegeneration. *Nat Neurosci* **14**, 1227–1235 (2011).
34. Myeloid Cells in the Central Nervous System: Immunity. https://www.cell.com/immunity/fulltext/S1074-7613(17)30235-2?sf94035833=1.
35. Bisht, K. *et al.* Capillary-associated microglia regulate vascular structure and function through PANX1-P2RY12 coupling in mice. *Nat Commun* **12**, 5289 (2021).
36. Császár, E. *et al.* Microglia modulate blood flow, neurovascular coupling, and hypoperfusion via purinergic actions. *Journal of Experimental Medicine* **219**, e20211071 (2022).
37. Badimon, A. *et al.* Negative feedback control of neuronal activity by microglia. *Nature* **586**, 417–423 (2020).
38. Dantzer, R. Neuroimmune Interactions: From the Brain to the Immune System and Vice Versa. *Physiological Reviews* **98**, 477–504 (2018).
39. Wohleb, E. S., Franklin, T., Iwata, M. & Duman, R. S. Integrating neuroimmune systems in the neurobiology of depression. *Nat Rev Neurosci* **17**, 497–511 (2016).
40. Chen, Y. & Colonna, M. Microglia in Alzheimer's disease at single-cell level. Are there common patterns in humans and mice? *Journal of Experimental Medicine* **218**, e20202717 (2021).
41. Zhang, X., Zhang, R., Nisa Awan, M. U. & Bai, J. The Mechanism and Function of Glia in Parkinson's Disease. *Front. Cell. Neurosci.* **16**, (2022).

42. Petzold, A. *et al.* Markers for different glial cell responses in multiple sclerosis: clinical and pathological correlations. *Brain* **125**, 1462–1473 (2002).
43. Bennett, M. L. & Viaene, A. N. What are activated and reactive glia and what is their role in neurodegeneration? *Neurobiology of Disease* **148**, 105172 (2021).
44. Mueller, B., Figueroa, A. & Robinson-Papp, J. Structural and functional connections between the autonomic nervous system, hypothalamic–pituitary–adrenal axis, and the immune system: a context and time dependent stress response network. *Neurol Sci* **43**, 951–960 (2022).
45. Nance, D. M. & Sanders, V. M. Autonomic innervation and regulation of the immune system (1987–2007). *Brain, Behavior, and Immunity* **21**, 736–745 (2007).
46. Dantzer, R. Neuroimmune Interactions: From the Brain to the Immune System and Vice Versa. *Physiol Rev* **98**, 477–504 (2018).
47. Sharma, D. & Farrar, J. D. Adrenergic regulation of immune cell function and inflammation. *Semin Immunopathol* **42**, 709–717 (2020).
48. Rogausch, H., del Rey, A., Oertel, J. & Besedovsky, H. O. Norepinephrine stimulates lymphoid cell mobilization from the perfused rat spleen via β-adrenergic receptors. *American Journal of Physiology-Regulatory, Integrative and Comparative Physiology* **276**, R724–R730 (1999).
49. Miyata, S. Glial functions in the blood-brain communication at the circumventricular organs. *Front. Neurosci.* **16**, (2022).
50. Cottrell, G. T. & Ferguson, A. V. Sensory circumventricular organs: central roles in integrated autonomic regulation. *Regulatory Peptides* **117**, 11–23 (2004).
51. Dantzer, R., Konsman, J.-P., Bluthé, R.-M. & Kelley, K. W. Neural and humoral pathways of communication from the immune system to the brain: parallel or convergent? *Autonomic Neuroscience* **85**, 60–65 (2000).
52. Croese, T., Castellani, G. & Schwartz, M. Immune cell compartmentalization for brain surveillance and protection. *Nat Immunol* **22**, 1083–1092 (2021).
53. Sun, R. & Jiang, H. Border-associated macrophages in the central nervous system. *J Neuroinflammation* **21**, 67 (2024).
54. Prinz, M., Masuda, T., Wheeler, M. A. & Quintana, F. J. Microglia and Central Nervous System–Associated Macrophages—From Origin to Disease Modulation. *Annual Review of Immunology* **39**, 251–277 (2021).

55. Goldmann, T. *et al.* Origin, fate and dynamics of macrophages at CNS interfaces. *Nat Immunol* **17**, 797–805 (2016).
56. Silvin, A., Qian, J. & Ginhoux, F. Brain macrophage development, diversity and dysregulation in health and disease. *Cell Mol Immunol* **20**, 1277–1289 (2023).
57. Goldmann, T. *et al.* Origin, fate and dynamics of macrophages at central nervous system interfaces. *Nat Immunol* **17**, 797–805 (2016).
58. Prinz, M. & Priller, J. Microglia and brain macrophages in the molecular age: from origin to neuropsychiatric disease. *Nat Rev Neurosci* **15**, 300–312 (2014).
59. Ginhoux, F. *et al.* Fate Mapping Analysis Reveals That Adult Microglia Derive from Primitive Macrophages. *Science* **330**, 841–845 (2010).
60. Kierdorf, K. *et al.* Microglia emerge from erythromyeloid precursors via Pu.1- and Irf8-dependent pathways. *Nat Neurosci* **16**, 273–280 (2013).
61. Gomez Perdiguero, E. *et al.* Tissue-resident macrophages originate from yolk-sac-derived erythro-myeloid progenitors. *Nature* **518**, 547–551 (2015).
62. Rezaie, P. & Male, D. Colonisation of the developing human brain and spinal cord by microglia: a review. *Microscopy Research and Technique* **45**, 359–382 (1999).
63. Askew, K. *et al.* Coupled Proliferation and Apoptosis Maintain the Rapid Turnover of Microglia in the Adult Brain. *Cell Reports* **18**, 391–405 (2017).
64. Füger, P. *et al.* Microglia turnover with aging and in an Alzheimer's model via long-term in vivo single-cell imaging. *Nat Neurosci* **20**, 1371–1376 (2017).
65. Huang, Y. *et al.* Repopulated microglia are solely derived from the proliferation of residual microglia after acute depletion. *Nat Neurosci* **21**, 530–540 (2018).
66. Healy, L. M., Zia, S. & Plemel, J. R. Towards a definition of microglia heterogeneity. *Commun Biol* **5**, 1–6 (2022).
67. Kim, S. U. & de Vellis, J. Microglia in health and disease. *Journal of Neuroscience Research* **81**, 302–313 (2005).
68. Saijo, K. & Glass, C. K. Microglial cell origin and phenotypes in health and disease. *Nat Rev Immunol* **11**, 775–787 (2011).
69. Masuda, T., Sankowski, R., Staszewski, O. & Prinz, M. Microglia Heterogeneity in the Single-Cell Era. *Cell Reports* **30**, 1271–1281 (2020).
70. Hickman, S. E. *et al.* The microglial sensome revealed by direct RNA sequencing. *Nat Neurosci* **16**, 1896–1905 (2013).

71. Butovsky, O. & Weiner, H. L. Microglial signatures and their role in health and disease. *Nat Rev Neurosci* **19**, 622–635 (2018).
72. Vecchiarelli, H. A. & Tremblay, M.-È. Microglial Transcriptional Signatures in the Central Nervous System: Toward A Future of Unraveling Their Function in Health and Disease. *Annual Review of Genetics* **57**, 65–86 (2023).
73. Pixley, F. J. & Stanley, E. R. CSF-1 regulation of the wandering macrophage: complexity in action. *Trends in Cell Biology* **14**, 628–638 (2004).
74. Green, K. N., Crapser, J. D. & Hohsfield, L. A. To Kill a Microglia: A Case for CSF1R Inhibitors. *Trends in Immunology* **41**, 771–784 (2020).
75. Bennett, F. C. *et al.* A Combination of Ontogeny and CNS Environment Establishes Microglial Identity. *Neuron* **98**, 1170-1183.e8 (2018).
76. Bedolla, A. *et al.* Adult microglial TGFβ1 is required for microglia homeostasis via an autocrine mechanism to maintain cognitive function in mice. *Nat Commun* **15**, 5306 (2024).
77. Jung, S. *et al.* Analysis of Fractalkine Receptor CX3CR1 Function by Targeted Deletion and Green Fluorescent Protein Reporter Gene Insertion. *Molecular and Cellular Biology* **20**, 4106–4114 (2000).
78. Pawelec, P., Ziemka-Nalecz, M., Sypecka, J. & Zalewska, T. The Impact of the CX3CL1/CX3CR1 Axis in Neurological Disorders. *Cells* **9**, 2277 (2020).
79. Gyoneva, S. *et al.* Cx3cr1-deficient microglia exhibit a premature aging transcriptome. *Life Science Alliance* **2**, (2019).
80. Wolf, Y., Yona, S., Kim, K.-W. & Jung, S. Microglia, seen from the CX3CR1 angle. *Front. Cell. Neurosci.* **7**, (2013).
81. Clark, A. K. & Malcangio, M. Microglial signalling mechanisms: Cathepsin S and Fractalkine. *Experimental Neurology* **234**, 283–292 (2012).
82. Clark, A. K., Wodarski, R., Guida, F., Sasso, O. & Malcangio, M. Cathepsin S release from primary cultured microglia is regulated by the P2X7 receptor. *Glia* **58**, 1710–1726 (2010).
83. Ulland, T. K. *et al.* TREM2 Maintains Microglial Metabolic Fitness in Alzheimer's Disease. *Cell* **170**, 649-663.e13 (2017).
84. Kim, S.-M. *et al.* TREM2 promotes Aβ phagocytosis by upregulating C/EBPα-dependent CD36 expression in microglia. *Sci Rep* **7**, 11118 (2017).

85. Zhao, Y. *et al.* TREM2 Is a Receptor for β-Amyloid that Mediates Microglial Function. *Neuron* **97**, 1023-1031.e7 (2018).
86. Wang, Y. *et al.* TREM2-mediated early microglial response limits diffusion and toxicity of amyloid plaques. *Journal of Experimental Medicine* **213**, 667–675 (2016).
87. Lin, B. *et al.* GPR34 senses demyelination to promote neuroinflammation and pathologies. *Cell Mol Immunol* **21**, 1131–1144 (2024).
88. Preissler, J. *et al.* Altered microglial phagocytosis in GPR34-deficient mice. *Glia* **63**, 206–215 (2015).
89. Sipe, G. O. *et al.* Microglial P2Y12 is necessary for synaptic plasticity in mouse visual cortex. *Nat Commun* **7**, 10905 (2016).
90. Ming, L., Hu, D., Zuo, C. & Zhang, W. G protein-coupled P2Y12 receptor is involved in the progression of neuropathic pain. *Biomedicine & Pharmacotherapy* **162**, 114713 (2023).
91. Cserép, C. *et al.* Microglia monitor and protect neuronal function through specialized somatic purinergic junctions. *Science* **367**, 528–537 (2020).
92. Davalos, D. *et al.* ATP mediates rapid microglial response to local brain injury in vivo. *Nat Neurosci* **8**, 752–758 (2005).
93. Nimmerjahn, A., Kirchhoff, F. & Helmchen, F. Resting Microglial Cells Are Highly Dynamic Surveillants of Brain Parenchyma in Vivo. *Science* **308**, 1314–1318 (2005).
94. Satoh, J. *et al.* TMEM119 marks a subset of microglia in the human brain. *Neuropathology* **36**, 39–49 (2016).
95. Masuda, T. *et al.* Novel Hexb-based tools for studying microglia in the CNS. *Nat Immunol* **21**, 802–815 (2020).
96. Dutta, G., Barber, D. S., Zhang, P., Doperalski, N. J. & Liu, B. Involvement of dopaminergic neuronal cystatin C in neuronal injury-induced microglial activation and neurotoxicity. *Journal of Neurochemistry* **122**, 752–763 (2012).
97. Toshihiko Miyake *et al.* Up-regulation of cystatin C by microglia in the rat facial nucleus following axotomy. *Molecular Brain Research* **37**, 273–282 (1996).

98. Tsuji, D., Kuroki, A., Ishibashi, Y., Itakura, T. & Itoh, K. Metabolic correction in microglia derived from Sandhoff disease model mice. *Journal of Neurochemistry* **94**, 1631–1638 (2005).
99. Thion, M. S. *et al.* Microbiome Influences Prenatal and Adult Microglia in a Sex-Specific Manner. *Cell* **172**, 500-516.e16 (2018).
100. Guzmán-Ruiz, M. A. *et al.* Circadian modulation of microglial physiological processes and immune responses. *Glia* **71**, 155–167 (2023).
101. Xu, Y., Gao, W., Sun, Y. & Wu, M. New insight on microglia activation in neurodegenerative diseases and therapeutics. *Front. Neurosci.* **17**, (2023).
102. Hristovska, I. & Pascual, O. Deciphering Resting Microglial Morphology and Process Motility from a Synaptic Prospect. *Front. Integr. Neurosci.* **9**, (2016).
103. Hanisch, U.-K. & Kettenmann, H. Microglia: active sensor and versatile effector cells in the normal and pathologic brain. *Nat Neurosci* **10**, 1387–1394 (2007).
104. Ohsawa, K. & Kohsaka, S. Dynamic motility of microglia: Purinergic modulation of microglial movement in the normal and pathological brain. *Glia* **59**, 1793–1799 (2011).
105. Madry, C. *et al.* Microglial Ramification, Surveillance, and Interleukin-1β Release Are Regulated by the Two-Pore Domain K+ Channel THIK-1. *Neuron* **97**, 299-312.e6 (2018).
106. Lénárt, N., Cserép, C., Császár, E., Pósfai, B. & Dénes, Á. Microglia–neuron–vascular interactions in ischemia. *Glia* **72**, 833–856 (2024).
107. Bonvento, G. & Bolaños, J. P. Astrocyte-neuron metabolic cooperation shapes brain activity. *Cell Metabolism* **33**, 1546–1564 (2021).
108. Zhao, X., Eyo, U. B., Murugan, M. & Wu, L.-J. Microglial interactions with the neurovascular system in physiology and pathology. *Developmental Neurobiology* **78**, 604–617 (2018).
109. Joshi, A. U. & Mochly-Rosen, D. Mortal engines: Mitochondrial bioenergetics and dysfunction in neurodegenerative diseases. *Pharmacological Research* **138**, 2–15 (2018).
110. Sugiura, A., McLelland, G., Fon, E. A. & McBride, H. M. A new pathway for mitochondrial quality control: mitochondrial-derived vesicles. *The EMBO Journal* **33**, 2142–2156 (2014).

111. Wake, H., Moorhouse, A. J., Jinno, S., Kohsaka, S. & Nabekura, J. Resting Microglia Directly Monitor the Functional State of Synapses In Vivo and Determine the Fate of Ischemic Terminals. *J. Neurosci.* **29**, 3974–3980 (2009).
112. Tremblay, M.-È., Lowery, R. L. & Majewska, A. K. Microglial Interactions with Synapses Are Modulated by Visual Experience. *PLOS Biology* **8**, e1000527 (2010).
113. Cserép, C. *et al.* Microglial control of neuronal development via somatic purinergic junctions. *Cell Rep* **40**, 111369 (2022).
114. Cangalaya, C., Stoyanov, S., Fischer, K.-D. & Dityatev, A. Light-induced engagement of microglia to focally remodel synapses in the adult brain. *eLife* **9**, e58435 (2020).
115. Miyamoto, A. *et al.* Microglia contact induces synapse formation in developing somatosensory cortex. *Nat Commun* **7**, 12540 (2016).
116. Ronzano, R. *et al.* Microglia-neuron interaction at nodes of Ranvier depends on neuronal activity through potassium release and contributes to remyelination. *Nat Commun* **12**, 5219 (2021).
117. Baalman, K. *et al.* Axon Initial Segment–Associated Microglia. *J. Neurosci.* **35**, 2283–2292 (2015).
118. Kato, G. *et al.* Microglial Contact Prevents Excess Depolarization and Rescues Neurons from Excitotoxicity. *eNeuro* **3**, (2016).
119. Akiyoshi, R. *et al.* Microglia Enhance Synapse Activity to Promote Local Network Synchronization. *eNeuro* **5**, (2018).
120. Czapski, G. A. & Strosznajder, J. B. Glutamate and GABA in Microglia-Neuron Cross-Talk in Alzheimer's Disease. *International Journal of Molecular Sciences* **22**, 11677 (2021).
121. Rodríguez, A. M., Rodríguez, J. & Giambartolomei, G. H. Microglia at the Crossroads of Pathogen-Induced Neuroinflammation. *ASN Neuro* **14**, 17590914221104566 (2022).
122. Szepesi, Z., Manouchehrian, O., Bachiller, S. & Deierborg, T. Bidirectional Microglia–Neuron Communication in Health and Disease. *Front. Cell. Neurosci.* **12**, (2018).

123. Fung, T. C., Olson, C. A. & Hsiao, E. Y. Interactions between the microbiota, immune and nervous systems in health and disease. *Nat Neurosci* **20**, 145–155 (2017).
124. Sharon, G., Sampson, T. R., Geschwind, D. H. & Mazmanian, S. K. The Central Nervous System and the Gut Microbiome. *Cell* **167**, 915–932 (2016).
125. Cunningham, C. L., Martínez-Cerdeño, V. & Noctor, S. C. Microglia Regulate the Number of Neural Precursor Cells in the Developing Cerebral Cortex. *J. Neurosci.* **33**, 4216–4233 (2013).
126. Diaz-Aparicio, I. *et al.* Microglia Actively Remodel Adult Hippocampal Neurogenesis through the Phagocytosis Secretome. *J. Neurosci.* **40**, 1453–1482 (2020).
127. Aarum, J., Sandberg, K., Haeberlein, S. L. B. & Persson, M. A. A. Migration and differentiation of neural precursor cells can be directed by microglia. *Proceedings of the National Academy of Sciences* **100**, 15983–15988 (2003).
128. Schafer, D. P. *et al.* Microglia Sculpt Postnatal Neural Circuits in an Activity and Complement-Dependent Manner. *Neuron* **74**, 691–705 (2012).
129. Sierra, A. *et al.* Microglia Shape Adult Hippocampal Neurogenesis through Apoptosis-Coupled Phagocytosis. *Cell Stem Cell* **7**, 483–495 (2010).
130. Yenari, M. A., Kauppinen, T. M. & Swanson, R. A. Microglial Activation in Stroke: Therapeutic Targets. *Neurotherapeutics* **7**, 378–391 (2010).
131. Stence, N., Waite, M. & Dailey, M. E. Dynamics of microglial activation: A confocal time-lapse analysis in hippocampal slices. *Glia* **33**, 256–266 (2001).
132. Ransohoff, R. M. A polarizing question: do M1 and M2 microglia exist? *Nat Neurosci* **19**, 987–991 (2016).
133. Paolicelli, R. C. *et al.* Microglia states and nomenclature: A field at its crossroads. *Neuron* **110**, 3458–3483 (2022).
134. Dubbelaar, M. L., Kracht, L., Eggen, B. J. L. & Boddeke, E. W. G. M. The Kaleidoscope of Microglial Phenotypes. *Front. Immunol.* **9**, (2018).
135. Martins-Ferreira, R. *et al.* The Human Microglia Atlas (HuMicA) unravels changes in disease-associated microglia subsets across neurodegenerative conditions. *Nat Commun* **16**, 739 (2025).

136. Greve, M. W. & Zink, B. J. Pathophysiology of traumatic brain injury. *Mount Sinai Journal of Medicine: A Journal of Translational and Personalized Medicine* **76**, 97–104 (2009).
137. Ng, S. Y. & Lee, A. Y. W. Traumatic Brain Injuries: Pathophysiology and Potential Therapeutic Targets. *Front. Cell. Neurosci.* **13**, (2019).
138. Alam, A. *et al.* Cellular infiltration in traumatic brain injury. *J Neuroinflammation* **17**, 328 (2020).
139. Morganti-Kossmann, M. C., Semple, B. D., Hellewell, S. C., Bye, N. & Ziebell, J. M. The complexity of neuroinflammation consequent to traumatic brain injury: from research evidence to potential treatments. *Acta Neuropathol* **137**, 731–755 (2019).
140. Endres, M., Dirnagl, U. & Moskowitz, M. A. Chapter 2 The ischemic cascade and mediators of ischemic injury. in *Handbook of Clinical Neurology* vol. 92 31–41 (Elsevier, 2008).
141. Sulhan, S., Lyon, K. A., Shapiro, L. A. & Huang, J. H. Neuroinflammation and blood–brain barrier disruption following traumatic brain injury: Pathophysiology and potential therapeutic targets. *Journal of Neuroscience Research* **98**, 19–28 (2020).
142. Shlosberg, D., Benifla, M., Kaufer, D. & Friedman, A. Blood–brain barrier breakdown as a therapeutic target in traumatic brain injury. *Nat Rev Neurol* **6**, 393–403 (2010).
143. Vénéreau, E., Ceriotti, C. & Bianchi, M. E. DAMPs from Cell Death to New Life. *Front. Immunol.* **6**, (2015).
144. Williams, A. J., Wei, H. H., Dave, J. R. & Tortella, F. C. Acute and delayed neuroinflammatory response following experimental penetrating ballistic brain injury in the rat. *J Neuroinflammation* **4**, 17 (2007).
145. Werner, C. & Engelhard, K. Pathophysiology of traumatic brain injury. *BJA: British Journal of Anaesthesia* **99**, 4–9 (2007).
146. Qin, C. *et al.* Signaling pathways involved in ischemic stroke: molecular mechanisms and therapeutic interventions. *Sig Transduct Target Ther* **7**, 1–29 (2022).
147. Lai, T. W., Zhang, S. & Wang, Y. T. Excitotoxicity and stroke: Identifying novel targets for neuroprotection. *Progress in Neurobiology* **115**, 157–188 (2014).

148. Murao, A., Aziz, M., Wang, H., Brenner, M. & Wang, P. Release mechanisms of major DAMPs. *Apoptosis* **26**, 152–162 (2021).
149. Trahtemberg, U. & Mevorach, D. Apoptotic Cells Induced Signaling for Immune Homeostasis in Macrophages and Dendritic Cells. *Front. Immunol.* **8**, (2017).
150. Zhao, S. *et al.* Regulation of microglial activation in stroke. *Acta Pharmacol Sin* **38**, 445–458 (2017).
151. Obukohwo, O. M., Oreoluwa, O. A., Andrew, U. O. & Williams, U. E. Microglia-mediated neuroinflammation in traumatic brain injury: a review. *Mol Biol Rep* **51**, 1073 (2024).
152. Karve, I. P., Taylor, J. M. & Crack, P. J. The contribution of astrocytes and microglia to traumatic brain injury. *British Journal of Pharmacology* **173**, 692–702 (2016).
153. Haynes, S. E. *et al.* The P2Y12 receptor regulates microglial activation by extracellular nucleotides. *Nat Neurosci* **9**, 1512–1519 (2006).
154. Qin, C. *et al.* Dual Functions of Microglia in Ischemic Stroke. *Neurosci. Bull.* **35**, 921–933 (2019).
155. Ma, Y., Wang, J., Wang, Y. & Yang, G.-Y. The biphasic function of microglia in ischemic stroke. *Progress in Neurobiology* **157**, 247–272 (2017).
156. Michaud, M. *et al.* Proinflammatory Cytokines, Aging, and Age-Related Diseases. *Journal of the American Medical Directors Association* **14**, 877–882 (2013).
157. Bauernfeind, F., Niepmann, S., Knolle, P. A. & Hornung, V. Aging-Associated TNF Production Primes Inflammasome Activation and NLRP3-Related Metabolic Disturbances. *The Journal of Immunology* **197**, 2900–2908 (2016).
158. Tylutka, A., Walas, Ł. & Zembron-Lacny, A. Level of IL-6, TNF, and IL-1β and age-related diseases: a systematic review and meta-analysis. *Front. Immunol.* **15**, (2024).
159. Ponomarev, E. D., Veremeyko, T. & Weiner, H. L. MicroRNAs are universal regulators of differentiation, activation, and polarization of microglia and macrophages in normal and diseased CNS. *Glia* **61**, 91–103 (2013).
160. Cherry, J. D., Olschowka, J. A. & O'Banion, M. K. Neuroinflammation and M2 microglia: the good, the bad, and the inflamed. *J Neuroinflammation* **11**, 98 (2014).

161. Gibson, I. M. & McIlwain, H. Continuous recording of changes in membrane potential in mammalian cerebral tissues in vitro; recovery after depolarization by added substances. *The Journal of Physiology* **176**, 261–283 (1965).
162. Li, C.-L. & McIlwain, H. Maintenance of resting membrane potentials in slices of mammalian cerebral cortex and other tissues in vitro. *The Journal of Physiology* **139**, 178–190 (1957).
163. Bliss, T. V. P., Collingridge, G. L., Morris, R. G. M. & Lømo, T. The discovery of long-term potentiation. *Philosophical Transactions of the Royal Society of London. Series B: Biological Sciences* **358**, 617–620 (2003).
164. Bliss, T. V. P. & Lømo, T. Long-lasting potentiation of synaptic transmission in the dentate area of the anaesthetized rabbit following stimulation of the perforant path. *The Journal of Physiology* **232**, 331–356 (1973).
165. Ting, J. T., Daigle, T. L., Chen, Q. & Feng, G. Acute brain slice methods for adult and aging animals: application of targeted patch clampanalysis and optogenetics. *Methods Mol Biol* **1183**, 221–242 (2014).
166. McIlwain, H., Buchel, L. & Cheshire, J. D. The inorganic phosphate and phosphocreatine of brain especially during metabolism in vitro. *Biochem J* **48**, 12–20 (1951).
167. Collingridge, G. L. The brain slice preparation: a tribute to the pioneer Henry McIlwain. *Journal of Neuroscience Methods* **59**, 5–9 (1995).
168. Lipton, P. *et al.* Making the best of brain slices; comparing preparative methods. *Journal of Neuroscience Methods* **59**, 151–156 (1995).
169. Ting, J. T. *et al.* Preparation of Acute Brain Slices Using an Optimized N-Methyl-D-glucamine Protective Recovery Method. *JoVE (Journal of Visualized Experiments)* e53825 (2018) doi:10.3791/53825.
170. Eguchi, K. *et al.* Advantages of Acute Brain Slices Prepared at Physiological Temperature in the Characterization of Synaptic Functions. *Frontiers in Cellular Neuroscience* **14**, (2020).
171. Ankri, L., Yarom, Y. & Uusisaari, M. Y. Slice It Hot: Acute Adult Brain Slicing in Physiological Temperature. *JoVE (Journal of Visualized Experiments)* e52068 (2014) doi:10.3791/52068.

172. Jones, R. S. G., da Silva, A. B., Whittaker, R. G., Woodhall, G. L. & Cunningham, M. O. Human brain slices for epilepsy research: Pitfalls, solutions and future challenges. *Journal of Neuroscience Methods* **260**, 221–232 (2016).
173. Mathis, D. M., Furman, J. L. & Norris, C. M. Preparation of Acute Hippocampal Slices from Rats and Transgenic Mice for the Study of Synaptic Alterations during Aging and Amyloid Pathology. *JoVE (Journal of Visualized Experiments)* e2330 (2011) doi:10.3791/2330.
174. Lee, K. H., Cha, M. & Lee, B. H. Neuroprotective Effect of Antioxidants in the Brain. *International Journal of Molecular Sciences* **21**, 7152 (2020).
175. Farhi, S. L. *et al.* Wide-Area All-Optical Neurophysiology in Acute Brain Slices. *J. Neurosci.* **39**, 4889–4908 (2019).
176. Loryan, I., Fridén, M. & Hammarlund-Udenaes, M. The brain slice method for studying drug distribution in the CNS. *Fluids Barriers CNS* **10**, 6 (2013).
177. Delbridge, A. R. D. *et al.* Organotypic Brain Slice Culture Microglia Exhibit Molecular Similarity to Acutely-Isolated Adult Microglia and Provide a Platform to Study Neuroinflammation. *Front. Cell. Neurosci.* **14**, (2020).
178. Kettenmann, H., Hanisch, U.-K., Noda, M. & Verkhratsky, A. Physiology of Microglia. *Physiological Reviews* **91**, 461–553 (2011).
179. Lein, P. J., Barnhart, C. D. & Pessah, I. N. Acute Hippocampal Slice Preparation and Hippocampal Slice Cultures. in *In Vitro Neurotoxicology: Methods and Protocols* (eds. Costa, L. G., Giordano, G. & Guizzetti, M.) 115–134 (Humana Press, Totowa, NJ, 2011). doi:10.1007/978-1-61779-170-3_8.
180. Gosselin, D. *et al.* An environment-dependent transcriptional network specifies human microglia identity. *Science* **356**, eaal3222 (2017).
181. Krabbe, G. *et al.* Functional Impairment of Microglia Coincides with Beta-Amyloid Deposition in Mice with Alzheimer-Like Pathology. *PLOS ONE* **8**, e60921 (2013).
182. Aires, V. *et al.* CD22 Blockage Restores Age-Related Impairments of Microglia Surveillance Capacity. *Front. Immunol.* **12**, (2021).
183. Avignone, E., Ulmann, L., Levavasseur, F., Rassendren, F. & Audinat, E. Status Epilepticus Induces a Particular Microglial Activation State Characterized by Enhanced Purinergic Signaling. *J. Neurosci.* **28**, 9133–9144 (2008).

184. Gyoneva, S. & Traynelis, S. F. Norepinephrine Modulates the Motility of Resting and Activated Microglia via Different Adrenergic Receptors *. *Journal of Biological Chemistry* **288**, 15291–15302 (2013).
185. Gyoneva, S., Swanger, S. A., Zhang, J., Weinshenker, D. & Traynelis, S. F. Altered motility of plaque-associated microglia in a model of Alzheimer's disease. *Neuroscience* **330**, 410–420 (2016).
186. Krabbe, G. *et al.* Activation of serotonin receptors promotes microglial injury-induced motility but attenuates phagocytic activity. *Brain, Behavior, and Immunity* **26**, 419–428 (2012).
187. Petersen, M. A. & Dailey, M. E. Diverse microglial motility behaviors during clearance of dead cells in hippocampal slices. *Glia* **46**, 195–206 (2004).
188. Boucsein, C. *et al.* Purinergic receptors on microglial cells: functional expression in acute brain slices and modulation of microglial activation in vitro. *European Journal of Neuroscience* **17**, 2267–2276 (2003).
189. Aires, V. *et al.* CD22 Blockage Restores Age-Related Impairments of Microglia Surveillance Capacity. *Front Immunol* **12**, 684430 (2021).
190. Takano, T. *et al.* Rapid manifestation of reactive astrogliosis in acute hippocampal brain slices. *Glia* **62**, 78–95 (2014).
191. Heindl, S. *et al.* Automated Morphological Analysis of Microglia After Stroke. *Front. Cell. Neurosci.* **12**, (2018).
192. Morrison, H., Young, K., Qureshi, M., Rowe, R. K. & Lifshitz, J. Quantitative microglia analyses reveal diverse morphologic responses in the rat cortex after diffuse brain injury. *Sci Rep* **7**, 13211 (2017).
193. Bourne, J. N., Kirov, S. A., Sorra, K. E. & Harris, K. M. Warmer preparation of hippocampal slices prevents synapse proliferation that might obscure LTP-related structural plasticity. *Neuropharmacology* **52**, 55–59 (2007).
194. Kirov, S. A., Sorra, K. E. & Harris, K. M. Slices Have More Synapses than Perfusion-Fixed Hippocampus from both Young and Mature Rats. *J. Neurosci.* **19**, 2876–2886 (1999).
195. Trivino-Paredes, J. S., Nahirney, P. C., Pinar, C., Grandes, P. & Christie, B. R. Acute slice preparation for electrophysiology increases spine numbers equivalently in the

male and female juvenile hippocampus: a DiI labeling study. *Journal of Neurophysiology* **122**, 958–969 (2019).

196. Holderith, N., Heredi, J., Kis, V. & Nusser, Z. A High-Resolution Method for Quantitative Molecular Analysis of Functionally Characterized Individual Synapses. *Cell Reports* **32**, 107968 (2020).
197. Avignone, E., Milior, G., Arnoux, I. & Audinat, E. Electrophysiological Investigation of Microglia. in *Microglia: Methods and Protocols* (eds. Garaschuk, O. & Verkhratsky, A.) 111–125 (Springer, New York, NY, 2019). doi:10.1007/978-1-4939-9658-2_9.
198. Wu, C., Luk, W. P., Gillis, J., Skinner, F. & Zhang, L. Size Does Matter: Generation of Intrinsic Network Rhythms in Thick Mouse Hippocampal Slices. *Journal of Neurophysiology* **93**, 2302–2317 (2005).
199. Schlingloff, D., Káli, S., Freund, T. F., Hájos, N. & Gulyás, A. I. Mechanisms of Sharp Wave Initiation and Ripple Generation. *J. Neurosci.* **34**, 11385–11398 (2014).
200. Boucsein, C., Kettenmann, H. & Nolte, C. Electrophysiological properties of microglial cells in normal and pathologic rat brain slices. *European Journal of Neuroscience* **12**, 2049–2058 (2000).
201. Avignone, E., Milior, G., Arnoux, I. & Audinat, E. Electrophysiological Investigation of Microglia. in *Microglia: Methods and Protocols* (eds. Garaschuk, O. & Verkhratsky, A.) 111–125 (Springer, New York, NY, 2019). doi:10.1007/978-1-4939-9658-2_9.
202. Holtman, I. R. *et al.* Induction of a common microglia gene expression signature by aging and neurodegenerative conditions: a co-expression meta-analysis. *acta neuropathol commun* **3**, 31 (2015).
203. Virtanen, M. A., Uvarov, P., Hübner, C. A. & Kaila, K. NKCC1, an Elusive Molecular Target in Brain Development: Making Sense of the Existing Data. *Cells* **9**, 2607 (2020).
204. Ben-Ari, Y. NKCC1 Chloride Importer Antagonists Attenuate Many Neurological and Psychiatric Disorders. *Trends in Neurosciences* **40**, 536–554 (2017).
205. Kharod, S. C., Kang, S. K. & Kadam, S. D. Off-Label Use of Bumetanide for Brain Disorders: An Overview. *Front. Neurosci.* **13**, (2019).

206. Eder, C., Klee, R. & Heinemann, U. Involvement of Stretch-Activated Cl− Channels in Ramification of Murine Microglia. *J. Neurosci.* **18**, 7127–7137 (1998).
207. Ducharme, G., Newell, E. W., Pinto, C. & Schlichter, L. C. Small-conductance Cl– channels contribute to volume regulation and phagocytosis in microglia.
208. Wu, Z. *et al.* An ultrasensitive GRAB sensor for detecting extracellular ATP in vitro and in vivo. 2021.02.24.432680 Preprint at https://doi.org/10.1101/2021.02.24.432680 (2021).
209. Keller, D., Erö, C. & Markram, H. Cell Densities in the Mouse Brain: A Systematic Review. *Front. Neuroanat.* **12**, (2018).
210. Elmore, M. R. P. *et al.* Colony-Stimulating Factor 1 Receptor Signaling Is Necessary for Microglia Viability, Unmasking a Microglia Progenitor Cell in the Adult Brain. *Neuron* **82**, 380–397 (2014).
211. Han, J., Harris, R. A. & Zhang, X.-M. An updated assessment of microglia depletion: current concepts and future directions. *Mol Brain* **10**, 25 (2017).
212. Strackeljan, L. *et al.* Microglia Depletion-Induced Remodeling of Extracellular Matrix and Excitatory Synapses in the Hippocampus of Adult Mice. *Cells* **10**, 1862 (2021).
213. Ramesh, G., MacLean, A. G. & Philipp, M. T. Cytokines and Chemokines at the Crossroads of Neuroinflammation, Neurodegeneration, and Neuropathic Pain. *Mediators of Inflammation* **2013**, 480739 (2013).
214. Buzsáki, G. Hippocampal sharp wave-ripple: A cognitive biomarker for episodic memory and planning. *Hippocampus* **25**, 1073–1188 (2015).
215. Hájos, N. *et al.* Maintaining network activity in submerged hippocampal slices: importance of oxygen supply. *European Journal of Neuroscience* **29**, 319–327 (2009).
216. Hájos, N. *et al.* Input-Output Features of Anatomically Identified CA3 Neurons during Hippocampal Sharp Wave/Ripple Oscillation In Vitro. *J. Neurosci.* **33**, 11677–11691 (2013).
217. Hájos, N. & Mody, I. Establishing a physiological environment for visualized in vitro brain slice recordings by increasing oxygen supply and modifying aCSF content. *Journal of Neuroscience Methods* **183**, 107–113 (2009).

218. Carbonell, W. S., Murase, S.-I., Horwitz, A. F. & Mandell, J. W. Migration of Perilesional Microglia after Focal Brain Injury and Modulation by CC Chemokine Receptor 5: An In Situ Time-Lapse Confocal Imaging Study. *J. Neurosci.* **25**, 7040–7047 (2005).
219. Yu, F. *et al.* Phagocytic microglia and macrophages in brain injury and repair. *CNS Neuroscience & Therapeutics* **28**, 1279–1293 (2022).
220. Chen, Z. & Trapp, B. D. Microglia and neuroprotection. *Journal of Neurochemistry* **136**, 10–17 (2016).
221. Huchzermeyer, C., Berndt, N., Holzhütter, H.-G. & Kann, O. Oxygen Consumption Rates during Three Different Neuronal Activity States in the Hippocampal CA3 Network. *J Cereb Blood Flow Metab* **33**, 263–271 (2013).
222. Ivanov, A. & Zilberter, Y. Critical State of Energy Metabolism in Brain Slices: The Principal Role of Oxygen Delivery and Energy Substrates in Shaping Neuronal Activity. *Front. Neuroenergetics* **3**, (2011).
223. Mulkey, D. K., Henderson, R. A., Olson, J. E., Putnam, R. W. & Dean, J. B. Oxygen measurements in brain stem slices exposed to normobaric hyperoxia and hyperbaric oxygen. *Journal of Applied Physiology* **90**, 1887–1899 (2001).
224. Masuch, A., Shieh, C.-H., van Rooijen, N., van Calker, D. & Biber, K. Mechanism of microglia neuroprotection: Involvement of P2X7, TNFα, and valproic acid. *Glia* **64**, 76–89 (2016).
225. Morrison, H. W. & Filosa, J. A. A quantitative spatiotemporal analysis of microglia morphology during ischemic stroke and reperfusion. *J Neuroinflammation* **10**, 782 (2013).
226. Sadler, R. *et al.* Short-Chain Fatty Acids Improve Poststroke Recovery via Immunological Mechanisms. *J. Neurosci.* **40**, 1162–1173 (2020).
227. Singh, V. *et al.* The gut microbiome primes a cerebroprotective immune response after stroke. *J Cereb Blood Flow Metab* **38**, 1293–1298 (2018).
228. Davies, D. S., Ma, J., Jegathees, T. & Goldsbury, C. Microglia show altered morphology and reduced arborization in human brain during aging and Alzheimer's disease. *Brain Pathology* **27**, 795–808 (2017).
229. Rueda-Carrasco, J. *et al.* SFRP1 modulates astrocyte-to-microglia crosstalk in acute and chronic neuroinflammation. *EMBO reports* **22**, e51696 (2021).

230. Madry, C. *et al.* Effects of the ecto-ATPase apyrase on microglial ramification and surveillance reflect cell depolarization, not ATP depletion. *Proceedings of the National Academy of Sciences* **115**, E1608–E1617 (2018).
231. Tóth, K. *et al.* The NKCC1 ion transporter modulates microglial phenotype and inflammatory response to brain injury in a cell-autonomous manner. *PLOS Biology* **20**, e3001526 (2022).
232. Matyash, M., Zabiegalov, O., Wendt, S., Matyash, V. & Kettenmann, H. The adenosine generating enzymes CD39/CD73 control microglial processes ramification in the mouse brain. *PLOS ONE* **12**, e0175012 (2017).
233. Nasu-Tada, K., Koizumi, S. & Inoue, K. Involvement of β1 integrin in microglial chemotaxis and proliferation on fibronectin: Different regulations by ADP through PKA. *Glia* **52**, 98–107 (2005).
234. Fekete, R. *et al.* Microglia control the spread of neurotropic virus infection via P2Y12 signalling and recruit monocytes through P2Y12-independent mechanisms. *Acta Neuropathol* **136**, 461–482 (2018).
235. Fields, R. D. & Burnstock, G. Purinergic signalling in neuron–glia interactions. *Nat Rev Neurosci* **7**, 423–436 (2006).
236. Franke, H. & Illes, P. Nucleotide signaling in astrogliosis. *Neuroscience Letters* **565**, 14–22 (2014).
237. Kurpius, D., Nolley, E. P. & Dailey, M. E. Purines induce directed migration and rapid homing of microglia to injured pyramidal neurons in developing hippocampus. *Glia* **55**, 873–884 (2007).
238. Moro, N., Ghavim, S. S. & Sutton, R. L. Massive efflux of adenosine triphosphate into the extracellular space immediately after experimental traumatic brain injury. *Experimental and Therapeutic Medicine* **21**, 1–10 (2021).
239. Chen, Y. *et al.* Spatiotemporally selective astrocytic ATP dynamics encode injury information sensed by microglia following brain injury in mice. *Nat Neurosci* **27**, 1522–1533 (2024).
240. Li, H. *et al.* Astrocytes release ATP/ADP and glutamate in flashes via vesicular exocytosis. *Mol Psychiatry* **30**, 2475–2489 (2025).
241. Zimmermann, H., Zebisch, M. & Sträter, N. Cellular function and molecular structure of ecto-nucleotidases. *Purinergic Signalling* **8**, 437–502 (2012).

242. Bosco, D. B. *et al.* RNAseq analysis of hippocampal microglia after kainic acid-induced seizures. *Mol Brain* **11**, 34 (2018).
243. Peng, J. *et al.* Microglial P2Y12 receptor regulates ventral hippocampal CA1 neuronal excitability and innate fear in mice. *Mol Brain* **12**, 71 (2019).
244. Schmid, C. D. *et al.* Differential gene expression in LPS/IFNγ activated microglia and macrophages: in vitro versus in vivo. *Journal of Neurochemistry* **109**, 117–125 (2009).
245. Gu, N. *et al.* Microglial P2Y12 receptors regulate microglial activation and surveillance during neuropathic pain. *Brain, Behavior, and Immunity* **55**, 82–92 (2016).
246. Lin, S.-S., Tang, Y., Illes, P. & Verkhratsky, A. The Safeguarding Microglia: Central Role for P2Y12 Receptors. *Front. Pharmacol.* **11**, (2021).
247. Zrzavy, T. *et al.* Loss of 'homeostatic' microglia and patterns of their activation in active multiple sclerosis. *Brain* **140**, 1900–1913 (2017).
248. Cunha, R. A., Sebastião, A. M. & Ribeiro, J. A. Inhibition by ATP of Hippocampal Synaptic Transmission Requires Localized Extracellular Catabolism by Ecto-Nucleotidases into Adenosine and Channeling to Adenosine A1 Receptors. *J. Neurosci.* **18**, 1987–1995 (1998).
249. Araque, A. *et al.* Gliotransmitters Travel in Time and Space. *Neuron* **81**, 728–739 (2014).
250. Corkrum, M. *et al.* Dopamine-Evoked Synaptic Regulation in the Nucleus Accumbens Requires Astrocyte Activity. *Neuron* **105**, 1036-1047.e5 (2020).
251. Sheridan, G. K. & Murphy, K. J. Neuron–glia crosstalk in health and disease: fractalkine and CX3CR1 take centre stage. *Open Biology* **3**, 130181 (2013).
252. Miyamoto, A., Wake, H., Moorhouse, A. J. & Nabekura, J. Microglia and synapse interactions: fine tuning neural circuits and candidate molecules. *Front. Cell. Neurosci.* **7**, (2013).
253. Schafer, D. P., Lehrman, E. K. & Stevens, B. The "quad-partite" synapse: Microglia-synapse interactions in the developing and mature CNS. *Glia* **61**, 24–36 (2013).
254. Wu, Y., Dissing-Olesen, L., MacVicar, B. A. & Stevens, B. Microglia: Dynamic Mediators of Synapse Development and Plasticity. *Trends in Immunology* **36**, 605–613 (2015).

255. Favuzzi, E. *et al.* GABA-receptive microglia selectively sculpt developing inhibitory circuits. *Cell* **184**, 4048-4063.e32 (2021).
256. Weinhard, L. *et al.* Microglia remodel synapses by presynaptic trogocytosis and spine head filopodia induction. *Nat Commun* **9**, 1228 (2018).
257. Parkhurst, C. N. *et al.* Microglia Promote Learning-Dependent Synapse Formation through Brain-Derived Neurotrophic Factor. *Cell* **155**, 1596–1609 (2013).
258. Samanta, S., Chakraborty ,Sanjoy & and Bagchi, D. Pathogenesis of Neurodegenerative Diseases and the Protective Role of Natural Bioactive Components. *Journal of the American Nutrition Association* **43**, 20–32 (2024).
259. Basilico, B. *et al.* Microglia control glutamatergic synapses in the adult mouse hippocampus. *Glia* **70**, 173–195 (2022).
260. Kim, J., Pavlidis, P. & Ciernia, A. V. Development of a High-Throughput Pipeline to Characterize Microglia Morphological States at a Single-Cell Resolution. *eNeuro* **11**, (2024).
261. Salamanca, L. *et al.* MIC-MAC: An automated pipeline for high-throughput characterization and classification of three-dimensional microglia morphologies in mouse and human postmortem brain samples. *Glia* **67**, 1496–1509 (2019).

9. The candidate's publications

Related to this thesis:

1. ***Péter Berki***, *Csaba Cserép*, Zsuzsanna Környei*, Balázs Pósfai, Eszter Szabadits, Andor Domonkos, Anna Kellermayer, Miklós Nyerges, Xiaofei Wei, Istvan Mody, Araki Kunihiko, Heinz Beck, He Kaikai, Wang Ya, Nikolett Lénárt, Zhaofa Wu, Miao Jing, Yulong Li, Attila I Gulyás, Ádám Dénes (2024):*
Microglia contribute to neuronal synchrony despite endogenous ATP-related phenotypic transformation in acute mouse brain slices.
Nature Communications, *15*(1), 5402. *:co-first authors

2. *Krisztina Tóth, Nikolett Lénárt, **Péter Berki**, Rebeka Fekete, Eszter Szabadits, Balázs Pósfai, Csaba Cserép, Ahmad Alatshan, Szilvia Benkő, Dániel Kiss, Christian A Hübner, Attila Gulyás, Kai Kaila, Zsuzsanna Környei, Ádám Dénes (2022):*
The NKCC1 ion transporter modulates microglial phenotype and inflammatory response to brain injury in a cell-autonomous manner.
PLoS biology, *20*(1), e3001526.

Unrelated to the thesis:

3. *Virág Takács, Zsuzsanna Bardóczi, Áron Orosz, Abel Major, Luca Tar, **Péter Berki**, Péter Papp, Márton I Mayer, Hunor Sebők, Luca Zsolt, Katalin E Sos, Szabolcs Káli, Tamás F Freund, Gábor Nyiri (2024):*
Synaptic and dendritic architecture of different types of hippocampal somatostatin interneurons.
PLoS Biology, *22*(3), e3002539.

10. Acknowledgements

First and foremost, I extend my heartfelt gratitude to my supervisors, Attila Gulyás and Ádám Dénes, for their unwavering support, insightful guidance, and constant encouragement. Their readiness for conversation and feedback has been invaluable, fostering my growth not only as a scientist but also as an individual.

I am profoundly grateful to Zsuzsanna Környei and Csaba Cserép, their expertise and contribution have been instrumental in shaping this work. My sincere thanks also go to all the members of the IEM - Neuroimmunology Lab, with special mention to Krisztina Tóth, Balázs Pósfai, Eszter Szabadits, and Nikolett Lénárt, for their collaboration.

A special note of thanks to Dániel Schlingloff, whose tremendous support during my undergraduate and PhD years was invaluable. I am also deeply appreciative of Ferenc Mátyás, who wholeheartedly supported the finalization of this project. Additionally, I am grateful for the camaraderie and support of my former colleagues: Diego Lopez, Zsolt Kohus, Kriczky Nándor, and all members of the IEM - Neuronal Network and Behavior Research Group.

My PhD studies were supported by the New National Excellence Program of the Ministry for Culture and Innovation from the source of the National Research, Development and Innovation Fund (EKÖP-2024-87).

Lastly, I am deeply indebted to my loved ones, Flóra Matuska and my family for their unwavering encouragement and understanding, especially during the most challenging times.

I would like to dedicate this work to my late father, who taught me that hard work and perseverance will always come back with benefits.